COMPUTATIONAL MODELLING STUDY ON PHASE STABILITY OF Li_2MnO_3 CATHODE MATERIAL FOR LITHIUM-ION BATTERIES

By

MAMONAMANE GRATITUDE MPHAHLELE

RESEARCH DISSERTATION

Submitted in fulfilment of the requirement for the degree of

MASTER OF SCIENCE

In

Physics

In the

FACULTY OF SCIENCE AND AGRICULTURE

(School of Physical and Mineral Sciences)

At the

UNIVERSITY OF LIMPOPO

(Turfloop Campus)

South Africa

SUPERVISOR: Prof. R S Ledwaba

CO-SUPERVISORS: Dr. M C Masedi

: Prof. P E Ngoepe

2023

Abstract

Li_2MnO_3 has been identified as a promising cathode material for secondary lithium-ion batteries due to its high theoretical capacity, nontoxicity and low cost. However, its application is hindered by structural transformations that lead to poor cycle capabilities. Cationic dopants have been used to reduce the collapse of the structure and they tend to improve the performance of cathode materials. As such, it is highly desirable to identify new doped structures as a remedial technique to optimize the properties of Li_2MnO_3.

Firstly, the structural, electronic and mechanical properties of pristine Li_2MnO_3 were investigated. All calculations were carried out using VASP and PHONON codes as implemented in MedeA software, employing the density functional theory with Hubbard correction (DFT+U). The equilibrium lattice parameters were obtained by performing full structure optimization of Li_2MnO_3 and the results agreed well with those reported experimentally and in literature. The predicted heat of formation was negative indicating that the structure is thermodynamically stable. Furthermore, phonon dispersion curves showed no negative vibrations suggesting dynamic stability. The elastic constants revealed that the Li_2MnO_3 structure is mechanically stable.

Secondly, the cluster expansion formalism was used for the generation of $Li_2Mn_{1-x}Ni_xO_3$, $Li_2Mn_{1-x}Co_xO_3$, $Li_2Mn_{1-x}Cr_xO_3$ and $Li_2Mn_{1-x}Ru_xO_3$ new phases with different concentrations and symmetries. The binary phase diagram predicted $Li_2Mn_{0.83}Ni_{0.17}O_3$, $Li_2Mn_{0.5}Co_{0.5}O_3$, $Li_2Mn_{0.5}Cr_{0.5}O_3$ and $Li_2Mn_{0.5}Ru_{0.5}O_3$ as the most stable phases of doped Li_2MnO_3. Lastly, Monte Carlo simulations were used to identify the ordered to disordered transition temperatures. Monte Carlo simulations produced thermodynamic properties for $Li_2Mn_{1-x}Ni_xO_3$, $Li_2Mn_{1-x}Co_xO_3$, $Li_2Mn_{1-x}Cr_xO_3$ and $Li_2Mn_{1-x}Ru_xO_3$ systems for the entire range of transition metals concentrations obtained from cluster expansion and it demonstrated that $Li_2Mn_{1-x}Ni_xO_3$, $Li_2Mn_{1-x}Co_xO_3$, $Li_2Mn_{1-x}Cr_xO_3$ and $Li_2Mn_{1-x}Ru_xO_3$ systems are phase separating systems at 0 K but changes to mixed systems at approximately 700 K-1700 K range which was confirmed by constructing the phase diagrams of all the four mixed systems. This validation will provide valuable insights which will guide experiments on where phase separation and mixed phases tend to occur in $Li_2Mn_{1-x}Ni_xO_3$, $Li_2Mn_{1-x}Co_xO_3$, $Li_2Mn_{1-x}Cr_xO_3$ and $Li_2Mn_{1-x}Ru_xO_3$ systems.

The findings show the usefulness of combing CE and MC simulations when searching for new stable multi-component materials. The structures generated in this study may be useful in future as electrode materials in lithium-ion materials.

Declaration

I declare that the dissertation hereby submitted to the University of Limpopo for the degree of Master of Science has not previously been submitted by me for a degree at this or any other university, that it is my own work both in design and execution, and that all material contained herein has been duly acknowledged.

31/03/2023

Mphahlele M.G (Ms) Date

Dedication

This work is dedicated to my wonderful parents Donald and Maphokeng Mphahlele, my siblings (Mohlapa, Nkgudi, Bonolo, Tsongoane and Phologe Mphahlele), my son Bohlale Mphahlele, nephew Lehlogonolo Mphahlele and my cousin Matholo Bapela

Acknowledgements

Foremost, I would like to thank God almighty for guidance and wisdom. I would express my sincere gratitude to my supervisor, Prof R.S. Ledwaba and co-supervisors Dr M.C. Masedi and Prof P.E. Ngoepe for constantly giving me support and their excellent supervision. I would also like to thank Dr K.T. Malatji for his insightful research assistance. I would also like to thank the members of the Materials Modelling Centre for their input on my research. I would also like to acknowledge National Research Foundation for financial assistance.

I also send my sincere gratitude to my family; they have always been there for me. Their constant support is greatly appreciated, and I, therefore, dedicate this dissertation to my family.

Table of contents

List of figures xi

List of tables xiv

List of abbreviations xv

List of symbols xvi

CHAPTER 1 : INTRODUCTION 1

1.1. General introduction 1

1.2. General background of batteries 2

1.2.1. Brief description of a battery 2

1.2.2. Applications 3

1.3. Literature review 4

1.3.1. Structural properties 4

1.3.2. Layered-spinel transformation 4

1.3.3. Doping Li_2MnO_3 6

1.4. Rationale 7

1.5. Objectives 9

1.6. Outline 9

CHAPTER 2 : METHODOLOGY 10

2.1. Introduction 10

2.2. Density functional theory 10
2.3. Approximation methods 14
2.3.1. Local density approximation 14
2.3.2. Generalized gradient approximation 15
2.4. Plane-wave pseudopotential method 16
2.4.1. Plane-waves and pseudopotentials 16
2.4.2. Pseudopotential approximation 18
2.5. k-sampling 20
2.6. Planewave Pseudopotential Code VASP 21
2.6.1. VASP Code 21
2.7. PHONON code 21
2.8. The Cluster Expansion 22
2.8.1. Basic Principles of the Cluster Expansion 23
2.8.2. The UNCLE-Code 24
2.8.3. Selecting the Input Structures 25
2.8.4. Genetic Algorithm 25
2.8.5. Running the Cluster Expansion 27
2.8.5.1. Miscible Constituents 28
2.8.5.2. Miscibility Gap 28
2.9. Monte Carlo Simulations 29
2.9.1. Random Walks and Markov chains 30

2.9.2. Implementation of the MC Simulation in the UNCLE Code 32

2.9.3. Grand-canonical Ensemble 32

2.9.4. Canonical Ensemble 33

2.10. Theoretical background of calculated properties 34

2.10.1. Heat of formation 34

2.10.2. Elasticity 34

2.10.3. Definition of elastic constants 36

2.10.4. Calculations of elastic constants 36

2.10.5. Elastic Constant Stability Conditions 37

2.10.6. Phonon dispersion curves 39

2.10.7. Density of states 40

CHAPTER 3 : STRUCTURAL, ELECTRONIC AND MECHANICAL PROPERTIES OF BULK LI_2MNO_3 42

3.1. Cut-off energy and the *k*-point convergence 42

3.1.1. Cut-off energy 42

3.1.2. *k*-points 43

3.2. Geometry optimization 44

3.3. Heat of formation of Li_2MnO_3 structure 44

3.4. Density of states 45

3.5. Elastic properties 46

3.6. Phonon dispersion curves 49

3.7. Discussion 50

CHAPTER 4 : CLUSTER EXPANSIONS AND MONTE CARLO SIMULATIONS FOR $LI_2TM_{1-X}NI_XO_3$ SYSTEMS (TM= NI, CO, CR, RU) WHERE 0≤X≤1 52

4.1. Introduction 52

4.2. Simulation procedure 52

4.3. Results 52

4.3.1. Search for the Ground States (Cluster Expansion) 53

4.3.1.1. $Li_2Mn_{1-x}Ni_xO_3$ 53

4.3.1.2. $Li_2Mn_{1-x}Co_xO_3$ 54

4.3.1.3. $Li_2Mn_{1-x}Cr_xO_3$ 56

4.3.1.4. $Li_2Mn_{1-x}Ru_xO_3$ 57

4.3.2. Monte Carlo Simulations 59

4.3.2.1. $Li_2Mn_{1-x}Ni_xO_3$ 59

4.3.2.2. $Li_2Mn_{1-x}Co_xO_3$ 62

4.3.2.3. $Li_2Mn_{1-x}Cr_xO_3$ 65

4.3.2.4. $Li_2Mn_{1-x}Ru_xO_3$ 68

4.3.3. Constructed Phase Diagrams 71

4.3.3.1. $Li_2Mn_{1-x}Ni_xO_3$ 72

4.3.3.2. $Li_2Mn_{1-x}Co_xO_3$ 73

4.3.3.3. $Li_2Mn_{1-x}Cr_xO_3$ 75

4.3.3.4. $Li_2Mn_{1-x}Ru_xO_3$ 76

4.4. Discussion 77

CHAPTER 5 : CONCLUSIONS AND RECOMMENDATIONS....79

5.1. Conclusions 79

5.2. Recommendations and future work 80

Bibliography....81

Appendix A 93

Papers presented at conferences....93

List of figures

Figure 1.1: Applications of lithium-ion batteries 3

Figure 1.2: Crystalline structure of layered Li_2MnO_3 4

Figure 1.3: Schematic illustration of layered to spinel transformation in Li_2MnO_3 during the initial cycle and after multiple cycles [14]. 6

Figure 2.1: Schematic illustration of all-electron (solid lines) and pseudo-electron (dashed lines) potentials and their corresponding wave functions [64].....19

Figure 2.2: a. Basic lattice b. Configuration and c. Cluster interactions 23

Figure 2.3: Self-consistent working plan as used by UNCLE for the cluster expansion for finding new input structures [77] 25

Figure 2.4: Illustration of the genetic algorithm 26

Figure 2.5: Ground state line of the binary $Li_2Mn_{1-x}Ni_xO_3$ systems for a bcc-parent lattice. .27

Figure 2.6: Binary ground state diagram illustrating miscible constituent 28

Figure 2.7: Binary ground state diagram illustrating miscibility gap 29

Figure 2.8: Visualization of MC steps in UNCLE. A grand canonical simulation changes the properties of the atoms in the crystal. The canonical approach changes the position of two atoms in the crystal.....32

Figure 3.1: The variation of total energy as a function of cut-off energy 43

Figure 3.2: The variation of total energy as a function of k-points 44

Figure 3.3: a. TDOS for bulk Li_2MnO_3 b. PDOS for O c. PDOS for Li and d. PDOS for Mn.46

Figure 3.4: Phonon dispersion curves for bulk Li_2MnO_3 50

Figure 4.1: The ground state line of the $Li_2Mn_{1-x}Ni_xO_3$ system: the heat of formation versus Ni concentration and ground state structures.....53

Figure 4.2: The ground state line of the $Li_2Mn_{1-x}Co_xO_3$ system: the heat of formation versus Co concentration and ground state structures. 55

Figure 4.3: The ground state line of the $Li_2Mn_{1-x}Cr_xO_3$ system: the heat of formation versus Cr concentration and ground state structures. 56

Figure 4.4: The ground state line of the $Li_2Mn_{1-x}Ru_xO_3$ system: the heat of formation versus Ru concentration and ground state structures. 58

Figure 4.5: Temperatures profiles cross sections through the 10 × 10 × 10 Monte Carlo simulation cells of a) $Li_2Mn_{0.1}Ni_{0.9}O_3$ b) $Li_2Mn_{0.2}$ $Ni_{0.8}O_3$ and c) $Li_2Mn_{0.3}Ni_{0.7}O_3$.....60

Figure 4.6: Temperatures profiles cross sections through the 10 × 10 × 10 Monte Carlo simulation cells of a) $Li_2Mn_{0.4}Ni_{0.6}O_3$, b) $Li_2Mn_{0.5}Ni_{0.5}O_3$ and c) $Li_2Mn_{0.6}Ni_{0.4}O_3$.....61

Figure 4.7: Temperatures profiles cross sections through the 10 × 10 × 10 Monte Carlo simulation cells of a) $Li_2Mn_{0.7}Ni_{0.3}O_3$ b) $Li_2Mn_{0.8}Ni_{0.2}O_3$ and c) $Li_2Mn_{0.9}Ni_{0.1}O_3$.....62

Figure 4.8: Temperatures profiles cross sections through the 10 × 10 × 10 Monte Carlo simulation cells of a) $Li_2Mn_{0.1}Co_{0.9}O_3$ 1, b) $Li_2Mn_{0.2}Co_{0.8}O_3$ and c) $Li_2Mn_{0.3}Co_{0.7}O_3$ 63

Figure 4.9: Temperatures profiles cross sections through the 10 × 10 × 10 Monte Carlo simulation cells of a) $Li_2Mn_{0.4}Co_{0.6}O_3$ b) $Li_2Mn_{0.5}Co_{0.5}O_3$ and c) $Li_2Mn_{0.6}Co_{0.4}O_3$ 64

Figure 4.10:Temperatures profiles cross sections through the 10 × 10 × 10 Monte Carlo simulation cells of a) $Li_2Mn_{0.7}$ $Co_{0.3}O_3$ b) $Li_2Mn_{0.8}Co_{0.2}O_3$ c) $Li_2Mn_{0.9}Co_{0.1}O_3$ 65

Figure 4.11: Temperatures profiles cross sections through the 10 × 10 × 10 Monte Carlo simulation cells of a) $Li_2Mn_{0.1}Cr_{0.9}O_3$ b) $Li_2Mn_{0.2}Cr_{0.8}O_3$ and c) $Li_2Mn_{0.3}Cr_{0.7}O_3$ 66

Figure 4.12: Temperatures profiles cross sections through the 10 × 10 × 10 Monte Carlo simulation cells of a) $Li_2Mn_{0.4}Cr_{0.6}O_3$ b) $Li_2Mn_{0.5}Cr_{0.5}O_3$ and c) $Li_2Mn_{0.6}Cr_{0.4}O_3$ 67

Figure 4.13: Temperatures profiles cross sections through the 10 × 10 × 10 Monte Carlo simulation cells of a) $Li_2Mn_{0.7}Cr_{0.3}O_3$ c) $Li_2Mn_{0.8}Cr_{0.1}O_3$ and c) $Li_2Mn_{0.9}Cr_{0.1}O_3$.....68

Figure 4.14: Temperatures profiles cross sections through the 10 × 10 × 10 Monte Carlo simulation cells of a) $Li_2Mn_{0.1}Ru_{0.9}O_3$ b) $Li_2Mn_{0.2}Ru_{0.8}O_3$ and c) $Li_2Mn_{0.3}Ru_{0.7}O_3$.....69

Figure 4.15: Temperatures profiles cross sections through the 10 × 10 × 10 Monte Carlo simulation cells of a) $Li_2Mn_{0.4}Ru_{0.6}O_3$ b) $Li_2Mn_{0.5}Ru_{0.5}O_3$ and c) $Li_2Mn_{0.6}Ru_{0.4}O_3$ 70

Figure 4.16: Temperatures profiles cross sections through the 10 × 10 × 10 Monte Carlo simulation cells of a) $Li_2Mn_{0.7}Ru_{0.3}O_3$, b) $Li_2Mn_{0.8}Ru_{0.2}O_3$ and c) $Li_2Mn_{0.9}Ru_{0.1}O_3$ 71

Figure 4.17: Constructed phase diagram of $Li_2Mn_{1-x}Ni_xO_3$ using critical temperatures at different concentrations. 73

Figure 4.18: Constructed phase diagram of $Li_2Mn_{1-x}Co_xO_3$ using critical temperatures at different concentrations. 74

Figure 4.19: Constructed phase diagram of $Li_2Mn_{1-x}CrxO_3$ using critical temperature at different concentrations. 76

Figure 4.20: Constructed phase diagram of $Li_2Mn_{1-x}RuxO_3$ using critical temperature at different concentrations. 77

List of tables

Table 3.1: The equilibrium lattice parameters and heats of formation of bulk Li_2MnO_3.....45

Table 3.2: List of elastic constants for bulk Li_2MnO_3.....48

Table 3.3: Bulk, Shear, Young's Modulus and B/G for bulk Li_2MnO_3.....49

Table 4.1: Stable structures of $Li_2Mn_{1-x}Ni_xO_3$ along the ground state line.....54

Table 4.2: Stable structures of $Li_2Mn_{1-x}Co_xO_3$ along the ground state line 55

Table 4.3: Stable structures of $Li_2Mn_{1-x}Cr_xO_3$ along the ground state line 57

Table 4.4: Stable structures of $Li_2Mn_{1-x}Ru_xO_3$ along the ground state line 58

Table 4.5:Concentration of Manganese Nickel with respect to critical temperatures for a mixed system $Li_2Mn_{1-x}Ni_xO_3$.....72

Table 4.6:Concentration of Manganese Cobalt with respect to critical temperatures for a mixed system $Li_2Mn_{1-x}Co_xO_3$ 74

Table 4.7: Concentration of Manganese chromium with respect to critical temperatures for a mixed system $Li_2Mn_{1-x}Cr_xO_3$ 75

Table 4.8: Concentration of Manganese ruthenium with respect to critical temperatures for a mixed system $Li_2Mn_{1-x}RuxO_3$.....76

List of abbreviations

CE Cluster expansion

CV Cross-validation

DFT Density functional theory

ECI Effective cluster interaction

DOS Density of states

EV Electric vehicle

GA Genetic algorithm

GGA Generalized gradient approximation

HEV Hybrid electric vehicle

LDA Local Density approximation

LIB Li-ion battery

MC Monte Carlo

MD Molecular dynamics

PAW Projector Augmented Wave

PBE Perdew, Burke, and Ernzerhof

PDOS Partial density of states

UNCLE Universal cluster expansion

US-PP ultra-soft Vanderbilt pseudopotential

VASP Vienna Ab-initio Simulation Package

List of symbols

ρ Charge density

E Energy

$\{R_\alpha\}$ Set of positions of all atoms in a system

U Coulomb energy

U_{en} Coulomb attraction between electron and nuclei

U_{ee} Coulomb repulsion between like charges

U_{en} Coulomb repulsion between nuclei

e Proton's elemental charge

Z'_α Atomic number of atom α

T[ρ] Kinetic energy of a system of non-interacting particles of density ρ

U[ρ] Classical electrostatic energy due to Coulombic interactions

E_{xc} Exchange-correlation energy

ε_{xc}^0 Exchange-correlation potential

V(r) External potential

V_{eff} (r) Effective potential

Ψ_i Wave function of electronic state

ϵ_i Kohn-Sham eigenvalue

V_H Hartree potential of the electrons

Ψ_{nk} Single-electron wave-function

$\mu_{n,k}$ Expansion coefficients

E_{band} Band energy

E_{rep} Repulsive energy

U_{ij} Repulsive pair energy terms

U Hubbard parameter

J exchange interaction term

J_c Interaction energy

P Transition probability

Δμ Change in chemical potential

E_f Fermi level

ΔH_f Heats of formation

Y Young's modulus

V_0 Equilibrium volume

C_{ij} Elastic constants

ε Strain

E_0 Energy of a crystal prior deformation

B Bulk modulus

G Shear modulus

T_0 Kinetic energy

T Thermodynamic temperature

m Mass

p Momentum

k Boltzmann constant

N Number of degrees of freedom of a system

Scv Fitness cross-validation score

r_0 Wave function confinement radius

n_0 Density confinement radius DFT total energy of the structure $\vec{\sigma}$

E_{DFT} ($\vec{\sigma}$) DFT total energy of the structure $\vec{\sigma}$

n_i ($\vec{\sigma}$) Number of atoms of atomic species i contained in structure $\vec{\sigma}$

Chapter 1 : Introduction

This chapter contains a detailed introduction to this work, the background and its objectives. The battery and its applications will be discussed, and previous studies on doping are also reviewed. The rationale and objectives of this study are also stated. Finally, there is a brief outline of the entire dissertation.

1.1. General introduction

Due to the increase in population and developments in technology, there is an ever-increasing demand for energy and the need for high-energy storage materials has become more prevalent. This is resulting in the rapid massive consumption of fossil-fuel resources [1, 2]. Rising energy demands and the depletion of fossil-fuel resources necessitate the pursuit of sustainable energy solutions, which include both renewable energy sources and sustainable storage technologies. To reduce the emission of greenhouse gases, the exploitation of renewable energy sources and storage is urgently needed, which demands a reliable and eco-friendly energy storage system [3]. As a result, new materials with improved properties for energy storage devices are required. Material abundance, environmentally friendly synthetic techniques, and life-cycle analyses must all be considered while designing novel electrochemical storage devices [3, 4, 5].

Lithium-ion batteries are widely used as energy storage systems to power equipment because of their high specific energy density and power density, long service life, low self-discharge rate and lack of memory effect [6]. However, their low energy density makes them too limited for high-power applications such as electric vehicles (EV). Additionally, for high-power applications, power density, cycling life and safety concerns are raised. As a result, further advancements in lithium-ion battery materials development engineering are required [7].

Cathode materials have a significant impact on the performance and safety of lithium-ion batteries. Currently, the most common cathode materials in commercial lithium-ion batteries are $LiCoO_2$, $LiMn_2O_4$ and $LiFePO_4$ [8]. $LiCoO_2$ surface reactivity and instability limit its practical capacity to approximately 140 mAh/g, which is half of its theoretical value (273 mAH/g) [9]. On the other hand, the olivine $LiFePO_4$ and spinel $LiMn_2O_4$ have received

attention due to their excellent cyclic performance, environmental friendliness, and low cost. Their low energy densities, however, limit their applications [10]. As a result, significant efforts have been made to investigate alternative cathode materials to improve the energy density of these rechargeable batteries.

The layered lithium-rich cathode material Li_2MnO_3 has piqued the interest of researchers in recent years due to its high theoretical specific capacity of 459 mAh/g, good environmental benignity, an abundance of Mn, and high operating voltage [11]. However, its application is hampered by low practical specific capacity and structural degradation during cycling [12]. In previous studies, Li_2MnO_3 has been known to be electrochemically inactive, however, a study by Kalymati *et al.* was the first to negate the findings [13]. Nowadays it is commonly accepted that the structure can undergo electrochemical cycling if it is activated by chemical or electrochemical means [14]. During the activation process, the surface oxygen is released from the crystal lattice, the Mn is driven into the Li layer and the structure gradually transforms from layered into spinel structure resulting in increased resistance, capacity decay and reduced lifespan of the battery [15, 16]. Moreover, the oxygen produced can cause ignition and even explosion, so LMO has been classified as a hazardous material [17].

Extensive efforts have been made to address these issues, with doping emerging as the most promising solution. The doping approach has been used in an attempt to inhibit structural transformation in the initial stages of cycling. Numerous studies of transitional metals (Ru, Fe, Ni, Co, Ti, Cr, Cu, V, T, Nb, and Zn) doping have been reported [18, 19, 20, 21, 22]. The studies show improvements in electrochemical properties, but the capacity retention remains too low for practical applications [23].

1.2. General background of batteries

1.2.1. Brief description of a battery

A battery can be defined as a collection of one or more electrical cells that convert chemical energy into electrical energy [4]. There are two major classes of batteries: primary and secondary batteries. Primary batteries are those which cannot be recharged because the chemical reaction within them cannot be reversed. Secondary batteries are rechargeable and can be used repeatedly. Lithium-ion batteries are secondary batteries that store energy

chemically via a redox reaction involving lithium intercalation between the cathode and anode. The lithium ion moves back and forth between the anode and cathode as the battery is discharged/charged. A lithium-ion battery comprises a cathode, anode, electrolyte, and separator [24]. When the battery is charged, the lithium ions in the cathode material migrate through the separator to the anode with the flow of charging current through the external circuit. In the opposite direction, the lithium ions in the anode migrate through the separator to the cathode material with the flow of discharging current through the external circuit. The electrodes are not in direct contact but are electrically connected by the electrolyte while the separator stops the mixing between the two but allows the flow of ions [25].

1.2.2. Applications

Lithium-ion batteries are one of this era's widely used electrochemical storage systems, known for among others, powering countless portable electronics, power tools, hybrid electric vehicles (HEV), and the electric grid. This varied range of applications is because of Li-based chemistry, which provides low redox potential and thereby increases the energy and power density of the system. Additionally, their long cycling life and are lightweight [26, 27].

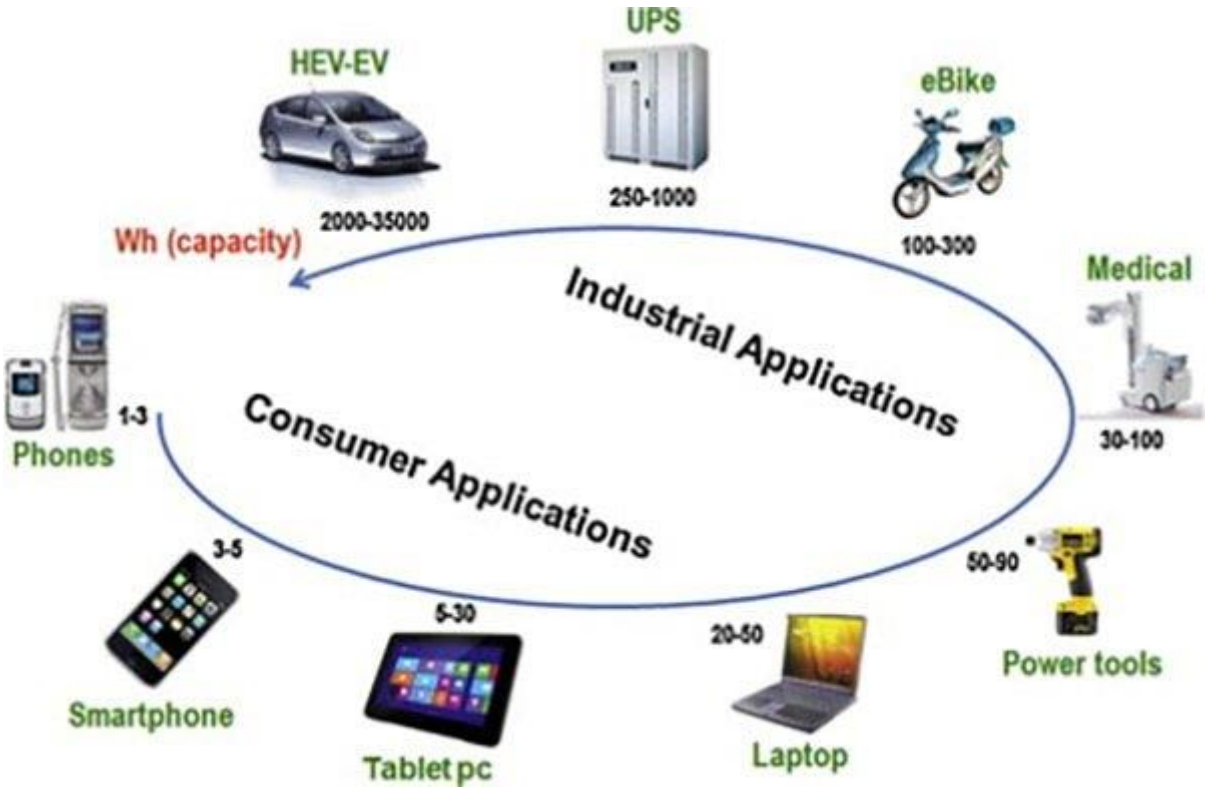

Figure 1.1: Applications of lithium-ion batteries

1.3. Literature review

1.3.1. Structural properties

Li_2MnO_3 structure is described by the space group C2/m, in a monoclinic cell with parameters a= 4.937 Å, b= 8.532 Å, c= 5.030 Å, β= 109.46º and α=γ= 90º. Figure 1.2 shows the modelled structure of Li_2MnO_3. Lithium ions occupy the 2b (0, 1/2, 0), 2c (0, 0, 1/2), and 4h (0, 0.6606, 1/2) sites, the manganese ions the 4g (0, 0.16708, 0) site, and the oxygen ions the 4i (0.2189, 0, 0.2273) and 8j (0.2540, 0.32119, 0.2233) sites. It has an O3-type structure, which can be redefined as $Li[Li_{1/3}Mn_{2/3}]O_2$. The transitional metal layer is composed of monovalent lithium and tetravalent manganese, with Li and Mn ions occupying octahedral sites in a 1:2 ratio. The lithium and transition metal layers are alternately arranged [28].

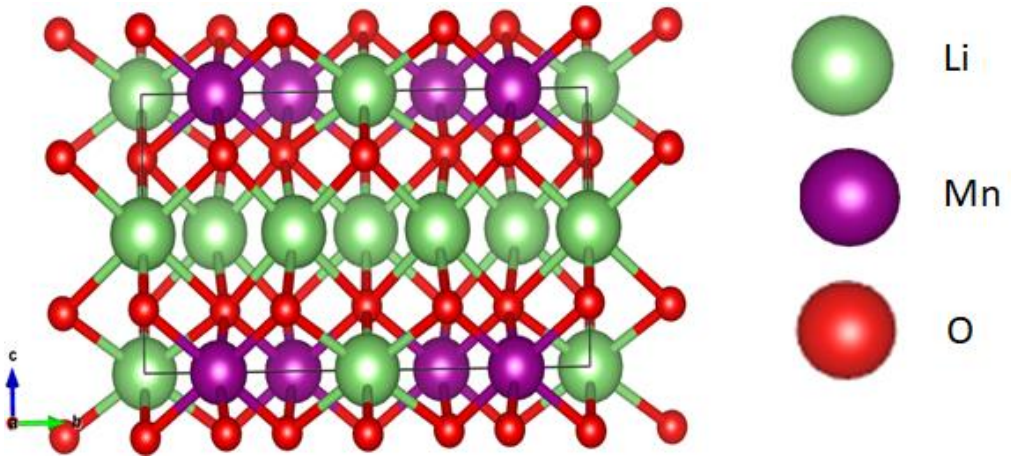

Figure 1.2: Crystalline structure of layered Li_2MnO_3

1.3.2. Layered-spinel transformation

Li_2MnO_3 was initially thought to be electrochemically inactive because oxidation of the Mn^{4+} cation to the higher +5 in its octahedral environment during lithium extraction in the first charge cycle is unlikely. Recent research has shown that Li_2MnO_3 can be electrochemically activated at 4.5 V against lithium. Several delithiation mechanisms have been proposed. Yu *et al.* [29] proposed a first charging mechanism characterized by: (1) simultaneous extraction of Li from the Li and the mixed metal cation layers (2) retention of the +4 oxidation state of Mn, and (3) charge compensation via loss of oxygen or reaction with the electrolyte. However, during cycling, the monoclinic structure gradually transforms into a cubic spinel structure [29].

The first-principle study by Okamoto [30] found that the Mn contribution in charge compensation during lithium extraction increases as the ratio of oxygen vacancies increases and linked the two to the significant decrease of Li-ion extraction potential.

Li_2MnO_3 is a promising cathode material for next-generation lithium-ion batteries. However, the electrochemically activated Li_2MnO_3 faces an irreversible structural transformation due to the loss of lattice oxygen during the early stages of charging, as shown in Figure *1.3*. . The oxidation of Mn^{4+} to Mn^{5+} in an octahedral environment is difficult, the origin of electrochemical activity of Li_2MnO_3 is primarily attributed to the removal of an electron from active oxygen p band near Fermi level. It was also discovered that peroxide (O_2^{2-}) and superoxide (O_2^-) intermediates could form during delithiation. The formed phase has a Li-defect spinel structure, indicating that delithiation results in Mn migration from the transition-metal layer to the Li layer, as well as oxygen release. This layered-to-spinel phase transition is an important bulk process in Li_2MnO_3 activation. Mn remigration occurs during lithiation in the first discharge, and the layered structure is formed again with significant disordering. After a few cycles, the defect spinel structure becomes more oxygen-deficient and has a lower Mn valency. As a result, the amount of Li inserted decreases, corresponding to the capacity and voltage fading observed in Li_2MnO_3 [14, 31, 32].

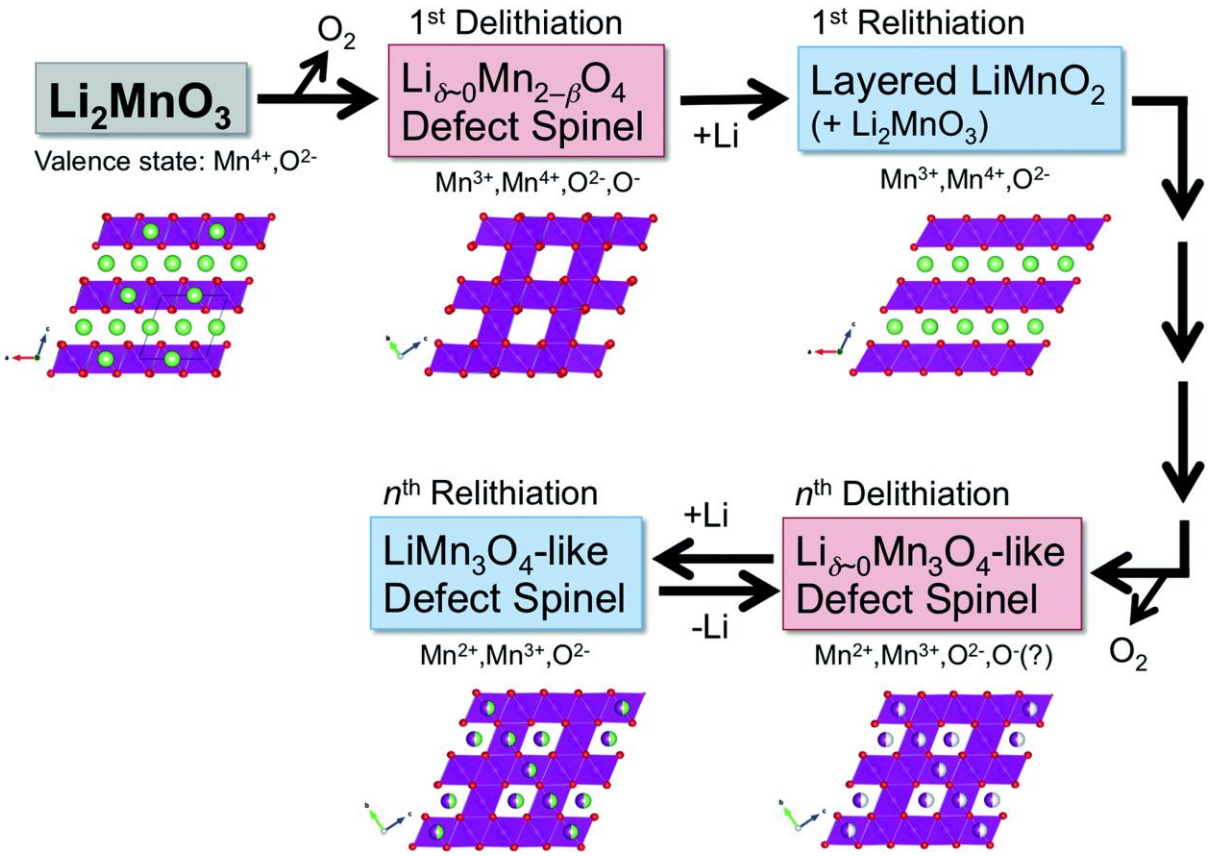

Figure 1.3: Schematic illustration of layered to spinel transformation in Li_2MnO_3 during the initial cycle and after multiple cycles *[14]*.

1.3.3. Doping Li_2MnO_3

Doping has been shown to be an effective method of optimizing operating voltage, capacity retention, charge transport, and phase stability in most cathode materials [21]. There are two types of doping: interstitial doping and substitutional doping. An interstitial dopant occupies an octahedral or tetrahedral hole in the lattice between atoms, whereas a substitutional dopant replaces one of the atoms in the host lattice. The atomic size and electronic properties of the foreign element in substitutional doping are similar to those of the parent material [33]. In previous reports substitutional doping was used, one Mn ion at the 4g position was replaced by a dopant. It has been shown that Mn sites are thermodynamically favoured by most cationic dopants [34]. Furthermore, it was discovered that replacing Mn in the LMO with transition metals such as (Ni, Co, Cr, or Ru) could form strong bonds with the oxygen atoms of the LMO, reducing oxygen production and improving other restrictions to some extent.

A DFT+U study presented by Lanjan *et al.* [35] showed that replacing 50% Mn with Ni or Co lowers the band gap and consequently increases the conductivity of $Li_2Mn_{0.5}TM_{0.5}O_3$. The study further demonstrated that the introduction of these dopants stabilises $Li_2Mn_{0.5}TM_{0.5}O_3$ by preventing the spontaneous removal of oxygen during charge/discharge thus making the material safer to use.

Moreover, a DFT study by Kong *et al.* [36] illustrated that structures of Li_2MnO_3 doped with Ni, Ru or Co are thermodynamically stable with positive heats of formation. They also discovered that Ni and Ru doping inhibit the formation of electron polarons while increasing their conductivity. Mori *et al.* [18] introduced Ru to Li_2MnO_3 and found that $Li_2Mn_{0.4}Ru_{0.6}O_3$ showed a discharge capacity of 192 mAh/g in the initial cycle and retains approximately 88% of the primal capacity after 10 cycles at 0.1 C. Kim et al. [21] have investigated the effects of various transition metal elements that could as dopants to replace some Mn-ions, and the tests reveal that Li_2MnO_3 with 1% Cr substitution exhibits a large initial discharge capacity of 234.9 mAh/g which is higher than the pristine material, but the capacity retention ratio is only 72% after 10 cycles at a lower current density of 0.05 C. According to the study by Gao *et al.* [22], Mo doping is beneficial for improving both dynamic and thermodynamic properties of Li_2MnO_3 by narrowing the band gap and increasing electronic states near the Fermi level. An experimental Ni doping study conducted by Lee's [37] group showed improved redox reaction and long-term cycle with mitigated voltage decay.

1.4. Rationale

The development of high-energy density cathodes for lithium-ion batteries (LIBs) is of great interest. In recent years, layered Li-rich Li_2MnO_3 materials have attracted much attention as potential cathode materials for lithium-ion batteries. In comparison with traditional cathodes, they have a higher specific capacity and a higher working voltage. Li-rich cathode materials have some challenges to overcome before they can be used in practical applications. Their electrochemical performance still needs to be improved in terms of energy density, long-term cycling stability, and rate capability [38].

Li_2MnO_3 exhibits significant improvements when doped with either metal or transitional metals. Dopants play a role in the early stages of delithiation by providing charge compensation and bulk electronic conduction mechanisms, allowing the lattice oxygen to be

oxidized later. Non-oxygen redox couples facilitate lithium removal and improve overall cycling performance [12, 13]. Ni, Co, Cr and Ru have been chosen as transition metals of interest in this study because they have similar ionic radii as Mn atoms [35]. The Ru doping in Li_2MnO_3 provides cycling stability due to the presence of a Ru^{+4}/Ru^{+5} redox couple [39]. Ni promotes the formation of smooth Li percolation paths, thus increasing the number of active Li ions and improving the charge−discharge capacity [40]. Cr can form stronger Cr–O bonds, therefore stabilising the local structural oxygen and hindering the structural transition of Li_2MnO_3 during delithiation [23]. Co could suppress the structure change from layered to spinel and enhance the cycling performance [34]. However, in all these studies only a certain percentage of the dopant was introduced to the Li_2MnO_3, and one or two phases were evaluated.

In the current study, the stability of pristine Li_2MnO_3 will be investigated using density functional theory with Hubbard correction (DFT+U). Three properties will be used to investigate its stability namely, structural, mechanical and electronic properties. In structural properties, the equilibrium lattice parameters and heat of formation will be used to determine its thermodynamic stability, whereby the structure will be considered stable if the heat of formation is negative. Furthermore, calculations of the density of states will be performed. Electronic state behaviour near the Fermi level with respect to band gaps will be observed. Lastly, the mechanical properties of Li_2MnO_3 will be investigated. This will be achieved by performing phonon dispersion calculation, which plays an important role in determining the vibrational properties of the material. Lastly, elastic constant, bulk Modulus, Shear modulus and Young's modulus are calculated to evaluate the elasticity of Li_2MnO_3.

Computational modelling techniques, such as *ab-initio* and atomistic simulation, have provided valuable insights into a variety of materials. Such methods individually play distinct roles along time and length scales of modelling. *Ab initio* methods tend to be more accurate, but they are limited to smaller systems and currently do not effectively address the thermal properties of larger systems [41]. *Ab initio* methods are therefore impractical for materials discovery applications, which require large-scale simulations of the material's phase space. An alternative technique that has proven useful is the Cluster Expansion technique [42].

The Cluster Expansion (CE) technique allows calculations of ground state energy, as well as many other thermodynamic properties, based on data from a small group of alloys similar to

the alloy under consideration. This study will employ the Universal Cluster Expansion (UNCLE) package to configure, construct and automatically converge cluster expansions for Li_2MnO_3 systems in order to produce unique structures and perform thermodynamic analysis of these structures. This method is well-established for alloys [43]. The dopants will be introduced without removing any ions at the Mn site. There are currently no studies reported on doping Li_2MnO_3 with the technique. The cluster expansion technique has been used in other materials such as $La_{1/3}NbO_3$ [44] and Mg-Sn [45].

1.5. Objectives

The objectives of this study are to:

i. perform first-principle calculations on pristine Li_2MnO_3 and determine its structural, mechanical, and electronic properties.
ii. employ cluster expansion to generate new stable phases of doped Li_2MnO_3.
iii. use Monte Carlo (MC) simulations to investigate thermodynamic properties of the new doped Li_2MnO_3 structures.

1.6. Outline

This dissertation entails 5 chapters as follows:

Chapter 1 consists of a general introduction of the study, applications, properties, structural aspects, and intention of the study.

Chapter 2 discusses the theoretical aspects and methodology used throughout this work.

Chapter 3 presents the calculations in detail, results and discussions on structural properties lattice parameters, volume, electronic properties, and mechanical properties of Li_2MnO_3.

Chapter 4 focuses on cluster expansion and Monte Carlo results on the phase stability of doped Li_2MnO_3.

Chapter 5 is the summary and conclusion of the entire study.

Chapter 2 : Methodology

2.1. Introduction

This chapter provides a high-level overview of the computational theories and methodologies employed in this study. Computational simulations are used to investigate a material's structure, chemical, electrical, optical, and magnetic properties. The approach has been used in solid state physics, chemistry, and materials science to predict the real situation by presenting physical systems as models of different systems.

2.2. Density functional theory

Density functional theory (DFT) is a quantum mechanical theory used in physics and chemistry to study the electronic structure and ground-state properties of many body systems. This theory is based on a formula by Hohenberg and Kohn [46] Sham in the 1960s using two theorems to provide the foundation of accurate calculations. The first theorem states that for every system of interacting particles in an external potential $V(r)$, the external potential is uniquely determined by the ground state density. This theorem provides an important basis for simplifying many-body systems using electron density functionals.

$$E = E[\rho] \qquad (2.1)$$

Where E is the total energy and ρ is the electron density.

In DFT, the total electron density is decomposed into one-electron densities composed of one-electron wavefunctions. The idea of using electron density as a fundamental quantity in the quantum mechanical theory of matter dates back to the early days of quantum mechanics in the 1920s, especially the work of Thomas and Fermi [47]. However, in the decades that followed, Hartree-Fock's approach, developed and applied to small molecular systems, became dominant [48]. Calculations on realistic solid-state systems were then out of reach. In 1951, Slater [49] used the electronic gas idea to simplify Hartree-Fock's theory so that the electronic structure of solids could be calculated. Slater's work, which led to the so-called $X\alpha$ method, contributed greatly to the development of electronic state calculations. In solid-state systems, the electron density is a scalar function defined at each point r in real space,

$$\rho = \rho(r) \qquad (2.2)$$

Electron density and total energy depend on the type and configuration of the nucleus. Therefore, one can write

$$E = E\left[\rho(r), \{R_\alpha\}\right] \tag{2.3}$$

where the set $\{R_\alpha\}$ denotes the positions of all atoms in the system under consideration. Equation (2.3) is key to understanding the electronic, structural, and dynamic properties of matter at the atomic level. This allows efficient searches for stable structures and, among other things, the investigation of dynamic processes such as diffusion and reactions of molecules on surfaces. Most of the considerations discussed here are based on the Born-Oppenheimer approximation [50], which assumes that electron motion is infinitely faster than that of atomic nuclei.

In DFT, the total energy is decomposed into three contributions, kinetic energy, Coulomb energy due to classical electrostatic interactions between charged particles in the system and the exchange-correlation energy that captures all many-body interactions.

$$E = T_0 + U + E_{XC} \tag{2.4}$$

Where T_0 is the kinetic energy, U is the Coulomb energy and E_{XC} is the exchange-correlation energy. It is purely classical and includes the electrostatic energy resulting from Coulomb attraction between electrons and nuclei, repulsion between all charges, and repulsion between nuclei. It can be written as follows:

$$U = U_{en} + U_{ee} + U_{nn} \tag{2.5}$$

with

$$U_{en} = -e^2 \sum_\alpha Z_\alpha \int \frac{\rho(r)}{|r - R_\alpha|} dr \quad , \tag{2.6}$$

$$U_{ee} = e^2 \iint \frac{\rho(r)\rho(r')}{|r - r'|} dr dr' \quad , \tag{2.7}$$

$$U_{nn} = e^2 \sum_{\alpha\alpha'} \frac{Z_\alpha Z_{\alpha'}}{|R_\alpha - R_{\alpha'}|} \quad , \tag{2.8}$$

where e proton's elementary charge and $Z'_\alpha$is the atomic number of the atom α. The summation spans all atoms and the integral spans the entire space. If the electron densities, atomic numbers, and positions of all atoms are known, equations (2.6) to (2.8) can be evaluated using classical electrostatics techniques.

In DFT, the ‘real’ electrons of a system are replaced by ‘effective’ electrons with the same charge, mass and density distribution. However, effective electrons move as independent particles within the effective potential, whereas the 'real' electron motion correlates with the motion of all other electrons. T_0 is referred to as the sum of kinetic energies of all effective electrons moving as independent particles. Often this distinction between real and effective electrons is not made explicit.

If each effective electron is described by a single particle wave function, Ψ_i then the kinetic energy of all effective electrons in the system is given by the following equation.

$$T_0 = \sum n_i \int \psi_i^*(r)\left[-\frac{\hbar^2}{2m}\nabla^2\right]\psi_i(r)dr \tag{2.9}$$

Equation (2.9) is the sum of the expectation values of one-particle kinetic energies n_i denotes the number of electrons in the state i, Ψ_i is a single particle wave-function and [$\frac{-\hbar^2}{2m}\nabla^2$] is the time-dependent Schrödinger equation. By construction, the dynamical correlations between the electrons are excluded from T_0.

The third term of Equation(2.4) which is called the exchange-correlation energy, E_{xc} includes all remaining complicated electronic contributions to the total energy. The Hohenberg-Kohn-Sham theorem [51], which is a central part of density functional theory, states that the total energy is at its minimum value for the ground state density and that the total energy is stationary with respect to first-order variations in the density as shown in equation 2.10.

$$\left.\frac{\partial E[\rho]}{\partial \rho}\right|_{\rho=\rho_0} = 0 \tag{2.10}$$

In conjunction with the kinetic energy, the one-particle wave-function $\Psi_i(r)$ generates the electron density.

$$\rho(r) = \sum_i n_i |\psi_i(r)|^2 \tag{2.11}$$

where n_i denotes the occupation number of the eigenstate i, which is represented by the one-particle wave function Ψ_i. By construction, $\rho(r)$ in Equation(2.11) is the exact many-electron density.

The goal of the next step is the derivation of equations that can be used for practical density functional calculations. The variational condition Equation(2.10) can be used to derive the conditions for the one-particle wave-functions that lead to the ground state density. To this

end, one substitutes Equation(2.11) in Equation(2.10) and varies the total energy with respect to each wave function. This procedure leads to the following equations:

$$[\frac{\hbar^2}{2m}\triangle^2 + V_{eff}(r)]\varphi_i(r) = \varepsilon_i\varphi_i(r) \qquad (2.12)$$

Where

$$V_{eff}(r) = V_c(r) + \mu_{xc}[\rho(r)] \qquad (2.13)$$

Equation(2.12) and Equation(2.13) are called the Kohn-Sham [52] equations. The electron density, which corresponds to these wave-functions, is the ground state density which minimizes the total energy. As a consequence of the partitioning of the total energy (2.4), the Hamiltonian operator in the Kohn-Sham Equation (2.12) and Equation (2.13) contains three terms, one for the kinetic energy, the second for the Coulomb potential and the third for the exchange-correlation potential. The kinetic energy term is the standard second-order differential operator of one-particle Schrödinger equations, and its construction does not require specific knowledge of a system.

In contrast, the Coulomb potential operator, $V_c(r)$ and the exchange-correlation potential operator, depend on the specific electron distribution in the system under consideration. The Coulomb or electrostatic potential $V_c(r)$ at point r is generated from the electric charges of all nuclei and electrons in the system. It can be evaluated directly in real space using equation 2.13 as follows:

$$V_C(r) = -e^2\sum_\alpha \frac{Z_\alpha}{|r - R_\alpha|} + e^2\int \frac{\rho(r')}{|r - r'|}dr' \qquad (2.14)$$

In condensed systems it is more convenient to use Poisson's equation shown in 2.15

$$\nabla^2 V_C(r) = -4\pi e^2 q(r) \qquad (2.15)$$

to calculate the electrostatic potential. Here, $q(r)$ denotes both the electronic charge distribution $\rho(r)$ and the positive point charges of the nuclei at positions R_α. The exchange-correlation potential is related to the exchange-correlation energy by equation 2.16 below.

$$\mu_{xc}(r) = \frac{\partial E_{xc}[\rho(r)]}{\partial\rho(r)} \qquad (2.16)$$

Equation (2.16) is formally exact in the sense that it does not contain any approximations to the complete many-body interactions. Therefore, from the above discussions, the Kohn-Sham total energy functional can be expressed as;

$$E = \frac{1}{2}\sum_{occ}\varepsilon_i + U_{nn} - \frac{e^2}{2}\iint\frac{\rho(r)\rho(r')}{|r-r'|}drdr' + E_{xc}[\rho(r)] - \int\rho(r)\mu_{xc}dr \quad (2.17)$$

In practice, however, the exchange-correlation energy (and thus the exchange-correlation potential) is not known, and one has to make approximations which will be discussed in the next section.

2.3. Approximation methods

2.3.1. Local density approximation

Local density approximation (LDA) is a set of approximations to the E_{xc} functional in DFT that is determined by the electronic density at each point in space. LDA demonstrates that E_{xc} is similar to that for a locally uniform electron gas with similar density in regions where there is slow variation in charge density [53]. Several different schemes have been developed to obtain approximate forms of functional exchange-correlation energies. The simplest and most accurate approximation for nonmagnetic systems is to assume that the exchange-correlation energy depends only on the local electron density d(r) around each volume element. The local density approximation (LDA) shows the correct summation rule for exchange-correlated holes [54]. In the local density approximation the exchange-correlation energy is given by equation 2.18:

$$E_{xc}[\rho] \approx \int\rho(r)\varepsilon_{xc}^{0}[\rho(r)]dr \quad (2.18)$$

Where $\rho(r)$ is the electron density while ε_{xc}^{0} denotes the exchange-correlation potential. The exchange-correlation energy arises from the known consequence of multi-electron interactions in constant density electron systems (homogeneous electron gas).

The exchange-correlation energy of a whole molecule or solid is integral to the contributions from each volume element. LDA is based on two basic assumptions**.** LDA is based upon two basic assumptions; the first being that exchange and correlation effects are mainly from the immediate locality of the point r and the second being that these exchange and correlation effects are slightly independent of the alteration of the electron density in the locality of r [55]. The fulfilment of these two conditions results in the same contribution from the volume element dr as if this volume element was surrounded by a constant electron density $\rho(r)$ of the same value within dr.

For this study, the LDA+U method was used which has been widely implemented to correct the approximate DFT xc functional. The LDA+U method works in the same way as the standard LDA method to describe the valence electrons. However, for the strongly correlated electronic states (d and f orbitals), the Hubbard model is implemented for more accurate modelling. Therefore, the total energy of the system (E_{LDA+U}) is typically the summation of standard LDA energy functional (E_{Hub}) for all the states and the energy of the Hubbard functional that describes the correlated states. Based on the simplified $LDA + U$ form, it has been customary to utilise the effective U parameter as shown in equation 2.19, instead of the interaction U parameter.

$$U_{eff} = U - J \tag{2.19}$$

Where the $'J'$ parameter is known as the exchange interaction term which accounts for Hund's rule coupling.

2.3.2. Generalized gradient approximation

Gradient-corrected density functional as suggested by Perdew [56], Becke [57], Wang [58] and Perdew, Burke and Ernzerhof [59] offer a remedy to the LDA discussed above. The basic idea of these schemes is the inclusion of terms in the exchange-correlation expressions that depend on the gradient of the electron density and not only on its value at each point in space. Therefore, these corrections are also sometimes referred to as 'non-local' potentials.

Table 2.1 gives the form suggested by Becke (1988) for the exchange part and Perdew (1986) for the correlation. Energies are given in Hartree atomic units; the units for the electron and spin densities are numbers of electrons / (Bohr radius)^3. The constant b in Becke's formula is a parameter fitted to the exchange energy of inert gases. The explicit form of the functions f and g in Perdew's expression for the correlation energy is given in the original paper by Perdew [59]. While dissociation energies calculated with these corrections rival in accuracy the best post-Hartree-Fock quantum chemistry methods, gradient corrected density functional calculations are computationally much less demanding and more general. Gradient corrected density functionals have been studied extensively for molecular systems, for example by Andzelm and Wimmer [60].

The results are very encouraging, and this approach could turn out to be of immense value in providing quantitative thermochemical data. The one-particle eigenvalues obtained from

the gradient-corrected exchange-correlation potentials are not significantly different from the LDA eigenvalues. Therefore, these potentials do not (and are not intended to) remove the discrepancy between calculated and measured energy band gaps.

Table 2.1: Gradient-correction to the total energy for exchange by Becke and correlation by Perdew.

	$E_{GGA} = E_{LSD} + E_x^G + E_c^G$
Becke (1988) Gradient-corrected exchange	$E_x^G = b\sum_\sigma \int \frac{\rho_\sigma x^2{}_\sigma}{1+6bx_\sigma \sinh^{-1} x_\sigma} dr$ $x_\sigma = \frac{\lvert\nabla\rho\rvert}{\rho_\sigma^{4/3}} \qquad \sigma = \uparrow or \downarrow$
Perdew (1986) Gradient-corrected correction	$E_c^G = \int f\left(\rho_\uparrow, \rho_\downarrow\right) e^{-g(\rho)\lvert\nabla\rho\rvert} \lvert\nabla\rho\rvert^2 dr$

The use of GGA has little influence on local properties and tends to overestimate the bond lengths and cell parameters but does lead usually to a significant improvement in global changes in the total energy, such as those that result when two atoms combine to make a molecule. In this work, we used the Perdew Burke Ernzerhof [59] form of the LDA+U, which was designed to be more robust and accurate for metallic systems.

2.4. Plane-wave pseudopotential method

2.4.1. Plane-waves and pseudopotentials

Plane-waves and pseudopotentials are hallmark methods of calculating the electronic and atomic structures of interfaces, and they also form a very natural alliance. They are so fundamental that their strength and weakness deserve special attention. In the plane-waves pseudopotential method, the model system is constructed in a 3D periodic supercell which allows Bloch's theorem to be applied to the electron wave-functions:

$$\Psi_{n,k}(r) = u_{n,k}(r)^{ikr} \quad (2.20)$$

The function $u(r)$ has the periodicity of supercell. It can be of any suitable mathematical form and usually one chooses a series expansion in terms of a set of basis functions. Plane-waves are used for this expansion so that each single-electron wave-function Ψ_{nk} is written as follows:

$$\psi_{n,k}(r) = \sum u_{n,k}(G) e^{(i(k+G).r)} \quad (2.21)$$

The μ_{nk} are the expansion coefficients. The wave-vectors G are such that the plane-waves are commensurate with the supercell. Both the number of G-vectors in the sum and the number of $k's$ considered should in principle be infinite. The exponential term is a plane-waves of wave-vector k which must be commensurate with the entire system (i.e., not just the periodically replicated cell). For an infinite system, there is an infinite number of k vectors, at each of which solutions for Ψ_{nk} exist. This simply reflects the fact that the number of electrons is infinite. However, a great simplification comes about when one realises that the change in Ψ_{nk} with k becomes negligible for k-points that are close together. This means that one may calculate at a finite number of k-points. We speak of this idea as k-point sampling.

The set of vectors $\{G\}$, on the other hand, should in principle be infinite to obtain an exact representation of the wave-function. This is never necessary because summing over a finite number of G's will yield sufficient accuracy. Plane-waves basis set has many advantages such as unbiased, completeness, single convergence criterion, mathematical simplicity and their derivatives are products in *k*-space and independence of atomic positions. On the other hand, they have disadvantages such as the number of plane-waves needed to be determined by the greatest curvature of the wave-function and empty space having the same quality of representation and cost a region of interest. The advantages speak for themselves, for example the first three indicate that one can always ensure that the basis set is adequate for a calculation by increasing the number of plane-waves until the quantity of interest stops changing. In other words, the quality of the basis set depends on a single parameter, usually expressed as the energy of free electrons whose wave-function has the same wave-vector as the largest wave-vector in the plane-wave basis.

$$E_c = \frac{\hbar^2 (G+k)^2}{2m} \quad (2.22)$$

All plane-waves of ‘energy’ less than the cut-off energy E_c are used in the expansion. The mathematical simplicity of plane-waves means the method is easier to implement, crucially so for the calculation of ionic forces which adds little complexity or cost to the calculation. Equally important in this context is the origin-less nature of plane-waves. Their independence from atomic positions means that the forces do not depend on the basis set, there are no ‘Pulay’ or ‘wave-function’ forces [61]. Even more important, new developments are easiest in plane-wave codes. An idea to calculate property is most rapidly realised in a plane-wave basis and even if other methods catch up in time, the plane-wave approach remains as the reference. From a computational viewpoint, the first of the disadvantages appear to be very serious.

2.4.2. Pseudopotential approximation

The rapid oscillations of the wave-functions near the nucleus, due to the very strong potential in the region and the orthogonality condition between different states, mean that a very large cut-off energy and hence basis set would be necessary. Fortunately, the study of physics and chemistry shows that the core electrons on different atoms are almost independent of the environment surrounding the atom and that only the valence electrons participate strongly in interactions between atoms. Thus, the core electron states may be assumed to be fixed and a pseudopotential may be constructed for each atomic species which takes into account the effects of the nucleus and core electrons [62].

The pseudopotential approximation allows the electronic wave-functions to be expanded using a much smaller number of plane-wave basis states. It is well known that most physical properties of solids are dependent on the valence electrons to a much greater extent than on the core electrons. The pseudopotential approximation exploits this by removing the core electrons and replacing them with strong ionic potential using a weaker pseudopotential that acts on a set of pseudo wave-functions rather than the true valence wave-functions. An ionic potential, valence wave function and corresponding pseudopotential and pseudo wave functions are illustrated in figure 2.1. The valence wave-functions oscillate rapidly in the region occupied by the core electrons due to the strong ionic potential in the region. These regions maintain the orthogonality between the core wave-functions and the valence wave-functions, which is required in Pauli’s exclusion principle [63].

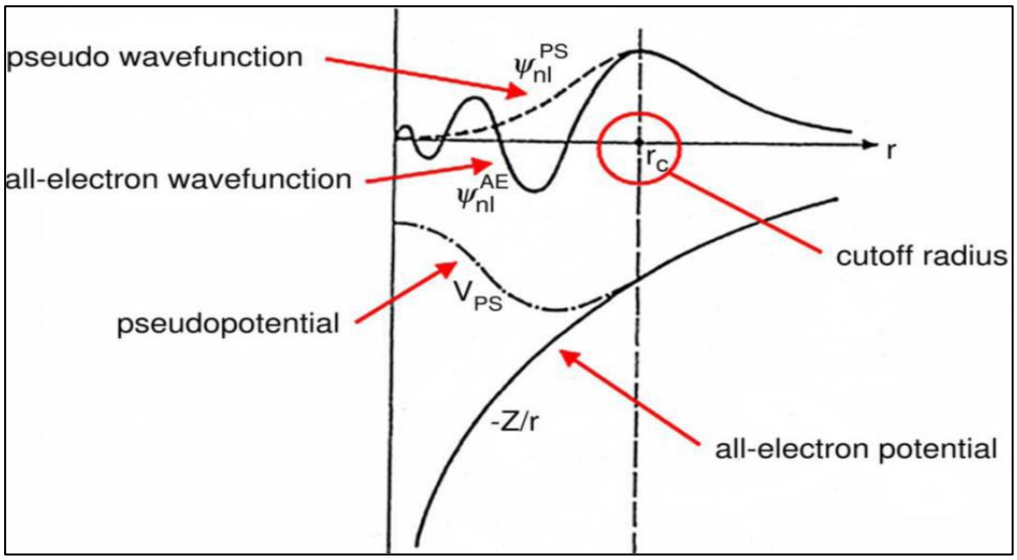

Figure 2.1: Schematic illustration of all-electron (solid lines) and pseudo-electron (dashed lines) potentials and their corresponding wave functions *[64]*

The pseudopotential is constructed in such a way that its scattering properties or phase shifts for the pseudo wave-functions are identical to the scattering properties of the ion and the core electrons for the valence wave-functions, but in such a way that the pseudo-wave-functions have no radial nodes in the core region. The phase shift produced by the ion core is different for each angular momentum component of the valence wave function and so the scattering from the pseudopotential must be angular momentum dependent. The most general form for pseudopotential is

$$V_{NL} = \sum_{lm} |lm\rangle V_l \langle lm| \qquad (2.23)$$

Where $\langle lm|$ are the spherical harmonics and V_l is the pseudopotential for angular momentum l. Acting on the electronic wave function with this operator decomposes the wave function into the spherical harmonics, each of which is multiplied by the relevant pseudo-potential V_l. A pseudo-potential that uses the same potential for all angular momentum components of the wavefunction is called a local pseudopotential. The pseudopotential is just a function of distance from the nucleus. Local potentials can be used to generate any given phase shift for all angular momentum states. However, there are limitations in matching the phase shift to various angular momentum states while preserving the important smoothness and weakness

of the pseudopotential. Without a smooth and weak pseudopotential, it becomes difficult to expand the wave-function using a reasonable number of plane-wave ground states.

2.5. k-sampling

Electronic states are allowed only at a set of *k*-points determined by the boundary conditions that apply to the bulk solid. The density of allowed *k*-points is proportional to the volume of the solid. The infinite numbers of electrons in the solid are accounted for by an infinite number of *k*-points and only a finite number of electronic states are occupied at each *k*-point.

The Bloch theorem [65] changes the problem of calculating an infinite number of electronic wave-functions to one of calculating a finite number of *k*-points. The occupied states at each *k*-point contribute to the electronic potential in the bulk solid so that in principle an infinite number of calculations are needed to compute this potential. However, the electronic wave-functions at *k*-points that are very close are identical. Hence it is possible to represent the electronic wave-functions over a region of *k*-space by the wave-functions at the single k-point. In this case, the electronic states at only a finite number of *k*-points are required to calculate the electronic potential and hence determine the total energy of the solid.

Methods have been devised for obtaining very accurate approximations of the electronic potential from a filled electronic band by calculating the electronic wave-functions at special sets of *k*-points. The two most common methods are those of Chadi and Cohen [66] and Monkhorst and Pack [67]. Using these methods, the electronic potential and the total energy of an insulator can be obtained by calculating the electronic states at a very small number of *k*-points. A denser set of *k*-points are required to calculate the electronic potential and the total energy of a metallic system in order to define the Fermi surface precisely.

However, the computational cost of performing a very dense sampling of *k*-space increases linearly with the number of *k*-points in the Brillouin zone (BZ). Density functional codes approximate these *k*-space integrals with a finite sampling of *k*-points. Special *k*-points schemes have been developed to use the fewest possible *k*-points for a given accuracy, thereby reducing the computational cost. The most commonly used scheme is that of Monkhorst and Pack [67].

2.6. Planewave Pseudopotential Code VASP

In this study, only one planewave pseudopotential code i.e. Vienna Ab-initio Simulation Package (VASP) [68] was employed. In section 2.6.1 below, a brief explanation of the code is given. The VASP code has been used to determine the equilibrium lattice parameters, the heats of formation, the elastic constants and the phonon dispersions for the Li_2MnO_3 structure. The density of states was also calculated using VASP and all the results calculated are presented in chapter 3.

2.6.1. VASP Code

The VASP code [69] is a software package for performing ab-initio quantum mechanical molecular dynamics (MD) using pseudopotentials and plane wave basis sets. The VASP approach uses a finite temperature local density approximation (using the free energy as the variable) and an accurate determination of the instantaneous electronic ground state at each MD step using an efficient matrix diagonalization scheme and an efficient Pulay mixing based on the evaluation. These methods circumvent all the problems encountered with the original Car-Parrinello method. This method is based on the simultaneous integration of the electron and ion equations of motion. Interactions between ions and electrons are described using the ultra-soft Vanderbilt pseudopotential (US-PP) or Projector Augmented Wave (PAW) methods [70]. Both techniques can significantly reduce the number of plane waves required per atom of transition metals and first-row elements. VASP makes it easy to calculate forces and stresses. This can be used to relax atoms to their instantaneous ground state.

2.7. PHONON code

The computational programmes used to determine phonons are VASP, Wien2K, Phonon etc. However, the phonon spectrum can be investigated within the framework of direct methods implemented in the phonon program written by Krzysztof Parlinski [71]. This method is based on the calculation of the interatomic forces in the supercell with the periodic boundary conditions. The Hellmann-Feynmann forces are obtained using one of the density functional theory codes like VASP, Wien2K or SIESTA. The direct method called Phonon code has been used to calculate the phonon dispersion curves and phonon density of states in numerous crystals, multilayers, and surfaces. Phonon code is a software for calculating

phonon dispersion curves, phonon density spectra of crystals, crystals with defects, surfaces and adsorbed atoms on surfaces from either a set of force constants or from a set of Hellmann-Feynman forces calculated within an ab initio program.

Phonons play an important role in solids and determine the thermal properties of all kinds of materials. They also build a crystal structure using one of the 230 crystallographic space groups to find the force constant from the Hellmann-Feynman forces, builds the dynamical matrix, diagonalise it and calculate the phonon dispersion relations and their intensities [72]. Phonon finds the polarization vectors and the irreducible representations (Gamma point) of phonon modes and calculates the total and partial phonon density of states. It plots the internal energy, free energy, entropy, heat capacity and tensor of mean square displacements (Debye-Waller factor). Phonons find the dynamical structure factor for coherent inelastic neutron scattering and the cross-section for incoherent double differential scattering.

2.8. The Cluster Expansion

Modern DFT methods can compute material properties with reasonable to high accuracy (depending on the quality of the approximation of exchange and correlation effects). In contrast, standard DFT applications are limited to unit cells of a few hundred atoms. Brute force modelling of alloys with different atomic concentrations and crystal structures would require a large number of very large supercells. Of course, such a procedure is impractical. Cluster expansion combined with Monte Carlo simulations offers a strategy to overcome this limitation [73].

The idea behind CE is to use a linear combination of interacting building blocks or figures to describe each configuration-dependent property of the system. Configuration is the distribution of atoms on a particular lattice. The energy σ of a particular configuration is then written as a number or sum of pairs, triplets, quadlets, etc. known as clusters. It was demonstrated [73] that such an expansion exists, if mathematically, the expansion goes over all configurations (i.e., atomic distributions). For practical reasons, the expansion must be restricted to relatively small clusters for the expansion to converge numerically. If the input for the convergent cluster expansion is provided by the DFT computation, the accuracy of the

DFT computation can be transferred to systems with 10^4–10^6 atoms. A lot of research has been done on binary bulk systems (e.g., [74] [75] [76]).

2.8.1. Basic Principles of the Cluster Expansion

An optimized cluster expansion produces a set of effective cluster interactions that can be used in large-scale Monte Carlo simulations to study order-disorder phenomena and phase separation processes as a function of temperature. On a basic lattice, various atoms such as A-type and B-type, are distributed on the elementary lattice and define a structure σ, which is a periodic arrangement of A and B atoms. This configuration is described by the pseudo-spin operator

$$\sigma_q = \pm 1 \qquad (2.24)$$

and has a value of +1 if atom A is at position q and -1 if atom B is at position σ.

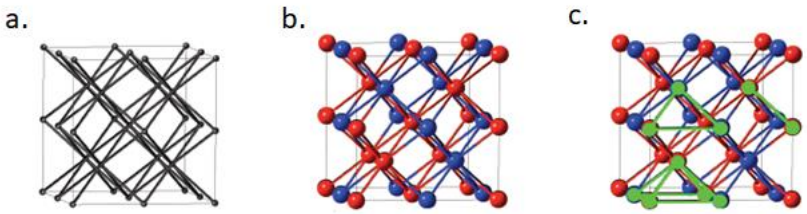

Figure 2.2: a. Basic lattice b. Configuration and c. Cluster interactions

The energy associated with a structure σ (σ) can be described by extending the cluster interactions and their respective interaction energies J using the equation:

$$E(\vec{\sigma}) = J_0 + J_1 \sum_i \sigma_i + \sum_{i>j} J_{ij}\sigma_i\sigma_j + \sum_{i>j>k} J_{ijk}\sigma_i\sigma_j\sigma_k + \cdots \qquad (2.25)$$

The first term J_0 in the equation represents a constant contribution that is independent of configuration. The second term is concentration dependent and is a sum over all N sites of structure σ with onsite energy J_1 times the pseudo spin operator σ at each site i. Further terms describe cluster interactions between multiple locations, such as 2-body interactions J_{ij} and 3-body interactions J_{ijk}. They contain the spin product $\sigma_i\sigma_j$... over all the f vertices of the cluster multiplied by the effective cluster interaction energy J_{ij}... summing all possible

ways in which the cluster can be placed on the lattice of the structure σ. In other words, the energy of structure σ is split into clusters with associated effective interaction energies. A central problem in cluster expansion is to find a universal set of interactions that best describes a particular model. To achieve this, it is convenient to rewrite equation (2.25) in a more compact form

$$E(\vec{\sigma}) = \sum_{C \epsilon \vec{C}} J_C \, \Pi_C(\vec{\sigma}) \tag{2.26}$$

The cluster expansion equation adds up the product of cluster C's interaction energy J_C with its correlation function,

$$\Pi_C(\vec{\sigma}) = N^{-1} \sum_{i=1}^{N} \sum_{k \in C} \prod_{v \epsilon \vec{f}} \sigma_v \tag{2.27}$$

a sum over all the possible ways a cluster C with $\vec{f}$ vertices can be placed on the N sites of the structure. In the correlation function the spin product $\sigma_1 \ldots \sigma_f$ goes over all f vertices of the cluster. Only symmetry inequivalent clusters are now considered and clusters included in an expansion can be collected by the vector $C = \{C_1, \ldots, C_n\}$.

2.8.2. The UNCLE-Code

The current work's CE calculations were performed using the program package UNiversal CLuster-Expansion (UNCLE) [77] which was developed by the group of S. Müller. The code uses genetic algorithms to perform full CE fit and can predict ground states for systems with up to three or more elements. To derive the temperature results, a T>0 Monte Carlo simulation is implemented. This accounts for configuration entropy. The following diagram shows the working scheme of the cluster expansion.

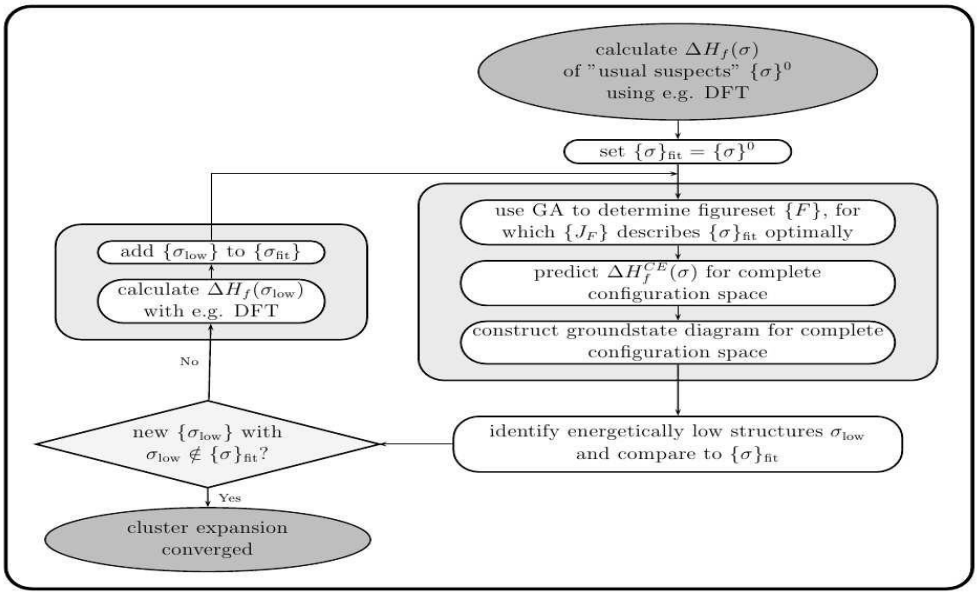

Figure 2.3: Self-consistent working plan as used by UNCLE for the cluster expansion for finding new input structures *[77]*

2.8.3. Selecting the Input Structures

A key task of convergence CE is to ensure that the effective interaction energies associated with the chosen numbers are independent of the training set. To avoid choosing the wrong inputs and misinterpreting the whole system, UNCLE adjusts the energies of other structures on the set of chosen sets. When new structures can be designed and they are energetically below the existing ground state line, they are recomputed by the DFT, resulting in a new set of input structures. This process is repeated with a new set of figures. This cycle is repeated, as shown in figure 2.3 , letting the current cluster expansion itself pick new structures to add to the database. Such an iterative approach has the advantage of producing a reliable ground state line and a set of figures that yields accurate results.

2.8.4. Genetic Algorithm

Hart *et al.* [78] pioneered the use of a genetic algorithm for CE minimization. In this approach, the figure list is represented as a binary string. A figure used is denoted by the value 1, otherwise, the value is 0. Additionally, the interaction energy is also encoded as a binary string. The combination of both binary strings containing the numbers used and their

interaction energies becomes the genetic ‘DNA’ of the solution whose fitness is described by CVS. A high CVS compared to other solutions indicates a poor fit for this solution.

A ‘population’ of different n_{pop} solutions is formed and the fitness of each individual solution is calculated. From these n_{pop} individuals, only the best fit n_{fit} ($0 < n_{fit} < n_{pop}$) individuals are selected and proceed to the next iterative process. Other n_{pop}-n_{fit} solutions are replaced by ‘descendants’ of the best surviving ‘parent’ solution. Their ‘DNA’ is made by two different processes, outlined in Figure 2.4:

•Crossover combines the 'DNA' of two randomly selected 'parent' solutions to create 'offspring' 'DNA'. This consumes the 'DNA' of the 'parent' solution up to the crossover point. Then the ‘DNA’ of the second ‘parent’ is used.

• In mutation, a random binary bit of the ‘DNA’ string is flipped from one state to the other, i.e., $1 \Rightarrow 0$ or $0 \Rightarrow 1$.

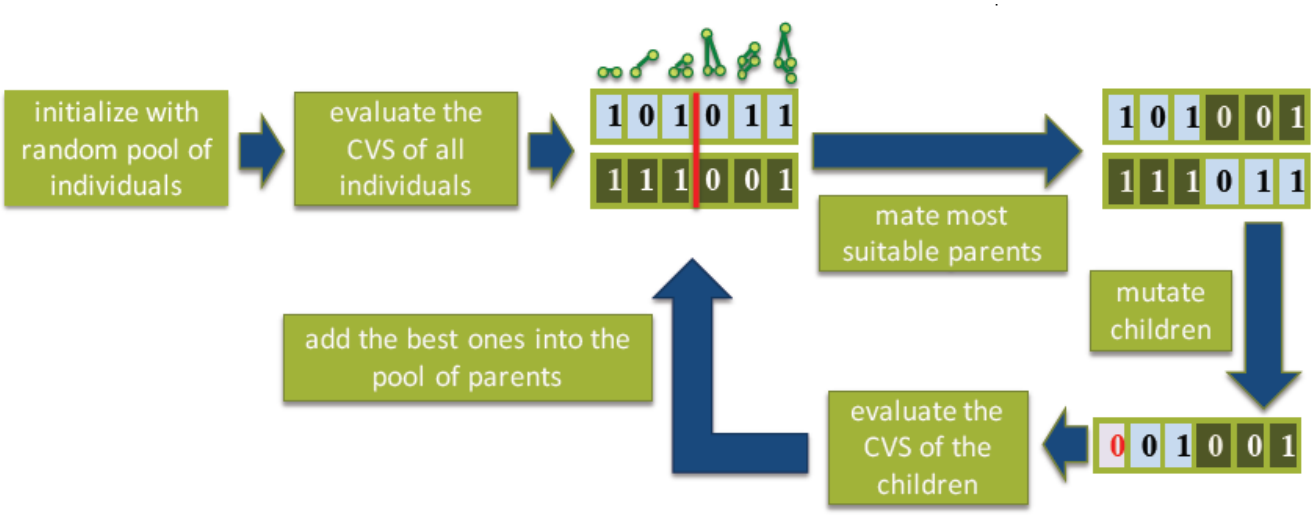

Figure 2.4: Illustration of the genetic algorithm

In an example of crossover is given. The two ‘parent’ solutions marked red, and green are used to generate offspring solutions. The diagram shows the mutation. A random bit in a binary string flips to its opposite state. As a result, the suitability of the new ‘population’ created by this process can be re-evaluated, and the whole procedure repeated until a solution with a sufficiently small CVS is found.

This method will always yield a minimum. However, it is unclear whether a local or global minimum has been discovered. As a result, it is best to perform several separate CEs and choose the solution with the lowest CVS as the final solution. Therefore UNCLE can be set up to do the procedure automatically by performing a number of steps sequentially and only save the best-yielded solution at the end.

2.8.5. Running the Cluster Expansion

After convergence of the genetic algorithm, a set of figures is selected that best represents the system. This set predicted all DFT-derived ground-state energies for the initial input set and produced the lowest SCV. Structures that were not part of the input set of the GA run are now correctly predicted. The ECI derived from the fit is used to describe all possible system structures in the given parent lattice. If the heat of formation of any of these structures is less than the heat of formation of the ground state line defined by the DFT input data, then the structure is included in the extended input set. As a result, the DFT computes the heat of formation and adds it to the list of input structures. A new GA is created using this extended input set. This procedure is repeated until the CE no longer predicts a new ground state. The result is the stable structure of the system and the final ground state line.

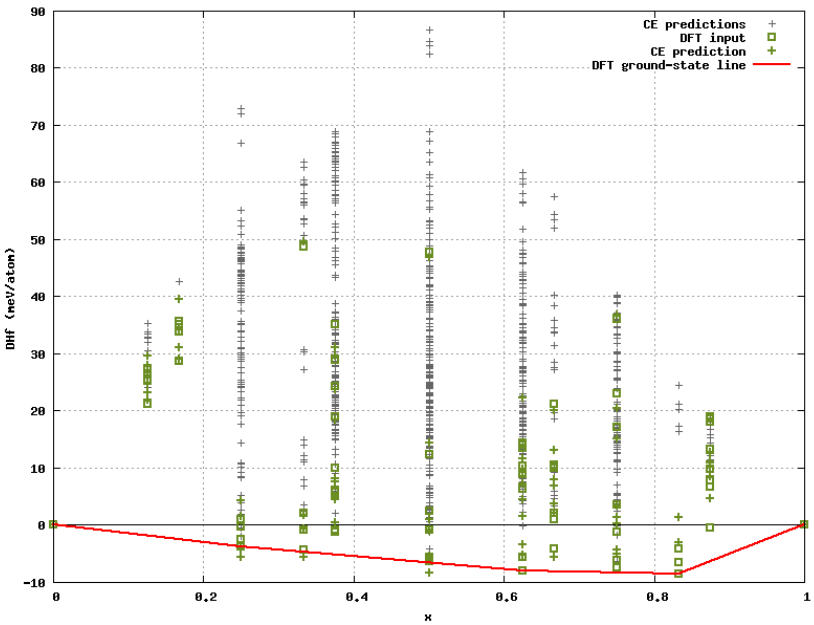

Figure 2.5: Ground state line of the binary $Li_2Mn_{1-x}Ni_xO_3$ systems for a bcc-parent lattice.

At the red line is the defined DFT grounded-state line, where lies the structures with the lowest formation energies, the green blocks denote the DFT results taken as an input for the CE and the green crosses represent the energies predicted by CE.

2.8.5.1. Miscible Constituents

If a model has miscible constituents, the structures with energies close to the ground states, that is those structures with the lowest heat of formation at a given concentration, are the most important ones, and the CE should be the most accurate for those. To achieve this, structures predicted by the CE to be more favourable (with a lower ΔH_f) but not yet in the training set are added to it. This is repeated iteratively until no new structures are predicted to be more favourable by CE than those already included in the training set. At this point, the CE has converged, and the thermodynamically stable structures have been identified among all structures considered by the CE.

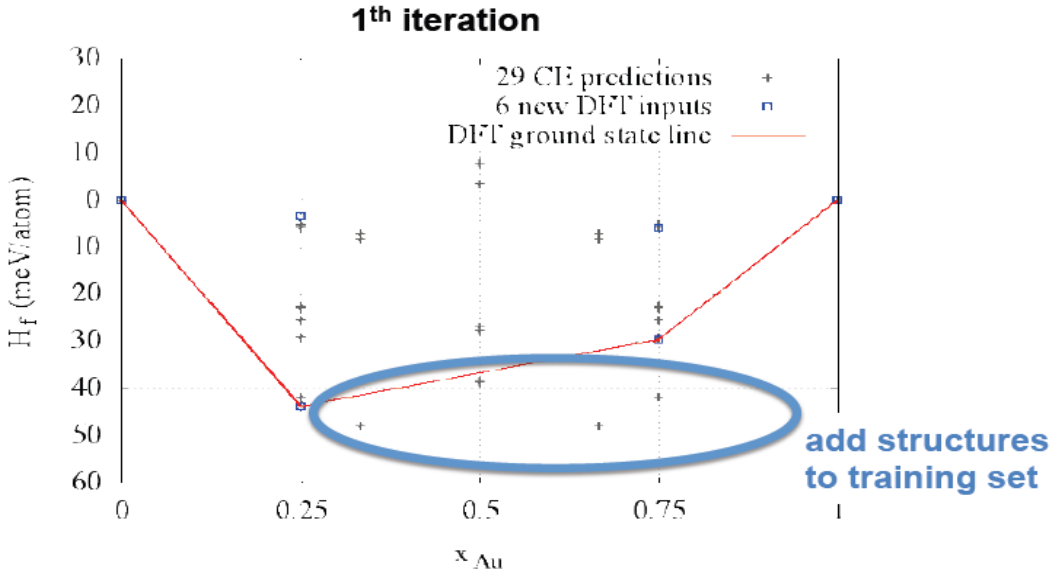

Figure 2.6: Binary ground state diagram illustrating miscible constituent

2.8.5.2. Miscibility Gap

If the model is phase separated, there are no stable ordered structures other than the two pure phases, and all structures are equally important for cluster expansion. Therefore, the process of selecting structures to add to the training set should improve the quality of CE for all structures considered, regardless of their formation energy ΔH_f.

To determine how good (or bad) the energies of the structures are predicted by the cluster expansion the stochastic nature of the genetic algorithm is used. Multiple cluster expansions are run using the same training set. These multiple J's predict the energies of all considered structures and the standard deviation of the predicted energies is calculated. The structures with the highest standard deviations are the ones that explain CE as the poorest. As a result, they are iteratively added to the training set.

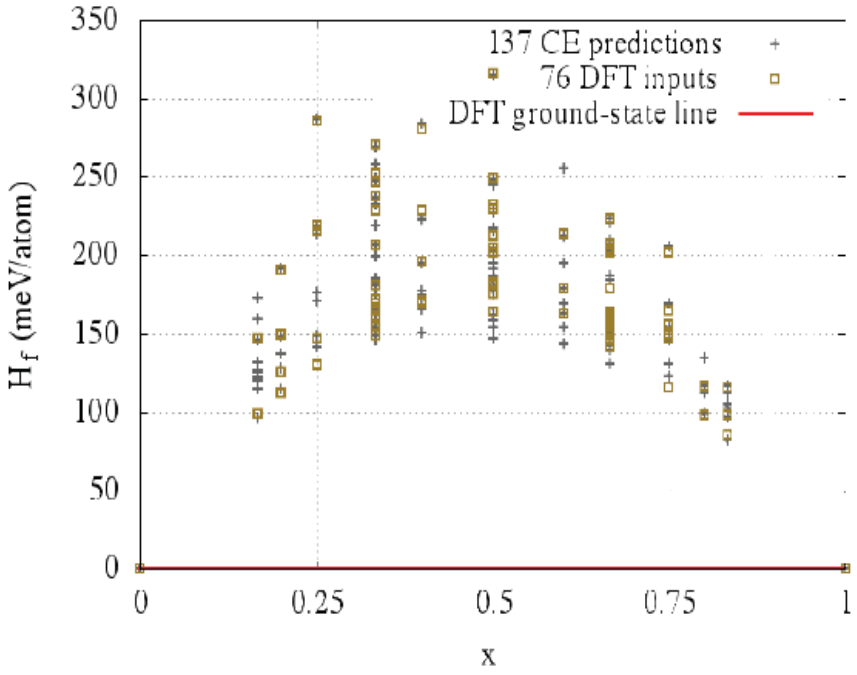

Figure 2.7: Binary ground state diagram illustrating miscibility gap

2.9. Monte Carlo Simulations

The cluster expansion requires effective interaction energies (ECIs), which in the present case were derived from standard DFT calculations. Strictly speaking, DFT total energies are only valid at T=0 K. To include temperature effects, one might think first about configurational entropies, which in this work are included by performing Monte Carlo calculations based on the cluster expansion results. Another very important temperature effect arises from vibrational entropy. This can be derived from DFT calculations of well-chosen displacements, as reported by Reith et al. [79]. This is computationally expensive for the ternary case and is well beyond the scope of a senior thesis. In that case, the ECI is temperature-dependent, so is the overall CE.

In the current work, the Monte Carlo (MC) method is applied without lattice vibrations. The Monte Carlo method (MC) is a probabilistic method and is widely used in statistical thermodynamics. Its main uses are approximating integrals, computing averages, and finding global minima in phase space. Often only 21 samples are considered because it is very difficult or even impossible to cover the entire phase space. This sample selection is the most important point in the simulation. In so-called simple or naive MC, samples are chosen randomly. This method is not very efficient for tasks such as finding global minima, as the selected phase points are distributed throughout the phase space. With such a distribution, the probability of jumping into the global minimum is very small. The improvement is a well-weighted sample of points in phase space, which leads to a global minimum. This way, low-weight points in the phase space are ignored. Such MC simulations are useful for describing thermodynamic systems at finite temperatures as they can derive the constitutive entropy. To illustrate the application of MC in combination with Cluster Extension (CE), the basic principles along with the implementation of MC in the UNCLE code will be described.

2.9.1. Random Walks and Markov chains

As mentioned before, sample selection is a key point for finding the thermodynamic properties of the system under investigation. MC uses a random method of changing points in phase space. By applying the so-called random walk strategy, each point has the same probability of being selected as the next point to be considered. The corresponding transition probability P depends only on the current point in the phase space and not on the previously selected n-2 points. This description of transition probabilities is called a Markov chain.

$$P(K_n = i \mid K_{n-1} = j \mid \ldots \mid K_0 = 1) = P(K_n = i \mid K_{n-1} = j) = P_{ij} \quad (2.28)$$

Assuming that each transition probability P can be written as $P_{ij}(n)$ a matrix containing the transition into each point of phase space can defined as

$$P = \begin{pmatrix} P_{11} & \cdots & P_{1K} \\ \vdots & \ddots & \vdots \\ P_{K1} & \cdots & P_{Kk} \end{pmatrix} \quad (2.29)$$

Since this matrix is probabilistic, two conditions must be met:

1. The elements of the matrix are probabilities, so all elements must be positive, P*ij* ≥0.
2. The probability of changing position in phase space must be 1. This means $\sum_{j=1}^{K} Pij$=1, where *i* is the current point and K is the number of points in phase space.

The next step in the random walkthrough phase space is to define the stationary probability that point i will be occupied after n steps:

$$w_i(n) = P\ (K_n = I) \qquad (2.30)$$

Now, the stationary probability vector w(n) is defined whose components are the probabilities of arriving at each point of the entire phase space,

$$w(n) = (w_1(n), w_2(n) \ldots w_K(n))^T \qquad (2.31)$$

This vector must again satisfy the conditional rule as the transition matrix P ≡ P_{ij}. Knowing the probability w of a particular point in the phase space of step n, the probability of step n+1 is defined as

$$w_j(n+1) = \sum_{i+1}^{K} w_i(n) P_{ij} \qquad (2.32)$$

which –in a matrix notation– looks like

$w(n + 1) = Pw(n)$

The vector **w** can now be constructed for s following steps by

$w(n + s) = P^s w(n)$

which for n=0 is

$w(s) = P^s w(0)$

At this point, by knowing the probabilities of the points in the occupied phase space and the initial transition probabilities, the probability distribution over the phase space after s steps can be predicted. Since each step has the same probability in the random walk approach, each element of the transition matrix and the stationary probability vector has traditionally been of the form

$$P_{ij=}\frac{1}{k}, w_i = \frac{1}{K} \qquad (2.33)$$

To construct an efficient algorithm a weight for the transition to different points in the phase space has to be implemented.

2.9.2. Implementation of the MC Simulation in the UNCLE Code

The UNCLE code allows MC calculations using grand canonicals and canonical ensembles. The system involved in the calculation is a box of atoms over a specified range, subject to periodic boundary conditions. A box is a unit cell. There are different implementations for both grand canonical and canonical calculations.

2.9.3. Grand-canonical Ensemble

In grand-canonical ensembles, the system can be viewed as a crystal of interest associated with a reservoir of atoms that may propagate through the system.

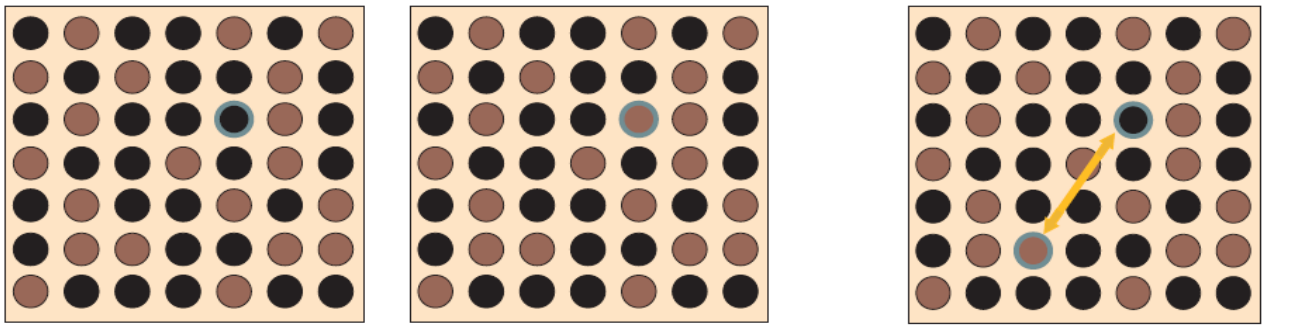

(a) Grandcanonical ensemble (b) Canonical ensemble

Figure 2.8: Visualization of MC steps in UNCLE. A grand canonical simulation changes the properties of the atoms in the crystal. The canonical approach changes the position of two atoms in the crystal

Overall, in both cases, the Boltzmann distributions of the old and new systems are computed and compared to determine if the transition occurs. The number of atoms in the simulation box should remain constant. In other words, adding one atom requires removing another atom. The thermodynamics controlling the propagation of atoms in and out of the box is the chemical potential μ. As the chemical potential of one type of atom in the system increases,

the number of atoms of that type decreases. The reason is that when one atom (such as atom A) is removed from the system and another atom (such as atom B) is added, the chemical potential changes by $\Delta\mu = \mu_A - \mu_B$. where the chemical potentials of μi are atomic species. The transition rate for changing configuration σ to σ' is defined as

$$P^*_{\sigma\sigma'} = \begin{cases} 1 & if\ \ \epsilon < e^{-(\Delta E - \Delta\mu)/kT} \\ 0 & if\ \ \epsilon > e^{-(\Delta E - \Delta\mu)/kT} \end{cases} \qquad (2.34)$$

where $\Delta E = E(\sigma') - E(\sigma)$. That is, if the energy of the system drops more than the change in chemical potential after atom exchange, the step is accepted, otherwise, it is compared with the random number above. The Ising model of cluster expansion allows us to easily change atom types at defined positions. Atoms are randomly selected and changing the spin variable obviously changes the atom type. In the next step, the energies of the simulated boxes were calculated using ECI so that the energy difference ΔE can be calculated. Δμ and the Boltzmann factor are also defined, since the atom-type chemical potential is an essential starting parameter.

2.9.4. Canonical Ensemble

In the canonical ensemble, the conserved quantity is the concentration of each atom type in the simulation box. At each step, the positions of two randomly selected atoms are exchanged. This changes the energy of the composition inside the box and the transition rate can be written as:

$$P^*_{\sigma\sigma'} = \begin{cases} 1 & if\ \ \epsilon < e^{-(E(\sigma') - E(\sigma))/kT} \\ 0 & if\ \ \epsilon > e^{-(E(\sigma') - E(\sigma))/kT} \end{cases} \qquad (2.35)$$

The random walkthrough phase space continues until a selected number of steps are taken or the energy change of the system falls below a certain numerical limit.

2.10. Theoretical background of calculated properties

2.10.1. Heat of formation

Electronic structural calculations of varying rigor are now routinely used to calculate the total energy of materials. This opens up the possibility of estimating the stabilities of structures that are either experimentally unavailable or inaccessible. The heats of formation and associated entropies provide a fundamental understanding on stabilities and phase diagram construction. It is, therefore, critical to consider the heat of formation when researching the cathode material Li_2MnO_3 for lithium-ion batteries. The heat of formation is calculated using the following formula:

$$\Delta H_f = E_c - \sum_i x_i E_i \qquad (2.36)$$

where E_c is the calculated total energy of the compound and E_i is the calculated total energy of element i in the compound. In this study, the equilibrium total energy of Li_2MnO_3 is calculated using VASP. The lower the heat of formation, the more stable the structure.

2.10.2. Elasticity

From the standpoint of material physics, the elastic constants (C_{ij}) contain some of the most vital information that can be easily obtained from ground state total energy calculations. If the elastic constants of a given crystal structure do not obey certain relationships, it cannot exist in a stable or metastable phase. Elastic constants, on the other hand, contain some of the most information about a material's strength against an extremely applied strain and serve as stability criteria in the study of mechanical stability structural transformation [80, 81]. Elastic properties are more important in understanding solid state physical, chemical and mechanical properties. They are related to various fundamental solid-state properties such as equations of states, interatomic potentials, phonon spectra, and lattice constants.

The elastic constants of a material describe the response to an externally applied strain required to sustain deformation and are defined by the bulk modulus (B), elastic modulus (E), and isotropic shear modulus (G). They provide useful information about the strength of the material being investigated. Since first-principles calculations using periodic boundary

conditions assume the existence of a single crystal, all elastic constants can be obtained by direct calculation. The elastic constants calculations were introduced by Born [82]. The Born stability criterion is a set of C_{ij} conditions related to quadratic changes in the internal energy of the forming crystal. Moreover, it was later shown that the region of Born stability is sensitive to the choice of coordinates [83].

Born conditions were found effective only for the unstressed system and inadequate for the stressed system [84]. Barron and Klein pointed out that the standard definition of the elastic constant derived from the Helmholtz free energy is not directly applicable to the study of the stress-strain relationship of a stressed system [85]. However, the elastic constants cannot be used as stability criteria for a stressed system as demonstrated by Wang *et al.* [84]. They proposed using the elastic stiffness modulus as a stability criterion for isotropic stress. For the anisotropic stress, a more general form from the path-dependent finite displacement was derived. Stability criteria are formulated in terms of elastic stiffness coefficients that determine the correct relationship between stress and strain at finite strain by considering both the internal and external work done during the deformation process [86]. This shows that a good generalization of the stress-free elastic constants valid for arbitrary stresses can largely determine the stability analysis.

Bulk modulus [87] is one of the important parameters characterizing the physical properties of material systems, as it also measures the degree of stiffness or energy required to produce a given volumetric strain. The Shear modulus [88] describes the resistance to deformation induced by shear forces, and the elastic modulus reflects a material's resistance to uniaxial stress [89]. The bulk modulus maps the bonding properties of materials and is used as an indicator of material strength and hardness [90]. In addition, Pugh introduced the bulk-to-shear modulus (B/G) ratio of the material. This ratio expresses that the shear modulus and compressive modulus represent the plastic's resistance to deformation and fracture. A higher B/G value indicates ductility, and a low B/G value indicates brittleness. The separation value for brittleness and ductility is 1.75 [91].

2.10.3. Definition of elastic constants

To determine the elastic constants of the crystal, the deformation of the unit cell uses the Bravais lattice vector **R = (a, b, c)** of the unperturbed unit cell **R' = (a`, b`, c`).** generated by the stress matrix

$$R' = R.\begin{pmatrix} 1+e_{xx} & \frac{1}{2}e_{xy} & \frac{1}{2}e_{xz} \\ \frac{1}{2}e_{yx} & 1+e_{yy} & \frac{1}{2}e_{yz} \\ \frac{1}{2}e_{zx} & \frac{1}{2}e_{zy} & 1+e_{zz} \end{pmatrix} \qquad (2.37)$$

The deformation leads to a change in the total energy of the crystal

$$U = \frac{E_{tot} - E_0}{V_0} = \frac{1}{2}\sum_{i=1}^{6}\sum_{j=1}^{6} C_{ij} e_i e_j \qquad (2.38)$$

where E_0 is the total energy of the unstrained lattice, V_0 is the volume of the undistorted cell and the C_{ij} are the elements of the elastic constant matrix with a notation that follows standard convention. Both *i* and *j* run from 1 to 6 in the order {xx, yy, zz, yz, xz, xy}. The elastic tensor has 36 elements, the elastic constants and at most 21 of these are independent.

2.10.4. Calculations of elastic constants

The simplest case is the cubic system which has only three independent constants, C_{11} , C_{12} and C_{44}. This case is used to illustrate the way the stiffness matrix elements may be determined from strain fields of the form (2.34). If the applied strain is e_{xx} = e with all other e_i equal to zero, the energy change is $U = C_{11}e^2/2$. This allows a unique determination of C_{11}. If $e_{yz} = e_{zy} = e/2$, with all other strain components zero, then $U = C_{44}e^2/2$ then C_{44} can be determined independently. The bulk modulus, B, is the response to a uniform compression so applying the strain field $e_{xx} = e_{yy} = e_{zz} = e$ allows the computation of B via the relation

$U = Be^2/2$. Similarly, the shear modulus can be calculated by using the strain field $e_{zz} = e; e_{xx} = e_{yy} = -e/2$, whereupon $U = 3C'e^2/2$. Finally, the off-diagonal stiffness matrix element C_{12} can be calculated using one or other of the relations.

$$B = \frac{1}{2}(C_{11} + 2C_{12}) \tag{2.39}$$

$$C' = \frac{1}{2}(C_{11} - C_{12}) \tag{2.40}$$

Using both relations helps to check the accuracy of the calculations separately. The symmetric general formulation for the calculation of the elastic constants from the total energy calculation is given by Le Page and Saxe [92].

2.10.5. Elastic Constant Stability Conditions

The elastic properties of single crystals are described by the elements Cij of the elastic tensor. For any material, both stress and strain have 3 tensile and 3 shear components, for a total of 6 components. Therefore, according to the theory of elasticity, a 6 x 6 symmetric matrix with 36 elements is required to describe the relationship between stress and strain. Due to the structural symmetry of crystals, some of the matrix elements are equal while others are fixed at zero.

Monoclinic crystals have 13 independent elastic constants(C_{11}, C_{22}, C_{33}, C_{12}, C_{13}, C_{23}, C_{44}, C_{55}, C_{66}, C_{15}, C_{25}, C_{35}, C_{46})**.** A monoclinic phase is considered stable if the following mechanical stability criteria are met**.** The monoclinic Born mechanical stability criterion [93] is given by:

$$C_{ij} > 0\ , [C_{11} + C_{22} + C_{33} + 2(C_{12} + C_{13} + C_{23})] > 0,\ (C_{33}C_{55} - C_{35}^2) > 0,$$

$$(C_{22} + C_{33} - 2C_{23}) > 0\ ,\ [C_{22}(C_{33}C_{55} - C_{35}^2) + 2C_{23}C_{25}C_{35} - C_{23}^2C_{55} - C_{25}^2C_{33}] > 0,$$

$$\{2[C_{15}C_{25}(C_{33}C_{12} - C_{13}C_{23}) + C_{15}C_{35}(C_{22}C_{13} - C_{12}C_{23}) + C_{25}C_{35}(C_{11}C_{23} - C_{12}C_{13})] - [C_{15}^2(C_{22}C_{33} - C_{23}^2) + C_{25}^2(C_{11}C_{33} - C_{13}^2) + C_{35}^2(C_{11}C_{22} - C_{12}^2)] + gC_{55}\} > 0 \tag{2.41}$$

$$g = C_{11}C_{22}C_{33} - C_{11}C_{23}^2 - C_{22}C_{13}^2 - C_{33}C_{12}^2 + 2C_{12}C_{13}C_{23}, \text{ [94]}$$

The calculated elastic constants of the monoclinic phase allow macroscopic mechanical parameters, namely the isotropic bulk (B) and shear (G) moduli, to be obtained with the Voigt(V) approximation. The Young's modulus and Poisson's ratio of a crystal can be obtained by the following equations:

$$E = \frac{9BG}{3B+G}, \nu = \frac{1}{2}\left[\frac{B_X - (2/3)G_X}{B_X - (1/3)G_X}\right] \quad (2.42)$$

$$\Delta_P = \frac{C_{33}}{C_{11}}, \ \Delta_{S1} = \frac{C_{11} - C_{13}}{2C_{44}}, \ \Delta_{S2} = \frac{2C_{44}}{C_{11} - C_{12}} \quad (2.43)$$

$$B_V = \frac{1}{9}(C_{11} + C_{22} + C_{33}) + \frac{2}{9}(C_{12} + C_{23} + C_{13}) \quad (2.44)$$

$$G_V = \frac{1}{15}(C_{11} + C_{22} + C_{33}) - \frac{1}{15}(C_{12} + C_{23} + C_{13}) + \frac{1}{5}(C_{44} + C_{55} + C_{66}) \quad (2.45)$$

$$\frac{1}{B_R} = (S_{11} + S_{22} + S_{33}) + 2(S_{12} + S_{23} + S_{13}) \quad (2.46)$$

$$\frac{1}{G_R} = \frac{4}{15}(S_{11} + S_{22} + S_{33}) - \frac{4}{15}(S_{12} + S_{23} + S_{13}) + \frac{1}{5}(S_{44} + S_{55} + S_{55}) \quad (2.47)$$

Where B_V, B_R, G_V and G_R are Voigt bulk modulus, Reuss bulk modulus, Voigt shear modulus and Reuss shear modulus respectively. However, S_{ij} is the elastic compliance constant and can be obtained from elastic constants.

The Hill approach is approximated as the average of Voigt and Reuss. The bulk and shear moduli of a material according to the Voigt-Reuss-Hill approximation [95] can be expressed as

$$B_H = \tfrac{1}{2}(B_R + B_V) \qquad (2.48)$$

and

$$G_H = \tfrac{1}{2}(G_R + G_V) \qquad (2.49)$$

The elastic modulus E is defined as the ratio of stress and strain and is used to provide a measure of the stiffness of a solid. The higher the E value, the harder the material. Poisson's ratio (v) refers to the ratio of transverse shrinkage strain to longitudinal strain during stretching and reflects the stability of a crystal against shear. Therefore, the higher the Poisson's ratio, the better the ductility of crystalline metals at low temperatures. However, it is recognized that the bulk modulus B is a measure of resistance to volume change induced by external pressure. The macroscopically measurable quantities of a material are the shear modulus, i.e., the isotropic response to shear, the elastic modulus corresponding to the stress-strain ratio of tensile force, the bulk modulus, Poisson's ratio, and the anisotropy constant. All of these are important for technical and engineering applications.

2.10.6. Phonon dispersion curves

The phonon dispersion curve is defined as the k-wave vector dependence of the normal mode frequencies ω(k,j) for all branches and selected directions in the crystal. They play important roles in several physical properties of condensed matter physics, including mechanical stability, electrical conductivity, and thermal conductivity. These properties indicate excited states in the quantum mechanical quantization of the vibrational modes of the elastic structure of the interacting particles. The bifurcation of phonon dispersion behaviour reflects certain features of the crystal structure and interatomic interactions. However, they provide the most comprehensive and detailed information on the dynamic properties of crystals. The phonon vibration frequency is calculated as follows [96, 89]:

$$\omega = v_s q \qquad (2.50)$$

where v_s is the speed and q is the wave-vector of the lattice vibrations.

Crystals with more than one type of atom will display two types of vibrations ,i.e., optical Mode and acoustic Mode. Optical phonons arise from out-of-phase vibrations between adjacent atoms in the unit cell, whereas acoustic phonons cause in-phase vibrations. Also, the frequency of the acoustic mode is zero at q = 0 (the centre of the Brillouin zone (Γ)), but the frequency of the optical mode is not. Acoustic and optical modes are divided into longitudinal and transverse modes. These are abbreviated as Longitudinal Acoustic (LA), Transverse Acoustic (TA), Longitudinal Optical (LO), and Transverse Optical (TO). Acoustic modes display a linear relationship between frequency and long-wavelength phonon wavevectors. Positive vibration frequencies indicate system stability and negative vibration frequencies (soft modes) indicate mechanical instability.

2.10.7. Density of states

The density of states (DOS) of a system represents the number of states available per energy interval at each energy level. DOS indicates how dense the quantum states are in the system. Integration of DOS over the energy range yields a set of states:

$$N(E) = \int_{E}^{\Delta E} g(E)dE \qquad (2.51)$$

where N (E) represents the charge carrier density and g(E)dE represents the number of states between E and dE. The density of states allows integration with respect to electronic energies rather than integration over the Brillouin zone. Widely used for rapid visual analysis of electronic structures. Properties such as the width of the valence band, the energy gap of insulators, and the number of significant feature strengths are useful for the interpretation of experimental spectroscopic data. The most accurate method used is based on linear or quadratic interpolation of the band energies between reference points in the Brillouin zone. The most popular and reliable technique is based on tetrahedral interpolation. The most popular and reliable technique is based on tetrahedral interpolation. However, it is not suitable for the Monkhorst Pack grid of special points [67]. The VASP code uses a simplified linear interpolation scheme. This method is based on linear interpolation of the parallelepiped formed by the points of the Monkhorst Pack set, followed by histogram sampling of the resulting set of band energies. The literature shows that DOS is essential for determining the stability trend of structures with the same composition with respect to E_F. Theory holds that the elements with the highest density of states near E_F are the least stable, while those with

the lowest density of states are the most stable [97, 98]. Moreover, the element with a greater contribution at the E_F is the most active or reactive element.

Chapter 3 : Structural, electronic and mechanical properties of bulk Li_2MnO_3

The purpose of this chapter is to present the ab initio first-principle results of Li_2MnO_3 that have been obtained. Particularly, equilibrium lattice constants, heats of formation, density of states (DOS), elastic properties and phonon dispersion curves. The cell parameters and heats of formation play an important role in determining the structural stability of the system. These were determined by performing geometry optimization allowing the lattice and cell volume to change. Firstly, structural optimization calculations were performed to achieve the minimum total energy or ground-state before any properties can be calculated. Secondly, DOS calculations were performed to determine the nature of the crystal and its electronic conductivity. Lastly, the mechanical stability of Li_2MnO_3 was investigated using phonon dispersion curves and elastic constants. Phonon dispersion curves and elastic properties are performed under PHONON and VASP code discussed in chapter 2.

3.1. Cut-off energy and the *k*-point convergence

3.1.1. Cut-off energy

The cut-off energy (eV) is necessary to determine the accurate ground state for the system. To determine the appropriate cut-off energy (eV) of the Li_2MnO_3 structure, single-point energy calculations were performed for different kinetic energy cut-offs at the default number of *k*-points mesh for the system within generalized gradient approximation in the form of Perdew-Burke-Ernzerhof (GGA-PBE) correlation functional. The energy cut-off (eV) was then varied from 100 eV up to 900 eV with an increase of 100 eV each time at a fixed *k*-points mesh. In figure 3.1 the total energy (eV) versus the kinetic energy cut-off (eV) gave a constant slope with an energy change of less than 1 meV/atom which was found from 500 eV, then the cut-off energy of 500 eV was chosen and used throughout the study as the energy convergence.

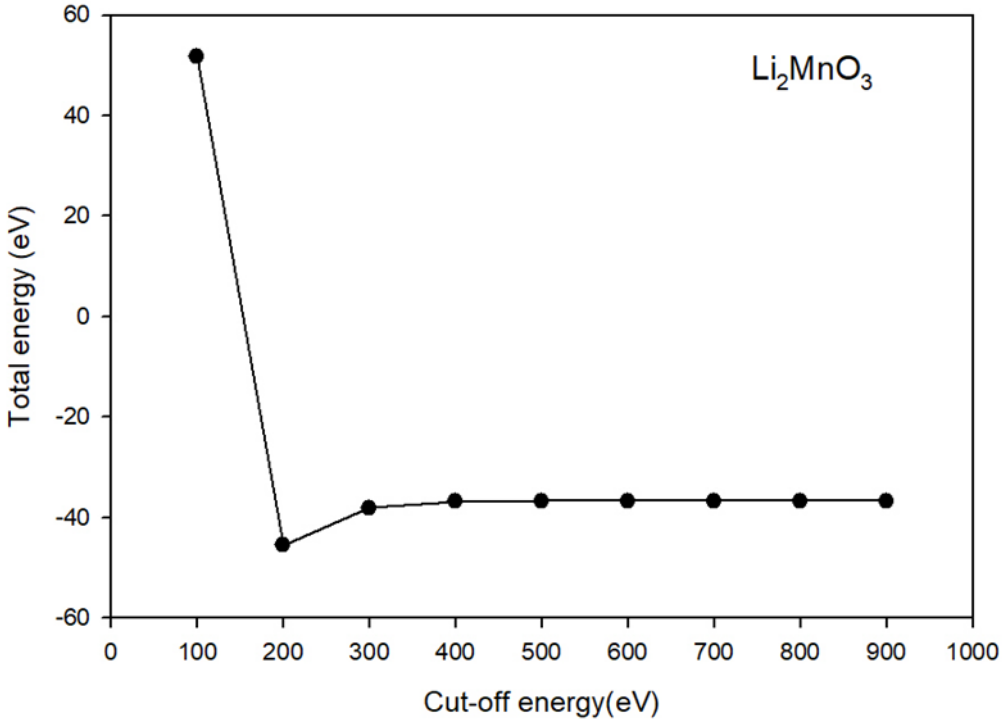

Figure 3.1: The variation of total energy as a function of cut-off energy

3.1.2. *k*-points

In this subsection, the convergence of the total energies (eV) with respect to the *k*-point mesh is illustrated in Figure 3.3. The total energy (eV) calculations were set at fixed cut-off energy of 500 eV for each structure while the number of *k*-points mesh was varied. The total energy (eV) with respect to the number of the *k*-points mesh was considered converged when the energy change per atom (between two consecutive points) was within 1meV per atom. The separations were varied to find a suitable number of *k*-points mesh of the Li_2MnO_3 structure. The *k*-points mesh of 5x5x5 was chosen for the structure and used throughout the study.

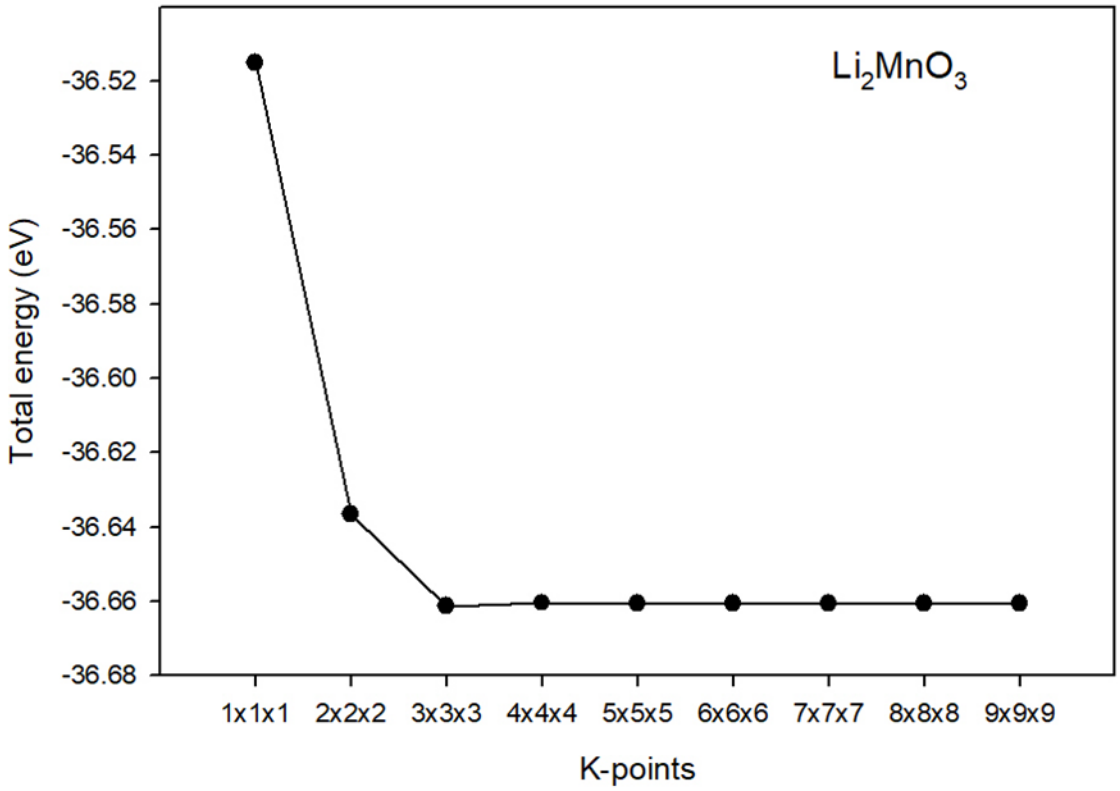

Figure 3.2: The variation of total energy as a function of *k*-points

3.2. Geometry optimization

The geometry optimization for the Li_2MnO_3 structure was performed within the generalized gradient approximation (GGA) using the energy cut-off of 500 eV for all the structures. The lattice parameters of the structure were allowed to vary, thereby minimizing the structure to its stable form. The calculations were carried out until the system reached convergence. Total energy was used to calculate the heat of formation for the optimized structures, which was discussed in detail in the following section.

3.3. Heat of formation of Li_2MnO_3 structure

Table 3.1 lists the calculated and experimental lattice parameters, cell volumes and heats of formation of Li_2MnO_3. The calculated lattice parameters agree well with the experimental results. The heat of formation (ΔH_f), which is the heat change when one mole of a compound is formed from the elements in their stable states, is essential in determining the structural stabilities of different crystal structures. The predicted ΔH_f value is given in table 1, the lower the heat of formation, the more stable the structure. The calculations have predicted

structures with negative heat of formations, so the Li_2MnO_3 system is thermodynamically stable.

Table 3.1: The equilibrium lattice parameters and heats of formation of bulk Li_2MnO_3

	Lattice parameters(Å)		**ΔH_f (KJ/mol)**	**Volume (Å^3)**
	VASP	**EXP [28]**	**VASP**	**VASP**
Li_2MnO_3	a=4.9845	4.8715	-874.417	204.7994
	b= 8.6121	8.5320		
	c=5.0653	5.0300		

3.4. Density of states

Figure 3.3 shows the total density of states (TDOS) and partial density of states (PDOS) of Li_2MnO_3. The DOS calculations were calculated using the spin polarised local density approximation with Hubbard corrections (LDA+U). The high spin states are shown on the positive scale while the lower spin states are seen on the negative scale. Figure 3.3a indicates the total density of states and Figures 3.3b-d show partial densities of states of O, Li and Mn respectively. The total contributions of all atoms in the structure are indicated by the TDOS, whilst the PDOS indicates the contribution of individual atoms.

It can be noted that the total and partial DOS are separated forming a small opening (pseudogap or band gap) near the Fermi level (E_f). The aspects of pseudo and band gaps are necessary for stability, where the shift of the E_f with respect to the gaps plays an essential role in stability and change of coordination within the system. It is observed that, Li *p*-states give a large contribution to the total density of states around the fermi level, and minimal contribution from Mn and O states. The total DOS indicates that the p orbitals of Li and the O dominate at the Fermi energy level and the d orbital of Mn. Hence, from the total density of states (TDOS), it can be deduced whether the structure is metal, semi-conductor or insulator by measuring its band gaps. The gap in the conducting band at the right side of the Fermi level was found to be 1.89 eV, this means that the material is semiconducting. The

value of the bandgap is in excellent agreement with other reported values [23]. By comparing this bandgap with those of other cathodes, such as $LiMnPO_4$ (3.948 eV) and $LiFePO_4$ (3.29 eV), it is clear that Li_2MnO_3 will have a higher conductivity [17, 99].

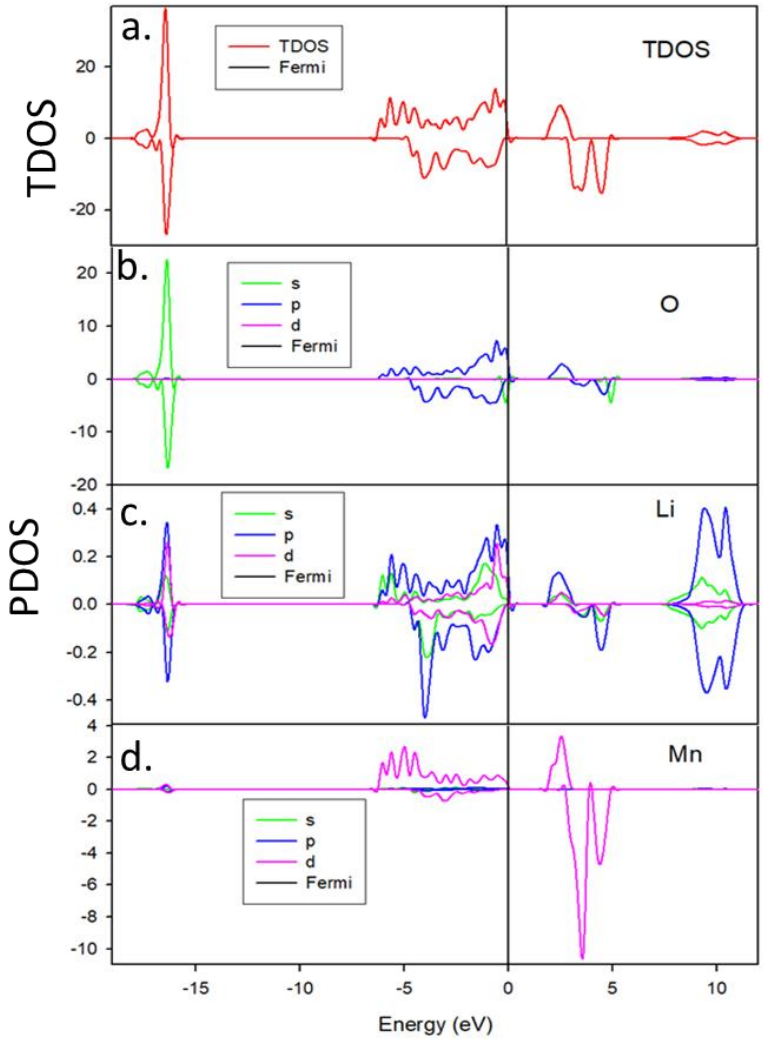

Figure 3.3: a. TDOS for bulk Li_2MnO_3 b. PDOS for O c. PDOS for Li and d. PDOS for Mn

3.5. Elastic properties

The elastic constants and moduli of the Li_2MnO_3 structure were investigated within the density functional theory (DFT) in the framework of GGA. The plane-wave cut-off energy was 500 eV and the convergence of the calculations is 1meV/atom. The knowledge of elastic constants is vital for many practical applications related to the mechanical properties of solids, for example, thermoelastic stress, internal strain, and fracture toughness. Elastic constants

determine the response of crystal to external forces. They play an important role in determining the strength of the material.

The elastic properties of solids are important hence they are related to various fundamental properties, equation of state, phonon spectra etc. The elastic constants for the monoclinic structure Li_2MnO_3 and the bulk modulus (*B*), shear modulus (*G*), Young's modulus (*E*) and Pugh ratio (B/G) were calculated, and they are all summarized in table 2 and 3.

The monoclinic systems have 13 independent elastic constants (C_{11}, C_{22}, C_{33}, C_{12}, C_{13}, C_{23}, C_{44}, C_{55}, C_{66}, C_{15}, C_{25}, C_{35}, C_{46}). The Born mechanical stability criteria for a monoclinic system [100] is given by:

$$C_{ij} > 0, \; [C_{11} + C_{22} + C_{33} + 2(C_{12} + C_{13} + C_{23})] > 0, \; (C_{33}C_{55} - C_{35}^2) > 0, \; (C_{44}C_{66} - C_{46}^2) > 0,$$

$$[(C_{22} + C_{33} - 2C_{23}) > 0, \; [C_{22}(C_{33}C_{55} - C_{35}^2) + 2C_{23}C_{25}C_{35} - C_{23}^2C_{55} - C_{25}^2C_{33}] > 0,$$

$$\{2[C_{15}C_{25}(C_{33}C_{12} - C_{13}C_{23}) + C_{15}C_{35}(C_{22}C_{13} - C_{12}C_{23}) + C_{25}C_{35}(C_{11}C_{23} - C_{12}C_{13})] - [C_{15}^2(C_{22}C_{33} - C_{23}^2) + C_{25}^2(C_{11}C_{33} - C_{13}^2) + C_{35}^2(C_{11}C_{22} - C_{12}^2)] + gC_{55}\} > 0$$

$$g = C_{11}C_{22}C_{33} - C_{11}C_{23}^2 - C_{22}C_{13}^2 - C_{33}C_{12}^2 + 2C_{12}C_{13}C_{23}, \; [94].$$

From the calculated elastic constants, the mechanical parameters such as the bulk, shear, Young's modulus and Poisson's ratio have been determined using the Voigt- Reuss- Hill. The modulus is used to describe the elastic behaviour of materials.

Pugh introduced the ratio of bulk to shear modulus (B/G) [91] of a material. The ratio expresses that the shear and bulk moduli signify the resistance to deformation of plastic and resistance to fracture. A high B/G value denotes ductility, whereas a low B/G value indicates brittleness. The value separating brittleness and ductility is 1.75 [101]. The results show that the B/G ratio for Li_2MnO_3 is 1.4801, therefore the system is brittle. The structure is mechanically stable since the mechanical stability criterion for a monoclinic structure.

Table 3.2: List of elastic constants for bulk Li_2MnO_3

	VASP	Exp [102]
C_{11}	271.51	269
C_{12}	67.75	48
C_{13}	38.22	35
C_{15}	16.19	
C_{22}	275.93	274
C_{23}	39.96	34
C_{25}	-9.90	
C_{33}	213.87	220
C_{35}	2.61	
C_{44}	52.13	79
C_{46}	-12.19	
C_{55}	55.11	81
C_{66}	103.02	105

Table 3.3: Bulk, Shear, Young's Modulus and B/G for bulk Li_2MnO_3

	VASP	**EXP [103]**
B	115.51	113
G	78.04	83
E	219.56	
$\frac{B}{G}$	1.4801	1.3614

3.6. Phonon dispersion curves

The study of phonons is an essential part of solid-state physics, since phonons play a major role in numerous physical properties of the solids, including the material's thermal conductivity. Particularly, the properties of long-wavelength phonons give rise to sound in solids. Phonons are the quantum mechanical equivalent of a type of vibrational motion known as a normal mode in classical mechanics, in which all parts of a lattice oscillate at the same frequency. The normal modes are the elementary vibrations of the lattice [104].

The phonon dispersion curves for Li_2MnO_3 structures were calculated using the PHONON code by Parlinski as implemented in MedeA software, which allows phonon dispersion curves and thermodynamic properties such as vibrational heat capacity at constant volume, vibrational internal energy, entropy and free energy to be calculated [105]. Figure 3.4 demonstrates the phonon spectra for Li_2MnO_3, all vibrations are positive suggesting that Li_2MnO_3 is vibrationally stable. The results are consistent with the calculated elastic constants.

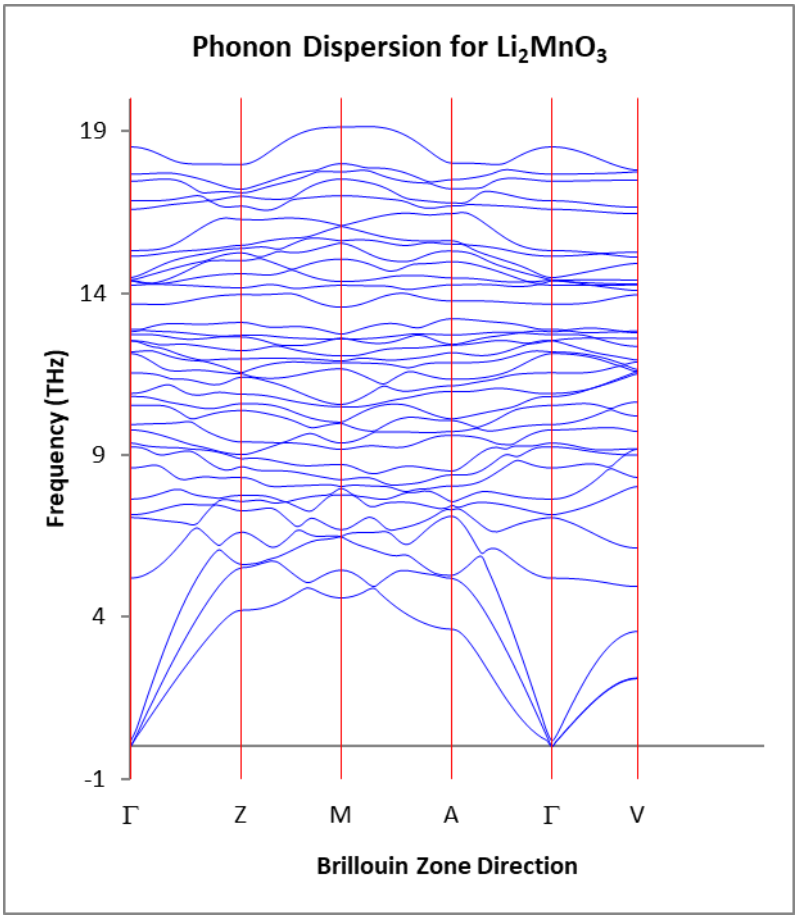

Figure 3.4: Phonon dispersion curves for bulk Li_2MnO_3

3.7. Discussion

In this chapter, a first-principle study on the cathode material Li_2MnO_3 was presented. The equilibrium lattice parameters were performed using the VASP code within a generalized gradient approximation. The lattice parameters were found to be in good agreement with available experimental data and the negative heat of formation suggests that the structure is thermodynamically stable. Electronic density of states calculations were performed using density functional theory with Hubbard corrections. The structure was found to have a band gap of 1.8863 eV and this implies that the system is semiconducting in nature. The band gap of Li_2MnO_3 is smaller than bandgap of other cathodes, such as $LiMnPO_4$ (3.948 eV) and $LiFePO_4$ (3.29 eV) [17, 99], this means that LMO will have a higher electronic conductivity compared to these cathodes. The phonon dispersion curves showed no negative vibration

suggesting vibrational stability. The elastic constants of Li_2MnO_3 satisfied all the necessary conditions for mechanical stability.

Chapter 4 : Cluster Expansions and Monte Carlo Simulations for $Li_2TM_{1-x}Ni_xO_3$ systems (TM= Ni, Co, Cr, Ru) where $0 \leq x \leq 1$

4.1. Introduction

The practical limitations of Li_2MnO_3 as cathode material in lithium-ion batteries have ignited significant interest in searching for new cathode materials. $Li_2Mn_{1-x}TM_xO_3$ is an attractive new class of cathode materials with promising electrochemical performance. In the current chapter, accurate and efficient cluster expansion energy models for $Li_2Mn_{1-x}Ni_xO_3$, $Li_2Mn_{1-x}Co_xO_3$, $Li_2Mn_{1-x}Cr_xO_3$ and $Li_2Mn_{1-x}Ru_xO_3$ systems were developed. Monte Carlo simulations were performed to investigate the structures of $Li_2Mn_{1-x}Ni_xO_3$, $Li_2Mn_{1-x}Co_xO_3$, $Li_2Mn_{1-x}Cr_xO_3$ and $Li_2Mn_{1-x}Ru_xO_3$ at higher temperatures.

4.2. Simulation procedure

The CE method enables the determination of stable multi-component crystal structures and ranks metastable structures based on the heat of formation while retaining the predictive power and accuracy of density functional methods. The ground-state phase diagram produced a variety of structures with varying concentrations and symmetries. This fitting scheme ran for 10 iterations, adding a maximum of 5 structures in each iteration, and starting from an initial training set of 5 structures. The iterations continue until the energies of all structures are predicted by the cluster expansion which is greater than the energy calculated for the structure of the ground state line at each sampled concentration. The ground-state search of binary compounds by total-energy calculations and diagrammatic approaches suffers heavily from the need that the small group of crystallographic configurations considered must include the most stable one. The combined use of cluster expansion and Monte Carlo simulations can eliminate this problem, as will be demonstrated.

4.3. Results

The binary ground state diagrams in figures 4.1.- 4.4. shows that all the generated phases at T=0 K. The green squares represent DFT enthalpies of formation of the training set, green crosses CE predicted enthalpies of formation of the training set and grey the CE predicted enthalpies of formation of all other structures considered by the cluster expansion.

4.3.1. Search for the Ground States (Cluster Expansion)

4.3.1.1. $Li_2Mn_{1-x}Ni_xO_3$

Figure 4.1 shows a binary ground state diagram of the $Li_2Mn_{1-x}Ni_xO_3$ system. The diagram shows that the system has generated structures both in the negative and positive heats of formation. The diagram further illustrates that the system prefers phases that are Ni deficient, the system is more stable at approximately X=0.2, which agrees with results obtained by Ye *et al.* [106]. As mentioned before the most important structures are those that lie along the ground state line. The structures are listed in Table *4.1* and the most thermodynamically stable structure was found to be $Li_2Mn_{0.83}Ni_{0.17}O_3$ with space group C2.

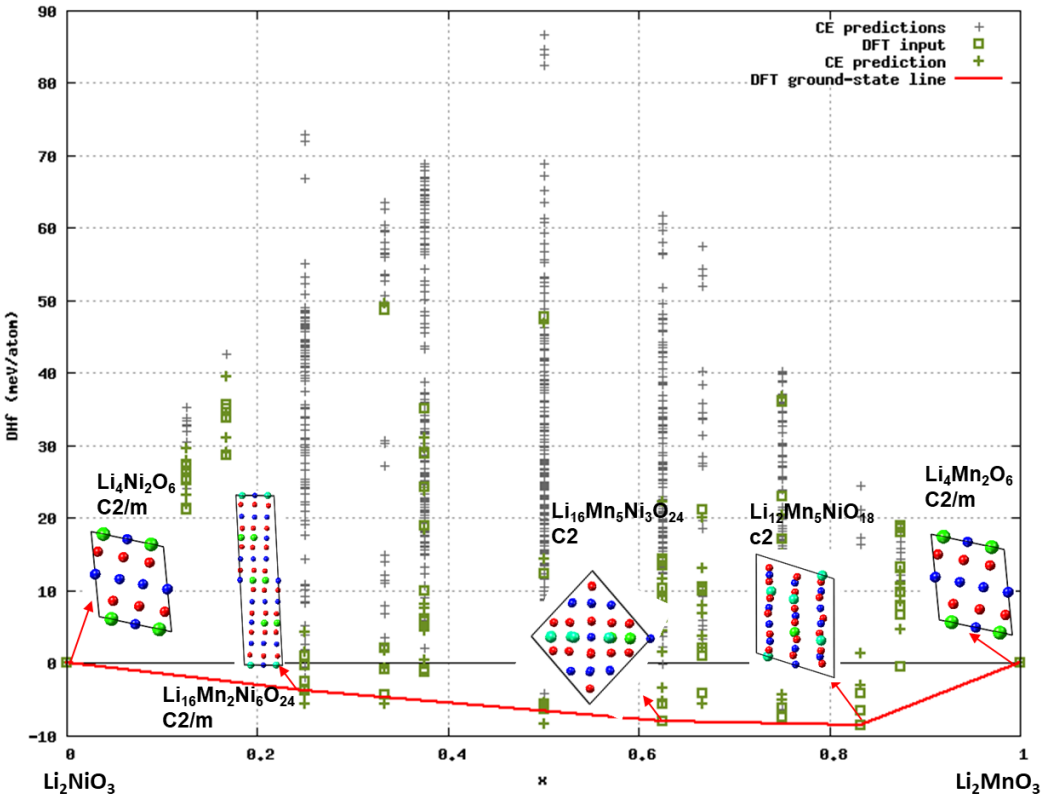

Figure 4.1: The ground state line of the $Li_2Mn_{1-x}Ni_xO_3$ system: the heat of formation versus Ni concentration and ground state structures.

Table 4.1: Stable structures of $Li_2Mn_{1-x}Ni_xO_3$ along the ground state line.

Structural formula	**Space group**	**Formation energy (eV/atom)**
Li_2NiO_3	C2/m	-32.91
$Li_2Mn_{0.25}Ni_{0.75}O_3$	C2/m	-32.30
$Li_2Mn_{0.625}Ni_{0.375}O_3$	C2	-36.37
$Li_2Mn_{0.83}Ni_{0.17}O_3$	C2	-37.88
Li_2MnO_3	C2/m	-38.44

4.3.1.2. $Li_2Mn_{1-x}Co_xO_3$

Presented in Figure 4.2 , the ground state diagram of the $Li_2Mn_{1-x}Co_xO_3$ system shows all 65 generated miscible constituents at T=0 K, that is, all phases are in the negative heats of formation. Table 4.2 shows all 8 structures along the ground state line and their formation energies. The most thermodynamically stable structure was found to be monoclinic $Li_2Mn_{0.5}Co_{0.5}O_3$ with space group C2/c.

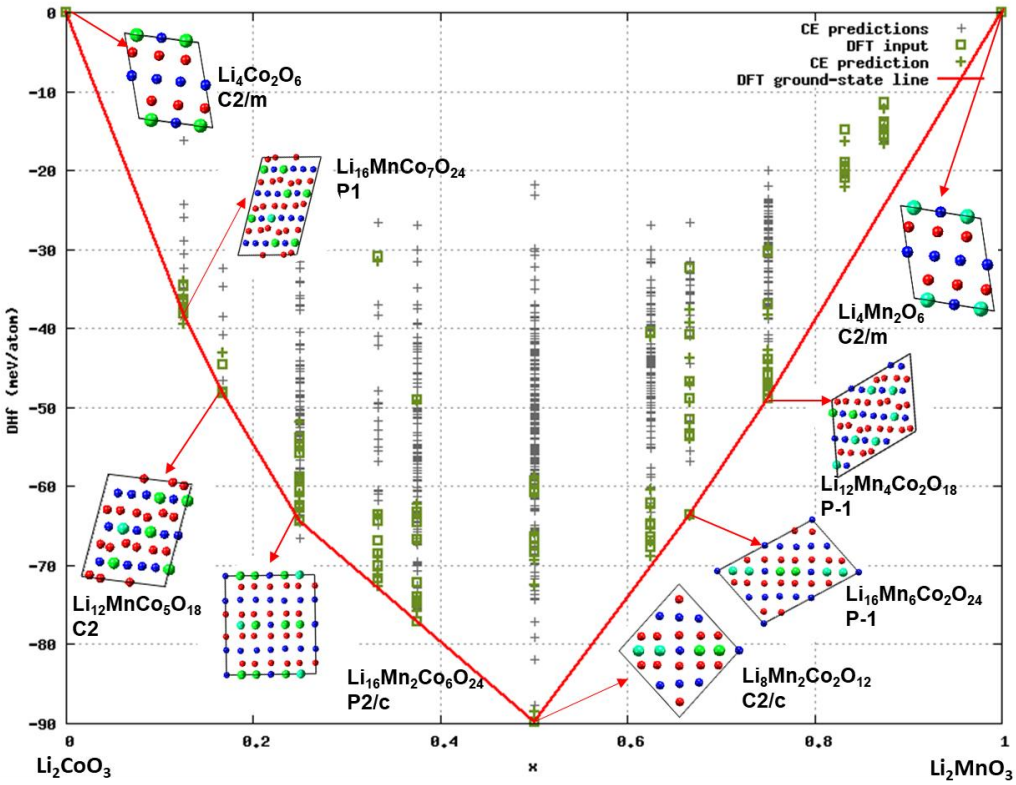

Figure 4.2: The ground state line of the $Li_2Mn_{1-x}Co_xO_3$ system: the heat of formation versus Co concentration and ground state structures.

Table 4.2: Stable structures of $Li_2Mn_{1-x}Co_xO_3$ along the ground state line

Structural formula	**Space group**	**Formation energy (eV/atom)**
Li_2CoO_3	C2/m	-32.91
$Li_2Mn_{0.125}Co_{0.875}O_3$	C2	-33.58
$Li_2Mn_{0.17}Co_{0.83}O_3$	C2	-35.60
$Li_2Mn_{0.25}Co_{0.75}O_3$	C2/c	-35.91
$Li_2Mn_{0.5}Co_{0.5}O_3$	C2/c	-36.80
$Li_2Mn_{0.67}Co_{0.33}O_3$	P-1	-37.35
$Li_2Mn_{0.75}Co_{0.25}O_3$	C2/c	-37.62
Li_2MnO_3	C2/m	-38.44

4.3.1.3. $Li_2Mn_{1-x}Cr_xO_3$

Figure 4.3 presents a binary ground state diagram of the $Li_2Mn_{1-x}Cr_xO_3$ system. The diagram shows all the 90 generated phases of which 10 are on the ground state diagram. The diagram further illustrates that the system becomes a miscibility gap towards X= 0.8. Table 4.3 list all the phases along the ground state line and their formation energies. The most thermodynamically stable phase is the triclinic $Li_2Mn_{0.5}Cr_{0.5}O_3$ with space group P-1.

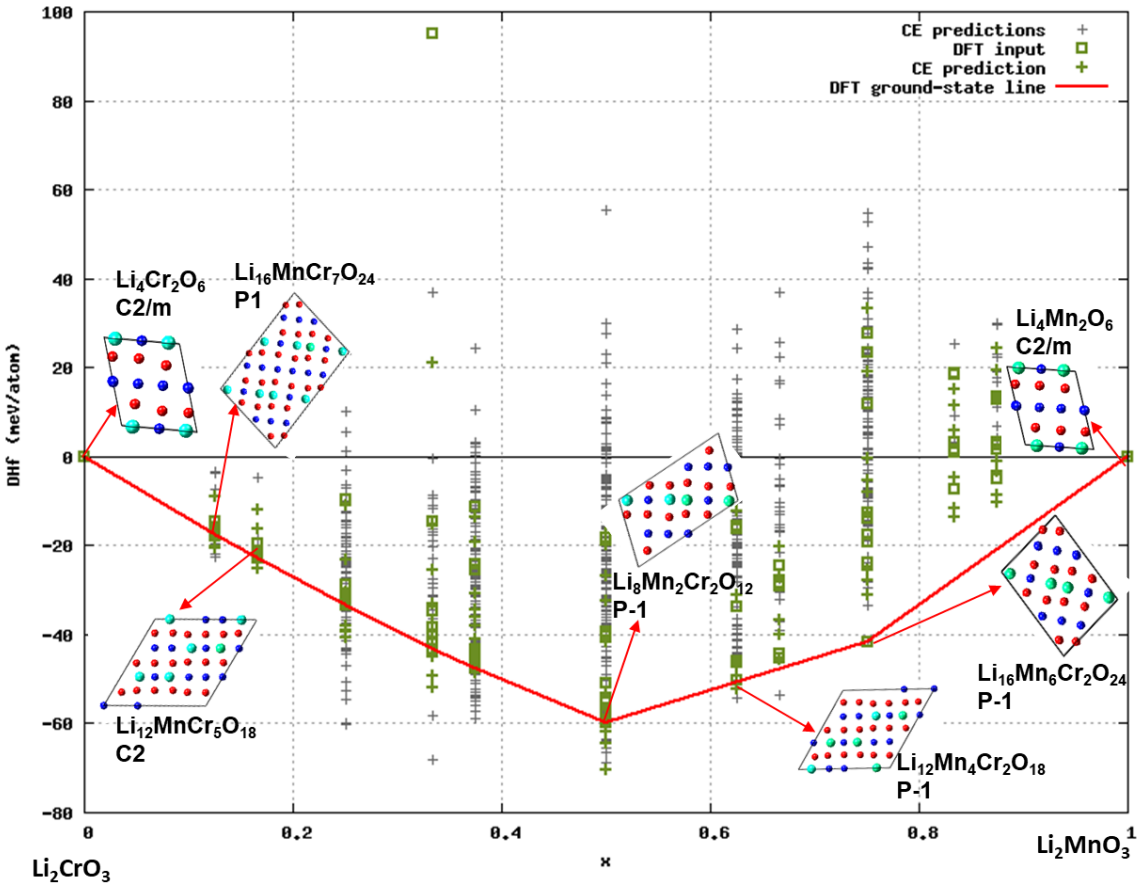

Figure 4.3: The ground state line of the $Li_2Mn_{1-x}Cr_xO_3$ system: the heat of formation versus Cr concentration and ground state structures.

Table 4.3: Stable structures of $Li_2Mn_{1-x}Cr_xO_3$ along the ground state line

Structural formula	Space group	Formation energy (eV/atom)
Li_2CrO_3	C2/m	-40.03
$Li_2Mn_{0.75}Cr_{0.25}O_3$	P-1	-38.87
$Li_2Mn_{0.67}Cr_{0.33}O_3$	P-1	-39.03
$Li_2Mn_{0.5}Cr_{0.5}O_3$	P-1	-39.29
$Li_2Mn_{0.375}Cr_{0.625}O_3$	P1	-39.48
$Li_2Mn_{0.33}Cr_{0.67}O_3$	P-1	-39.55
$Li_2Mn_{0.25}Cr_{0.75}O_3$	P-1	-39.66
$Li_2Mn_{0.17}Cr_{0.83}O_3$	C2	-39.78
$Li_2Mn_{0.125}Cr_{0.875}O_3$	P1	-39.84
Li_2MnO_3	C2/m	-38.44

4.3.1.4. $Li_2Mn_{1-x}Ru_xO_3$

The binary ground state diagram of $Li_2Mn_{1-x}Ru_xO_3$ in Figure 4.4 produced 83 new structures from which only 4 structures are on the DFT ground-state line. Table 3.1 lists the most stable structures, their space groups and their formation energies. The most stable phase was found to be triclinic $Li_2Mn_{0.5}Ru_{0.5}O_3$ with space group P-1.

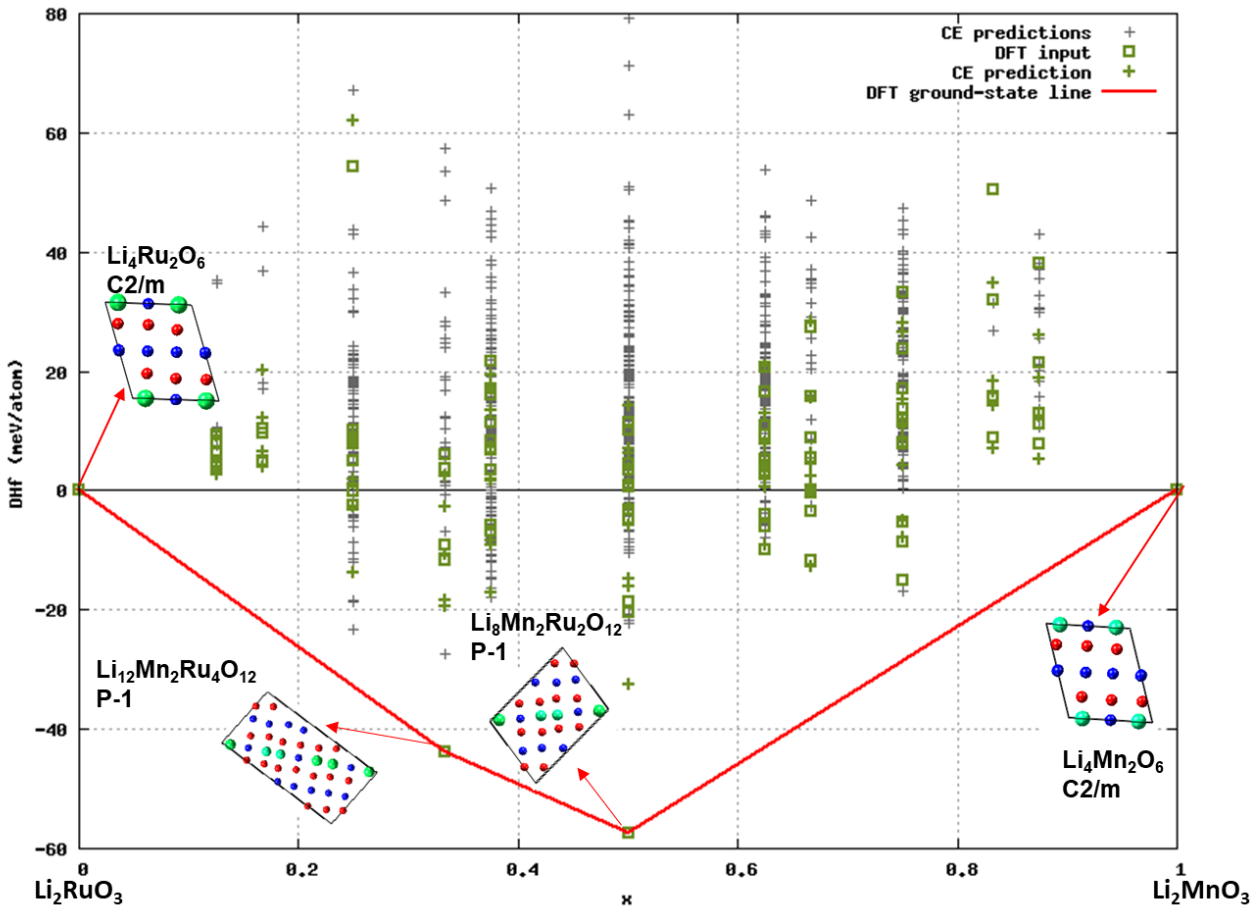

Figure 4.4: The ground state line of the $Li_2Mn_{1-x}Ru_xO_3$ system: the heat of formation versus Ru concentration and ground state structures.

Table 4.4: Stable structures of $Li_2Mn_{1-x}Ru_xO_3$ along the ground state line

Structural formula	**Space group**	**Formation energy (eV/atom)**
Li_2RuO_3	C2/m	-37.22
$Li_2Mn_{0.33}Ru_{0.67}O_3$	P-1	-37.64
$Li_2Mn_{0.5}Ru_{0.5}O_3$	P-1	-37.86
Li_2MnO_3	C2/m	-38.44

4.3.2. Monte Carlo Simulations

The canonical ensemble was chosen for the Monte Carlo (MC) simulation of the $Li_2Mn_{1-x}M_xO_3$ systems. All the systems used periodic cells with 12000 atoms. The temperature was varied from 0 K- 3500 K for all the systems. Temperature profiles for $Li_2Mn_{1-x}Ni_xO_3$, $Li_2Mn_{1-x}Co_xO_3$, $Li_2Mn_{1-x}Cr_xO_3$ and $Li_2Mn_{1-x}Ru_xO_3$ showing phase changes across different concentrations are shown below. From these interactive temperatures vs energy graphs, one can extract critical temperatures (when an increase in temperature results in the same energy difference in the system). Below the critical temperature, the dissolved TM form precipitates indicating the solubility limits of Li_2MnO_3. The pink spheres represent transition metal dopant and the green represent Mn.

4.3.2.1. $Li_2Mn_{1-x}Ni_xO_3$

Figure 4.5 shows the variations in energies per atom and the corresponding degree of inversion of a) $Li_2Mn_{0.1}Ni_{0.9}O_3$, b) $Li_2Mn_{0.2}Ni_{0.8}O_3$ and c) $Li_2Mn_{0.3}Ni_{0.7}O_3$ structures at a range of temperatures from 0 K to 3500 K computed using Monte Carlo simulation. Snapshots of the structures generated at various temperatures are also shown. The energy difference increases continuously with increasing temperature but there is a sudden reduction in the rate of increase at around the critical temperature, which appears to correspond with the onset of reverse inversion.

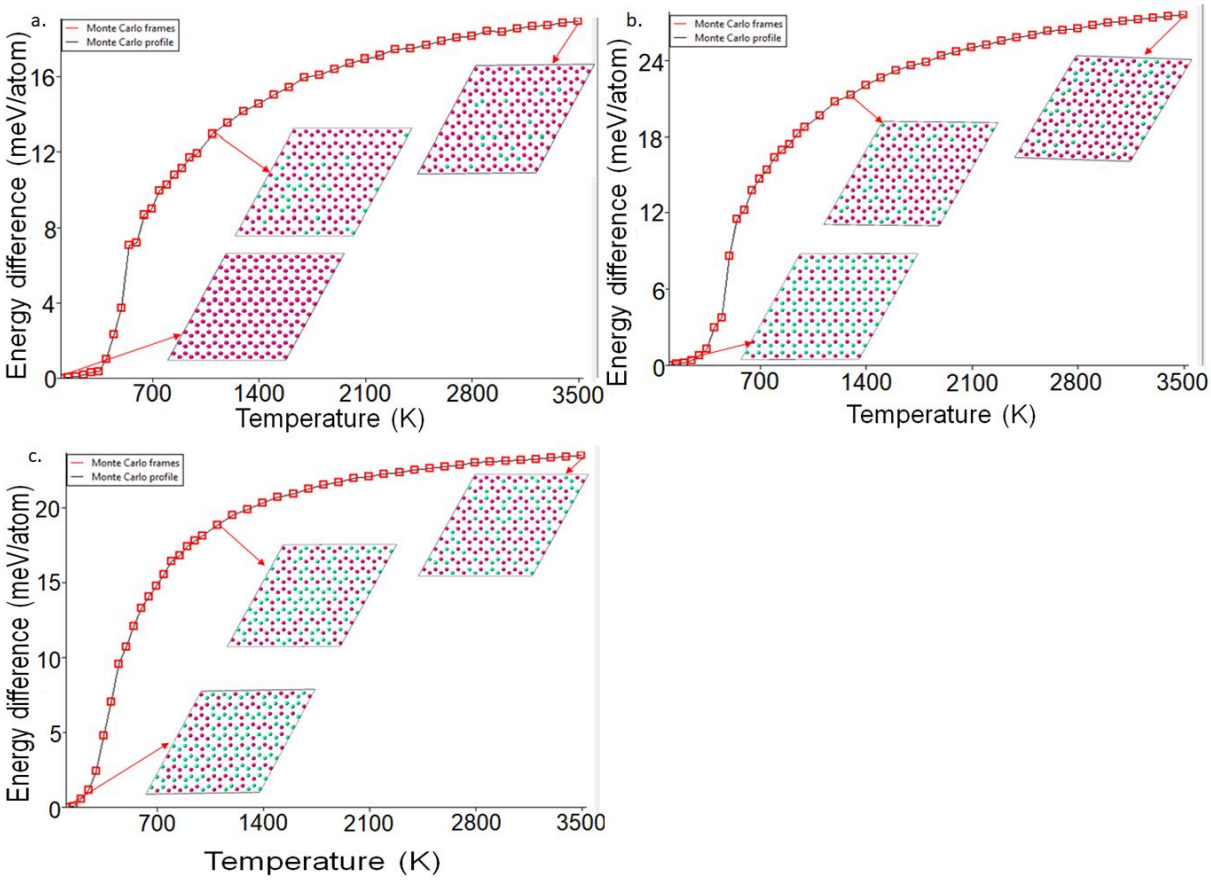

Figure 4.5: Temperatures profiles cross sections through the 10 × 10 × 10 Monte Carlo simulation cells of a) $Li_2Mn_{0.1}Ni_{0.9}O_3$ b) $Li_2Mn_{0.2}Ni_{0.8}O_3$ and c) $Li_2Mn_{0.3}Ni_{0.7}O_3$

Figure 4.6 depicts the changes in energies per atom and the corresponding degrees of inversion for a) $Li_2Mn_{0.4}Ni_{0.6}O_3$, b) $Li_2Mn_{0.5}Ni_{0.5}O_3$ and c) $Li_2Mn_{0.6}Ni_{0.4}O_3$ structures calculated using Monte Carlo simulation at temperatures ranging from 0 K to 3500 K. Also shown are snapshots of the structures generated at various temperatures. The energy difference increases continuously as temperature increases, but there is a sudden decrease in the rate of increase before the systems reach equilibrium.

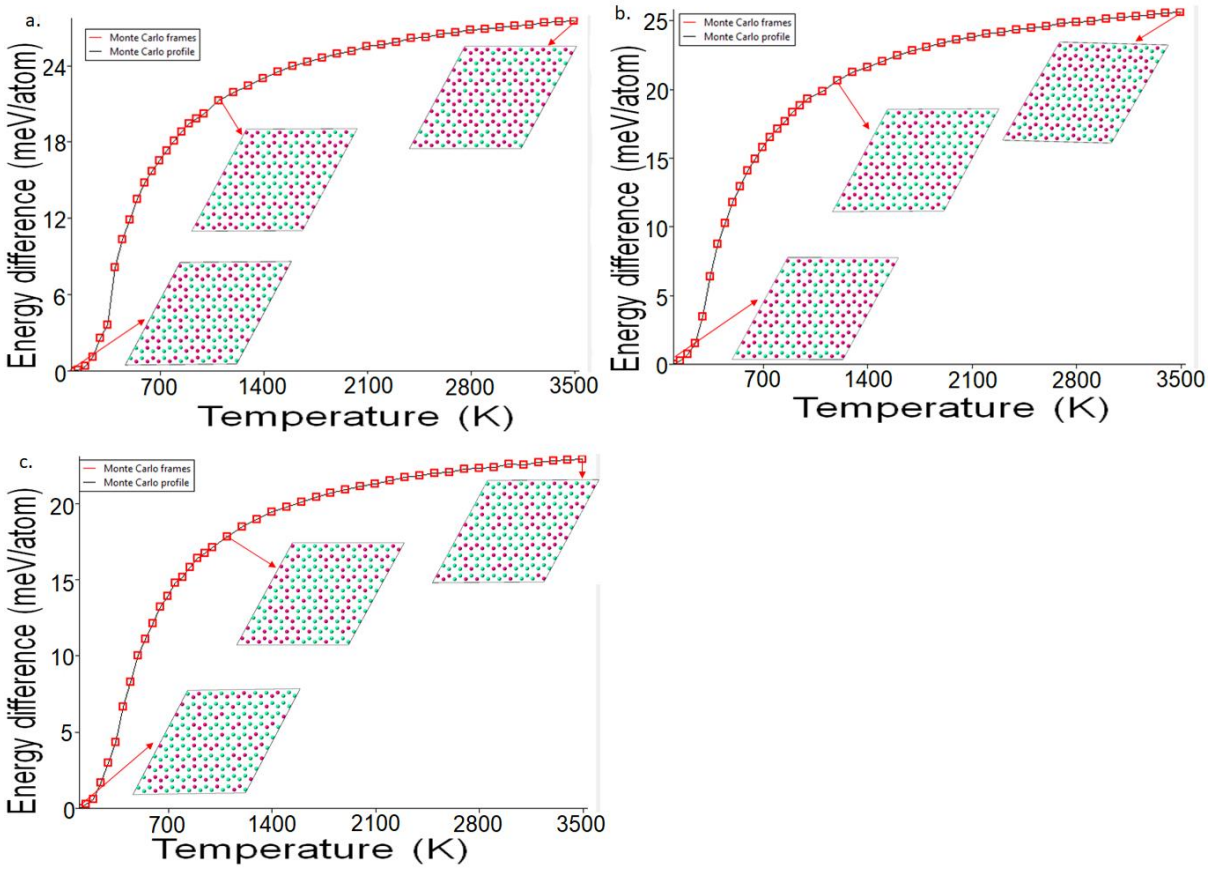

Figure 4.6: Temperatures profiles cross sections through the 10 × 10 × 10 Monte Carlo simulation cells of a) $Li_2Mn_{0.4}Ni_{0.6}O_3$, b) $Li_2Mn_{0.5}Ni_{0.5}O_3$ and c) $Li_2Mn_{0.6}Ni_{0.4}O_3$

Figure 4.7 shows the changes in energies per atom and the corresponding degrees of inversion of a) $Li_2Mn_{0.7}Ni_{0.3}O_3$, b) $Li_2Mn_{0.8}Ni_{0.2}O_3$ and c) $Li_2Mn_{0.9}Ni_{0.1}O_3$ structures calculated using Monte Carlo simulation over a temperature range of 0 K to 3500 K. A snapshot of the structures created at different temperatures is also shown. The energy difference increases continuously as the temperature is increased; however, the increase drops off sharply near the critical temperature. At this temperature, the system begins to reach equilibrium.

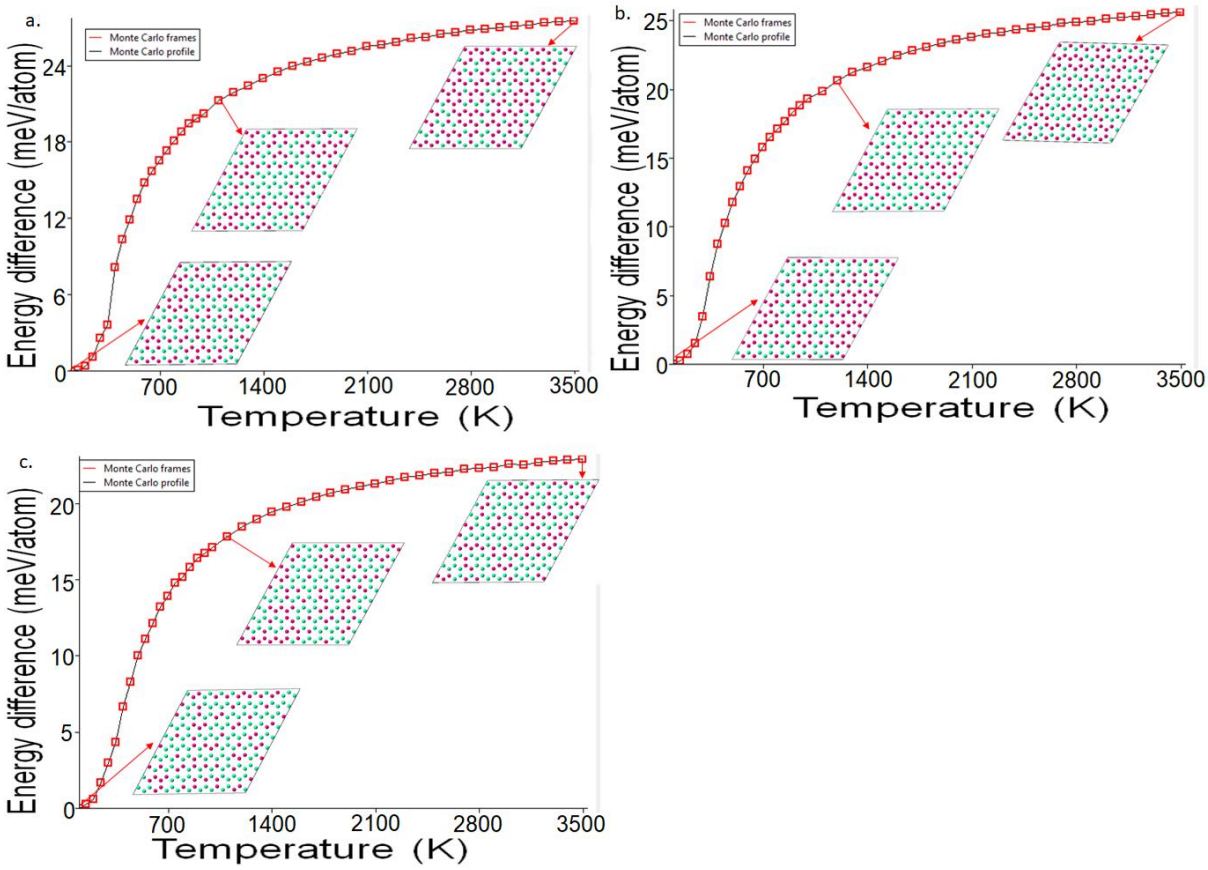

Figure 4.7: Temperatures profiles cross sections through the 10 × 10 × 10 Monte Carlo simulation cells of a) $Li_2Mn_{0.7}Ni_{0.3}O_3$ b) $Li_2Mn_{0.8}Ni_{0.2}O_3$ and c) $Li_2Mn_{0.9}Ni_{0.1}O_3$

4.3.2.2. $Li_2Mn_{1-x}Co_xO_3$

Figure 4.8 depicts the changes in energies per atom and the corresponding degrees of inversion of a) $Li_2Mn_{0.1}Co_{0.9}O_3$, b) $Li_2Mn_{0.2}Co_{0.8}O_3$ and c) $Li_2Mn_{0.3}Co_{0.7}O_3$ structures calculated using Monte Carlo simulation at temperatures ranging from 0 K to 3500 K. A snapshot of the structures generated at various temperatures is also shown. The energy difference increases continuously with increasing temperature, but there is a sudden decrease in the rate of increase around the critical temperature, which corresponds with the beginning of reverse inversion.

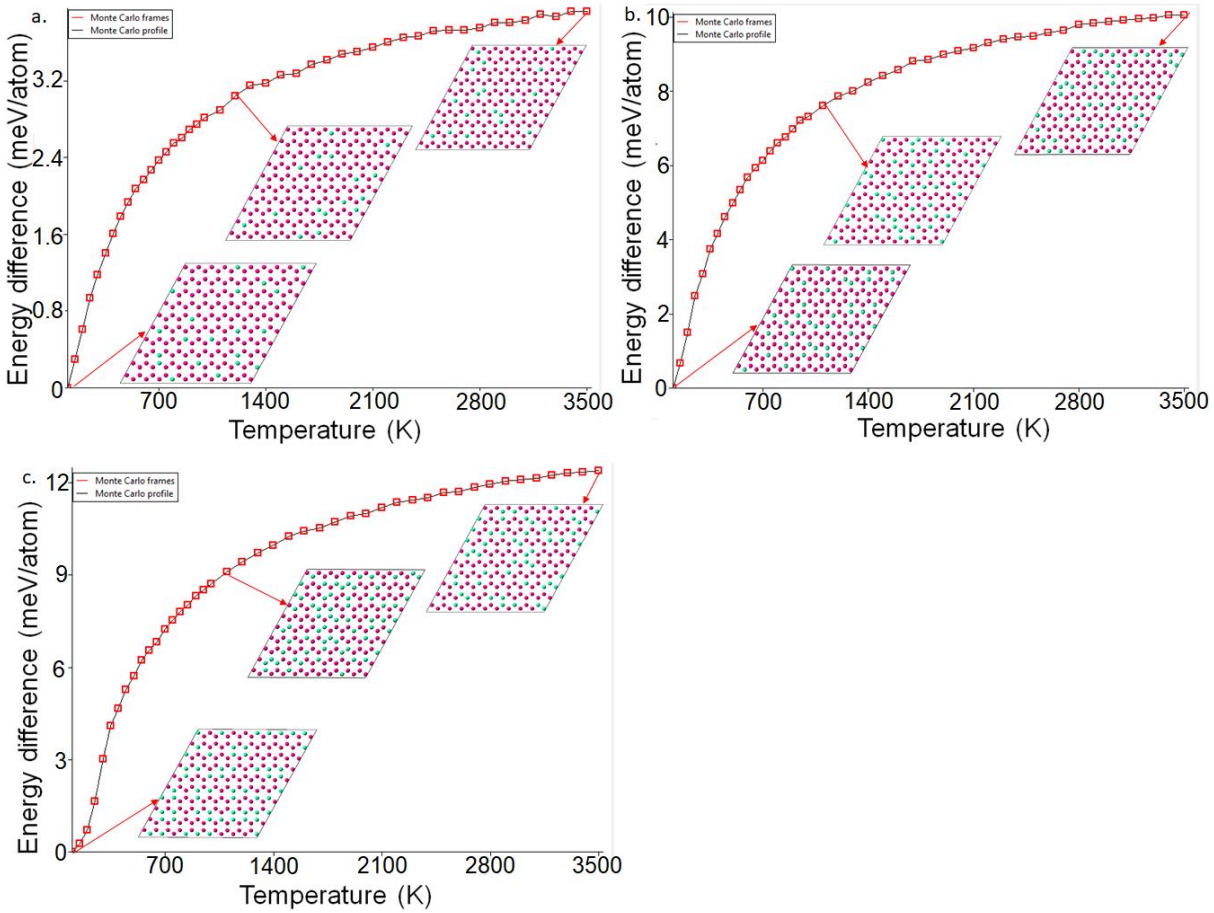

Figure 4.8: Temperatures profiles cross sections through the 10 × 10 × 10 Monte Carlo simulation cells of a) $Li_2Mn_{0.1}Co_{0.9}O_3$ 1, b) $Li_2Mn_{0.2}Co_{0.8}O_3$ and c) $Li_2Mn_{0.3}Co_{0.7}O_3$

Figure 4.9 depicts the changes in energies per atom and the corresponding degrees of inversion of *a) $Li_2Mn_{0.4}Co_{0.6}O_3$, b) $Li_2Mn_{0.5}Co_{0.5}O_3$ and c) $Li_2Mn_{0.6}Co_{0.4}O_3$* structures calculated using Monte Carlo simulation at temperatures ranging from 0 K to 3500 K. A snapshot of the structures generated at various temperatures is also shown. The energy difference increases continuously with increasing temperature, but there is a sudden decrease in the rate of increase around the critical temperature, which corresponds with the start of reverse inversion.

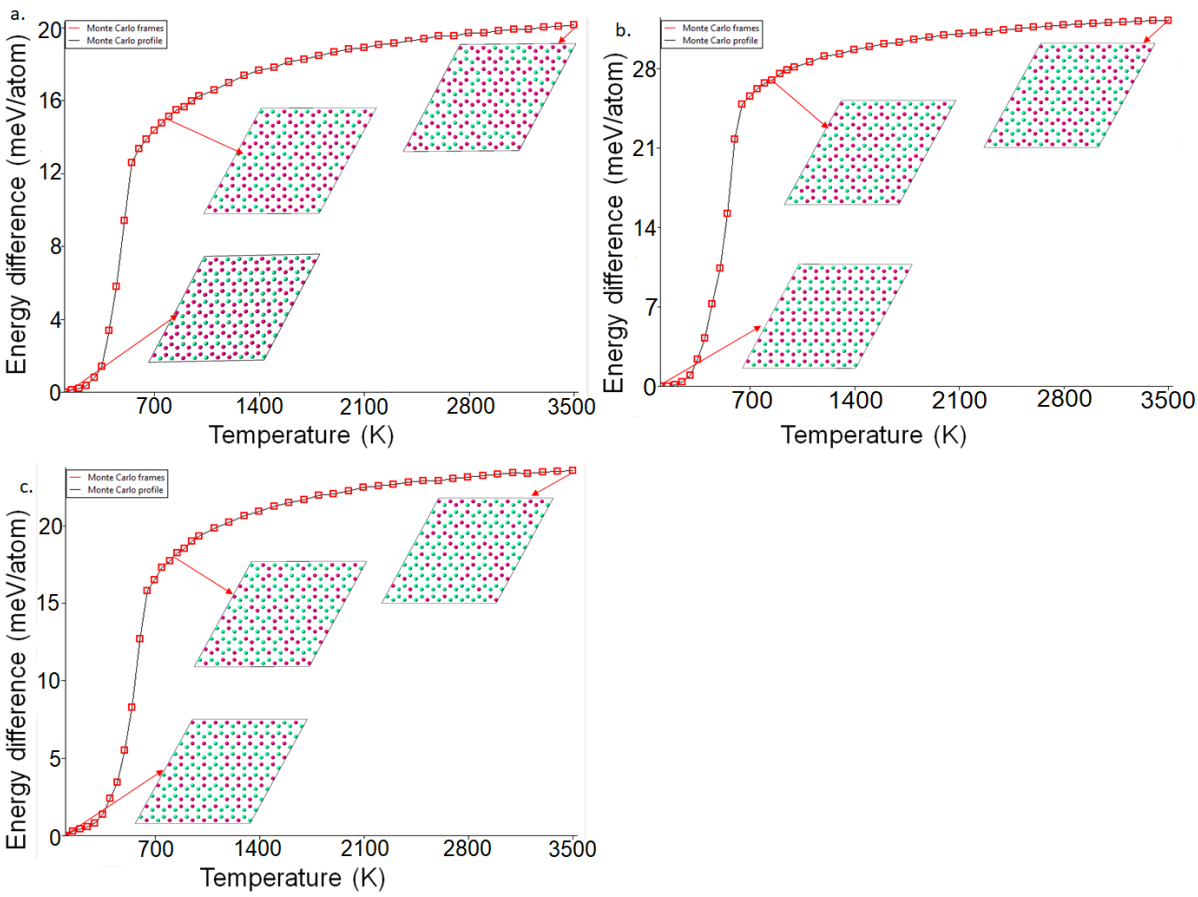

Figure 4.9: Temperatures profiles cross sections through the 10 × 10 × 10 Monte Carlo simulation cells of a) $Li_2Mn_{0.4}Co_{0.6}O_3$ b) $Li_2Mn_{0.5}Co_{0.5}O_3$ and c) $Li_2Mn_{0.6}Co_{0.4}O_3$

Figure 4.10 depicts the changes in energies per atom and the corresponding degrees of inversion of *a)* $Li_2Mn_{0.7}Co_{0.3}O_3$, b) $Li_2Mn_{0.8}Co_{0.2}O_3$ *c)* $Li_2Mn_{0.9}Co_{0.1}O_3$ structures calculated using Monte Carlo simulation at temperatures ranging from 0 K to 3500 K. A snapshot of the structures generated at various temperatures is also shown. The energy difference increases continuously with increasing temperature, but there is a sudden decrease in the rate of increase around the critical temperature, which corresponds with the onset of reverse inversion.

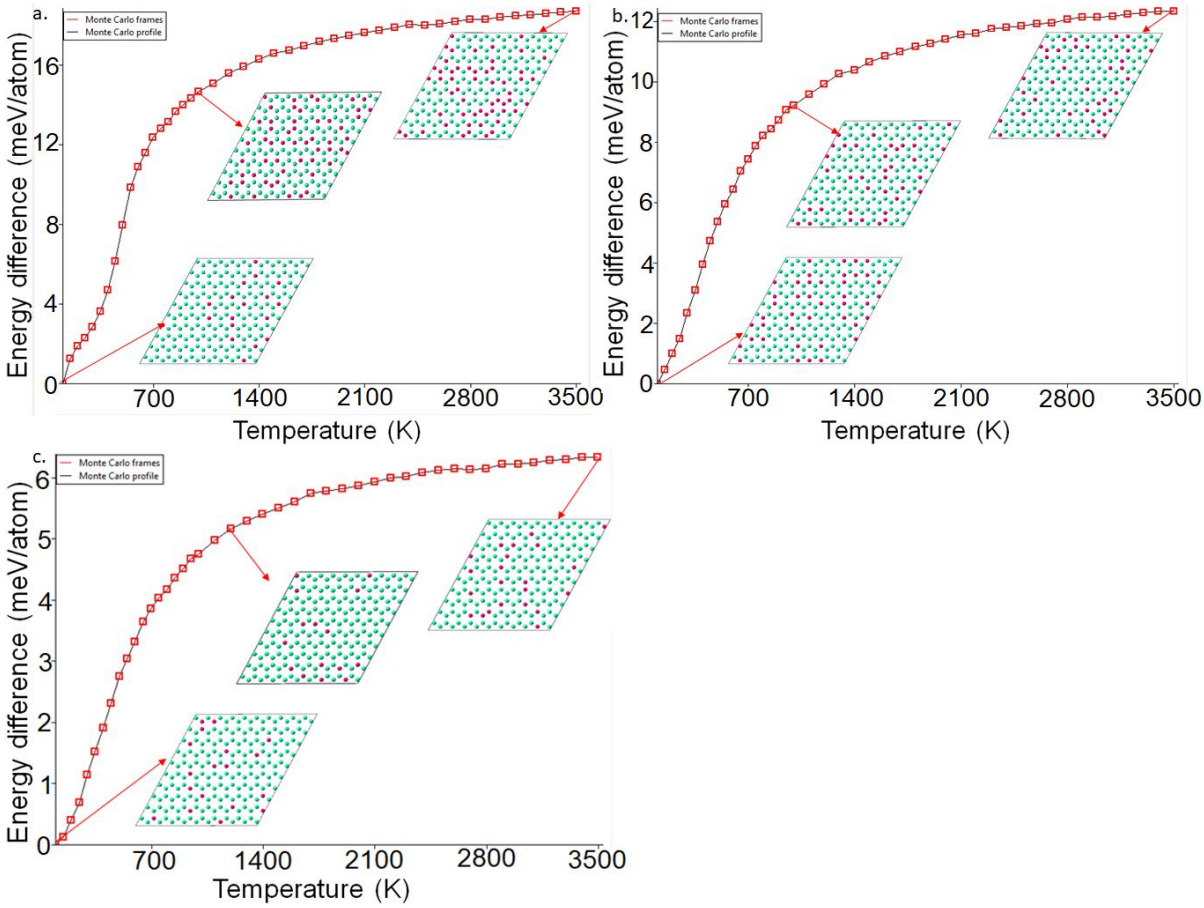

Figure 4.10:Temperatures profiles cross sections through the 10 × 10 × 10 Monte Carlo simulation cells of a) $Li_2Mn_{0.7}Co_{0.3}O_3$ b) $Li_2Mn_{0.8}Co_{0.2}O_3$ *c)* $Li_2Mn_{0.9}Co_{0.1}O_3$

4.3.2.3. $Li_2Mn_{1-x}Cr_xO_3$

Figure 4.11 depicts the changes in energies per atom and the corresponding degrees of inversion of a) $Li_2Mn_{0.1}Cr_{0.9}O_3$, b) $Li_2Mn_{0.2}Cr_{0.8}O_3$ and c) $Li_2Mn_{0.3}Cr_{0.7}O_3$ structures calculated using Monte Carlo simulation at temperatures ranging from 0 K to 3500 K. A snapshot of the structures generated at various temperatures is also shown. The energy difference increases continuously with increasing temperature, but there is a sudden decrease in the rate of increase around the critical temperature, which corresponds with the onset of reverse inversion.

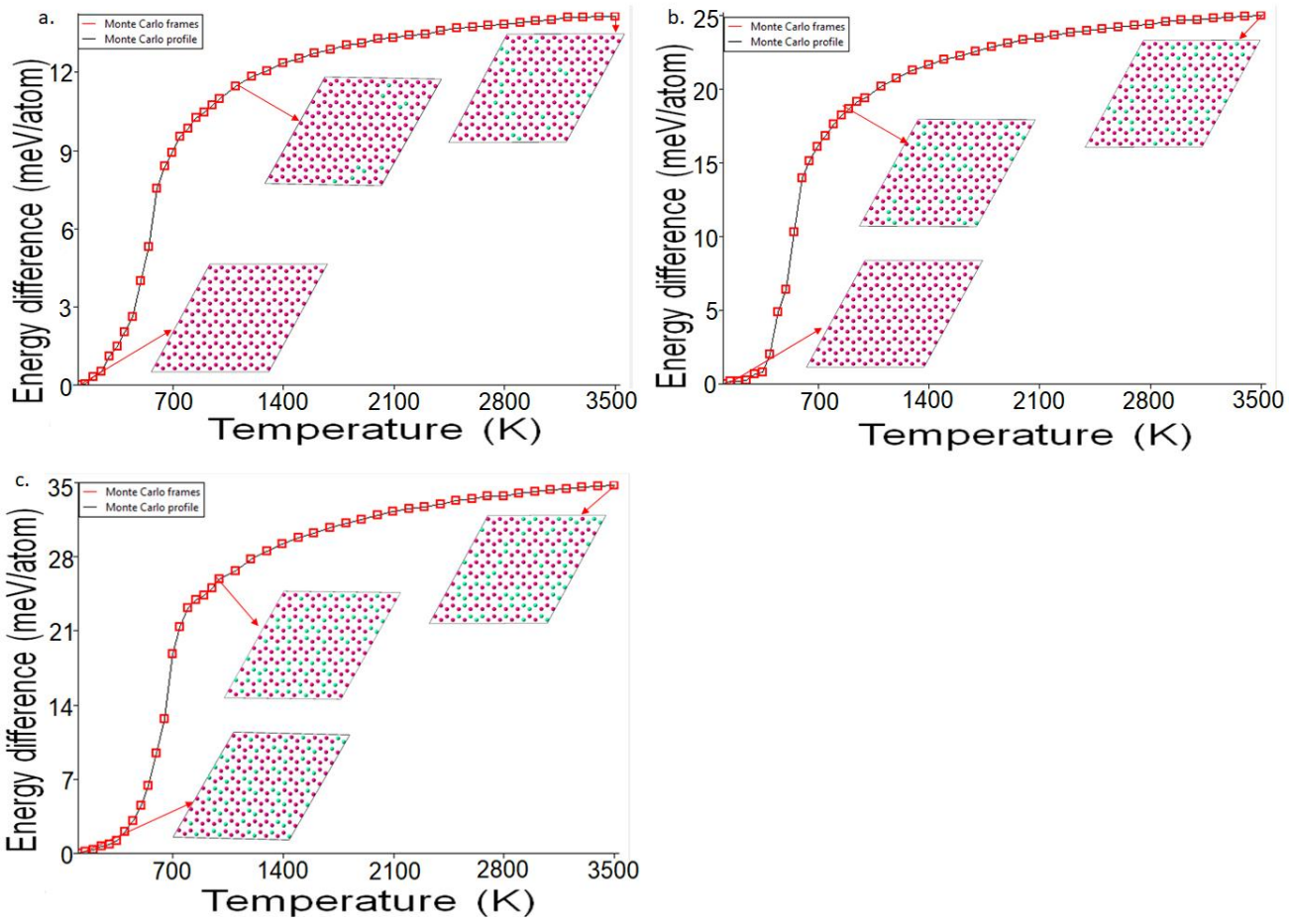

Figure 4.11: Temperatures profiles cross sections through the 10 × 10 × 10 Monte Carlo simulation cells of a) $Li_2Mn_{0.1}Cr_{0.9}O_3$ b) $Li_2Mn_{0.2}Cr_{0.8}O_3$ and c) $Li_2Mn_{0.3}Cr_{0.7}O_3$

Figure 4.12 depicts the changes in energies per atom and the corresponding degrees of inversion of a) $Li_2Mn_{0.4}Cr_{0.6}O_3$, b) $Li_2Mn_{0.5}Cr_{0.5}O_3$ and c) $Li_2Mn_{0.6}Cr_{0.4}O_3$ structures calculated using Monte Carlo simulation at temperatures ranging from 0 K to 3500 K. A snapshot of the structures generated at various temperatures is also shown. The energy difference increases continuously with increasing temperature, but there is a sudden decrease in the rate of increase around the critical temperature, which corresponds with the onset of reverse inversion.

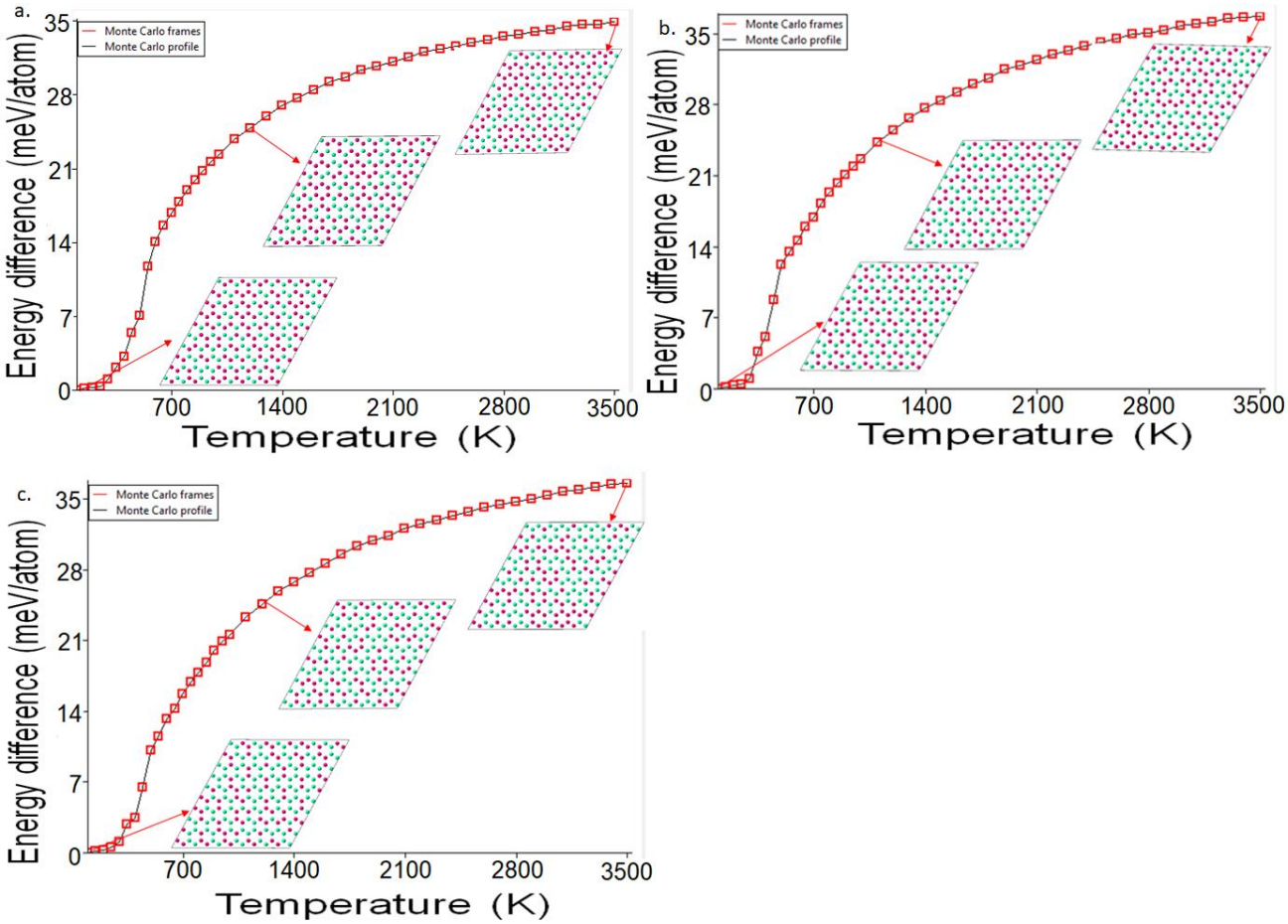

Figure 4.12: Temperatures profiles cross sections through the 10 × 10 × 10 Monte Carlo simulation cells of a) $Li_2Mn_{0.4}Cr_{0.6}O_3$ b) $Li_2Mn_{0.5}Cr_{0.5}O_3$ and c) $Li_2Mn_{0.6}Cr_{0.4}O_3$

Figure 4.13 depicts the changes in energies per atom and the corresponding degrees of inversion of a) $Li_2Mn_{0.7}Cr_{0.3}O_3$, b) $Li_2Mn_{0.8}Cr_{0.1}O_3$ and c) $Li_2Mn_{0.9}Cr_{0.1}O_3$ structures calculated using Monte Carlo simulation at temperatures ranging from 0 K to 3500 K. A snapshot of the structures generated at various temperatures is also shown. The energy difference increases continuously with increasing temperature, but there is a sudden decrease in the rate of increase around the critical temperature, which corresponds with the onset of reverse inversion.

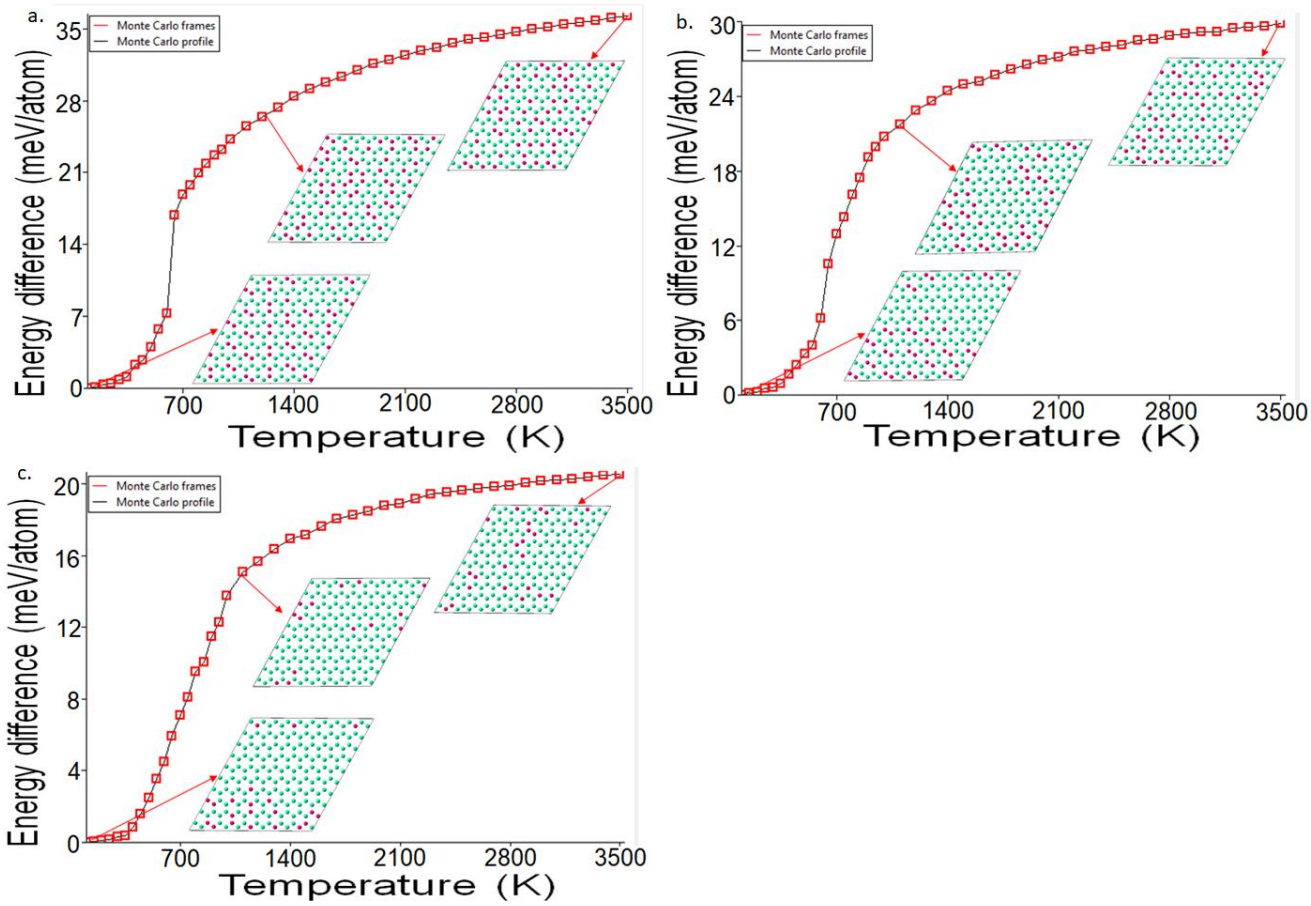

Figure 4.13: Temperatures profiles cross sections through the 10 × 10 × 10 Monte Carlo simulation cells of a) $Li_2Mn_{0.7}Cr_{0.3}O_3$ c) $Li_2Mn_{0.8}Cr_{0.1}O_3$ and c) $Li_2Mn_{0.9}Cr_{0.1}O_3$

4.3.2.4. $Li_2Mn_{1-x}Ru_xO_3$

Figure 4.14 depicts the changes in energies per atom and the corresponding degrees of inversion of a) $Li_2Mn_{0.1}Ru_{0.9}O_3$, b) $Li_2Mn_{0.2}Ru_{0.8}O_3$ and c) $Li_2Mn_{0.3}Ru_{0.7}O_3$ structures calculated using Monte Carlo simulation. A snapshot of the structures created at different temperatures is also shown. The energy difference increases continuously as temperature rises, but there is a sharp decrease in the rate of increase near the critical temperature, which corresponds with the onset of reverse inversion.

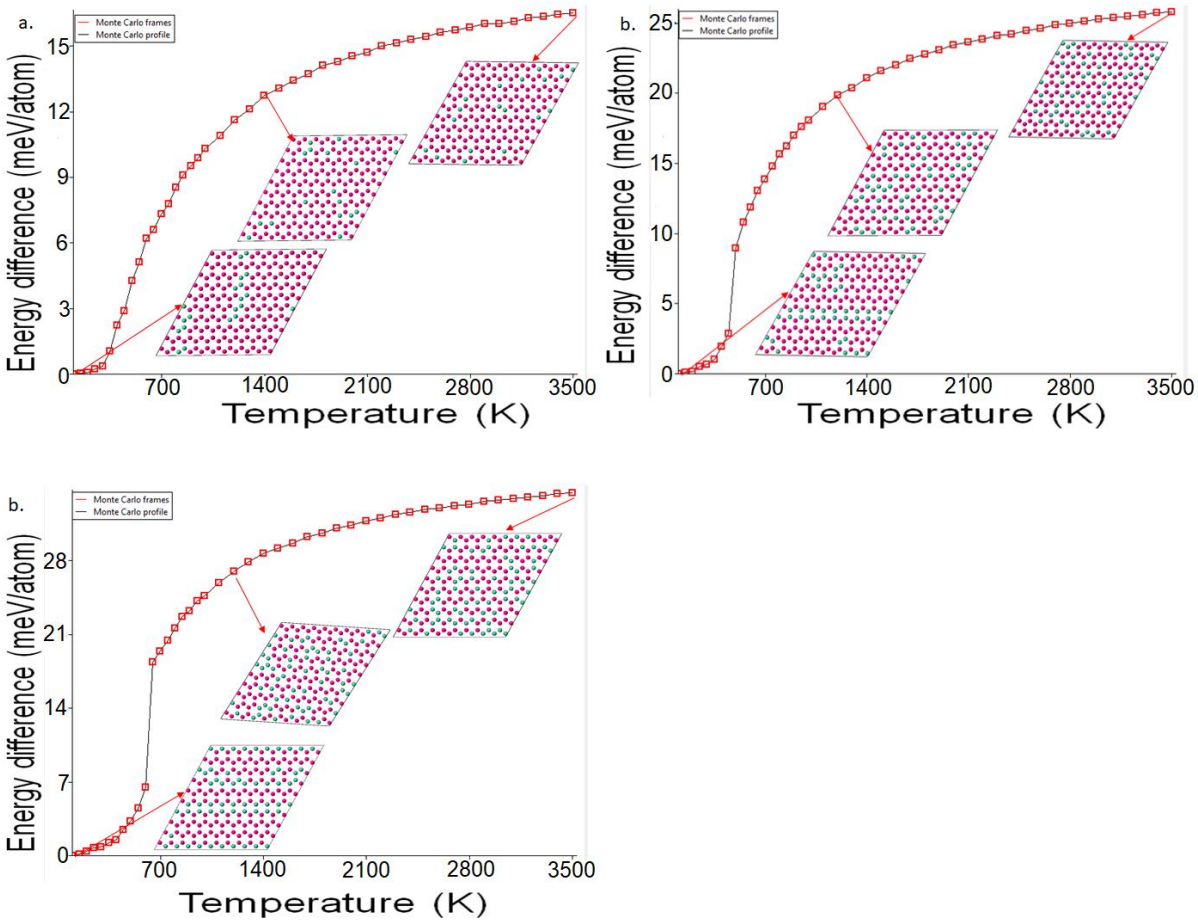

Figure 4.14: Temperatures profiles cross sections through the 10 × 10 × 10 Monte Carlo simulation cells of a) $Li_2Mn_{0.1}Ru_{0.9}O_3$ b) $Li_2Mn_{0.2}Ru_{0.8}O_3$ and c) $Li_2Mn_{0.3}Ru_{0.7}O_3$

Figure 4.15 depicts the changes in energies per atom and the corresponding degrees of inversion of a) $Li_2Mn_{0.4}Ru_{0.6}O_3$, b) $Li_2Mn_{0.5}Ru_{0.5}O_3$ and c) $Li_2Mn_{0.6}Ru_{0.4}O_3$ structures calculated using Monte Carlo simulation at temperatures ranging from 0 K to 3500 K. A snapshot of the structures generated at various temperatures is also shown. The energy difference increases continuously with increasing temperature, but there is a sudden decrease in the rate of increase around the critical temperature, which corresponds with the onset of reverse inversion.

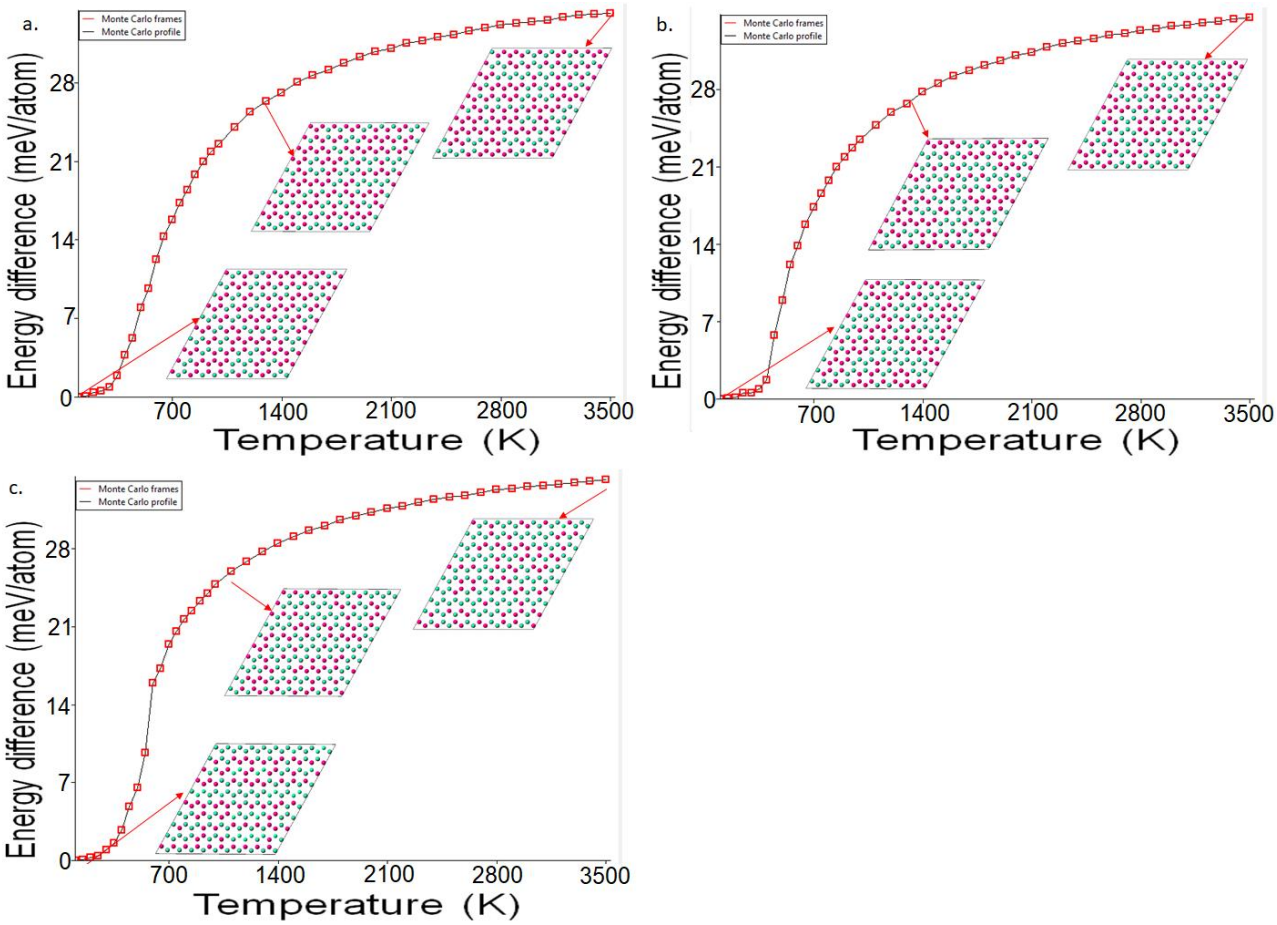

Figure 4.15: Temperatures profiles cross sections through the 10 × 10 × 10 Monte Carlo simulation cells of a) $Li_2Mn_{0.4}Ru_{0.6}O_3$ b) $Li_2Mn_{0.5}Ru_{0.5}O_3$ and c) $Li_2Mn_{0.6}Ru_{0.4}O_3$

Figure 4.16 depicts the changes in energies per atom and the corresponding degrees of inversion of *a)* $Li_2Mn_{0.7}Ru_{0.3}O_3$, *b)* $Li_2Mn_{0.8}Ru_{0.2}\ O_3$ *and c)* $Li_2Mn_{0.9}\ Ru_{0.1}O_3$ structures calculated using Monte Carlo simulation at temperatures ranging from 0 K to 3500 K. A snapshot of the structures generated at various temperatures are also shown. The energy difference increases continuously with increasing temperature, but there is a sudden decrease in the rate of increase around the critical temperature, which corresponds with the onset of reverse inversion.

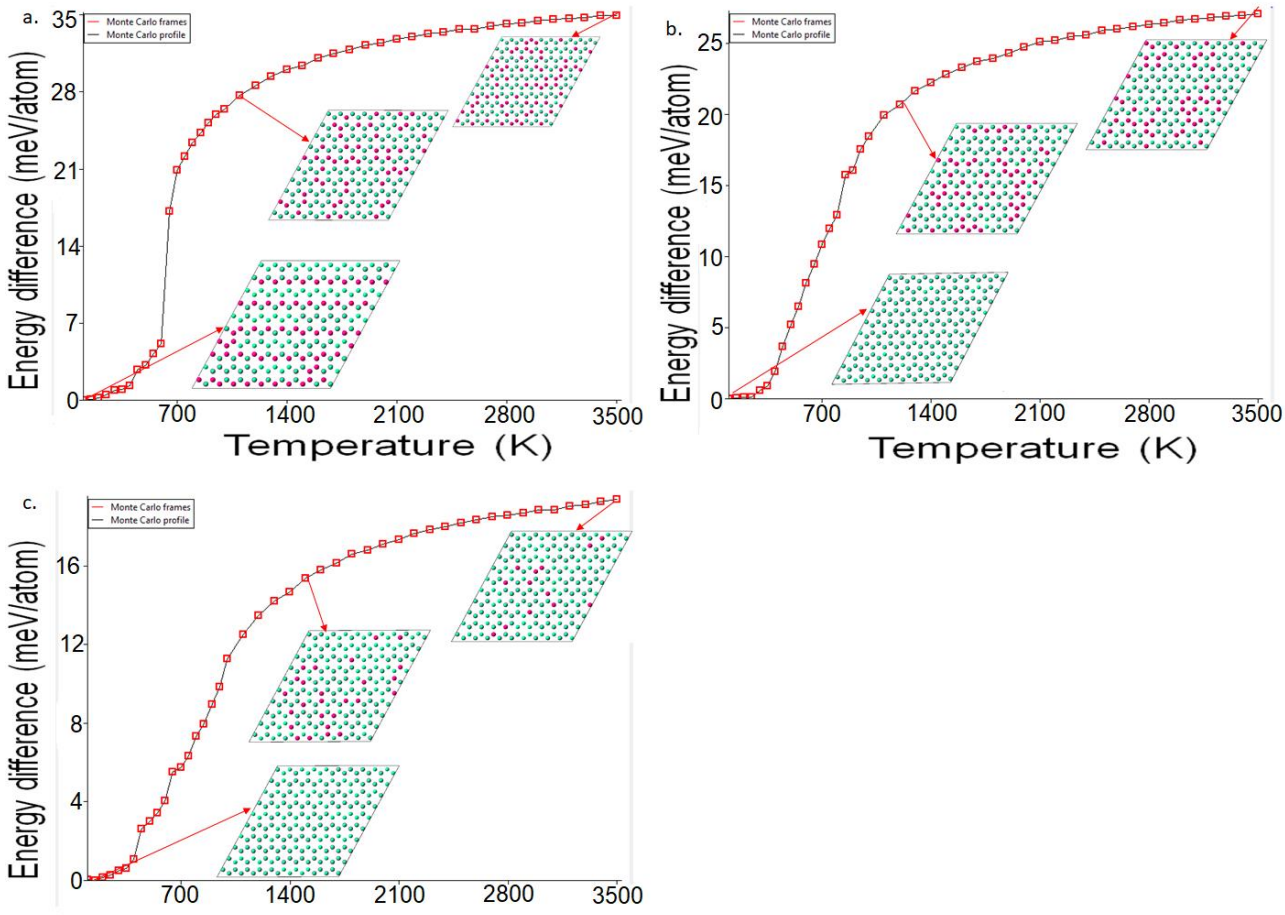

Figure 4.16: Temperatures profiles cross sections through the 10 × 10 × 10 Monte Carlo simulation cells of a) $Li_2Mn_{0.7}Ru_{0.3}O_3$, b) $Li_2Mn_{0.8}Ru_{0.2}O_3$ and c) $Li_2Mn_{0.9}Ru_{0.1}O_3$

4.3.3. Constructed Phase Diagrams

Below we show tables of concentrations of manganese and M=Ni, Co, Cr, Ru with critical temperatures generated from MC interactive temperature versus energy graphs above. Critical temperatures are then used to construct phase diagrams in figures 4.17-4.20. Phase diagrams can be used to predict the phase changes that occurred in a material after it was subjected to a specific heat treatment process. This is significant because the properties of a material's components are determined by the phases that exist in the material.

4.3.3.1. $Li_2Mn_{1-x}Ni_xO_3$

Figure 4.17 illustrates a phase diagram of the $Li_2Mn_{1-x}Ni_xO_3$ system. The diagram shows two cooling curves. The phase separation decreases as the system is cooled and at around 850 K the system mixes.

Table 4.5:Concentration of Manganese Nickel with respect to critical temperatures for a mixed system $Li_2Mn_{1-x}Ni_xO_3$.

Concentration (Ni)	**Critical Temperature (K)**
0.1	1200
0.2	1100
0.3	1000
0.4	950
0.5	850
0.6	900
0.7	950
0.8	1000
0.9	1200

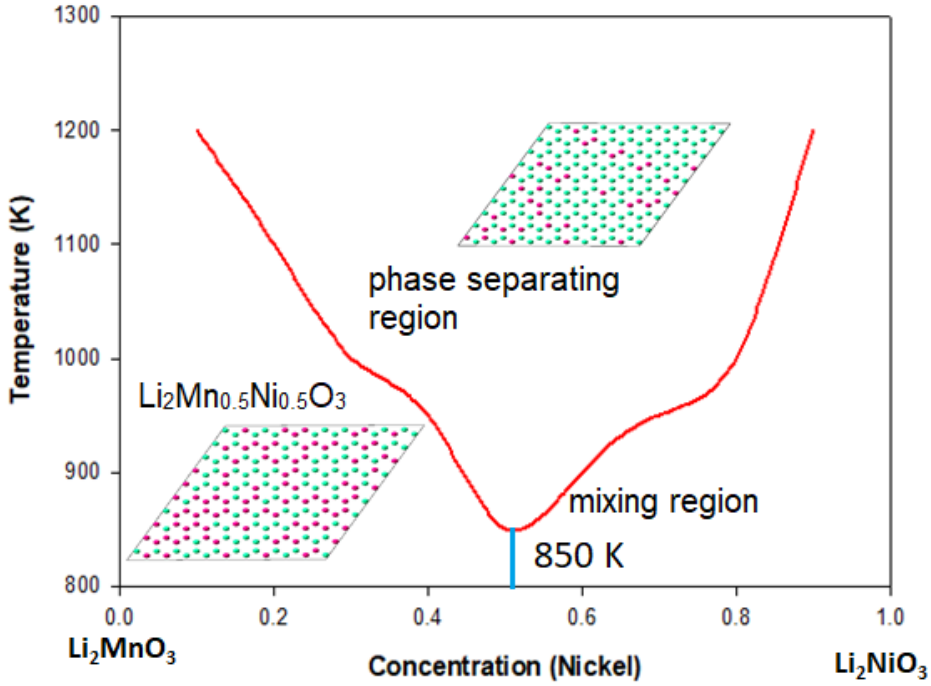

Figure 4.17: Constructed phase diagram of $Li_2Mn_{1-x}Ni_xO_3$ using critical temperatures at different concentrations.

4.3.3.2. $Li_2Mn_{1-x}Co_xO_3$

Figure 4.18 shows a calculated phase diagram which appears to be symmetrical. Inside the curve, the system is phase separating and the mixture of two phases of Li_2MnO_3 and Li_2CoO_3 is stable. Outside the curve, single-phase homogenous $Li_2Mn_{1-x}Co_xO_3$ is stable. The mixing temperature is 700 K.

Table 4.6:Concentration of Manganese Cobalt with respect to critical temperatures for a mixed system $Li_2Mn_{1-x}Co_xO_3$

Concentration (Co)	Critical Temperature (K)
0.1	1300
0.2	1200
0.3	1100
0.4	800
0.5	700
0.6	750
0.7	1000
0.8	1100
0.9	1200

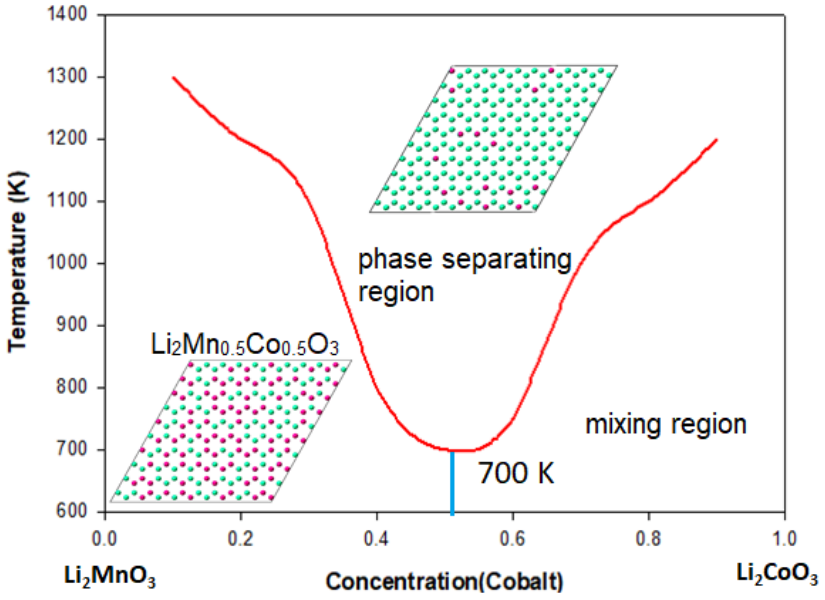

Figure 4.18: Constructed phase diagram of $Li_2Mn_{1-x}Co_xO_3$ using critical temperatures at different concentrations.

4.3.3.3. $Li_2Mn_{1-x}Cr_xO_3$

The dependence of the miscibility gap of $Li_2Mn_{1-x}Cr_xO_3$ is illustrated in Figure 4.19. The gap decreases as the temperature is increased. At the maxima of the curve, 1700 K, the two phases mix.

Table 4.7: Concentration of Manganese chromium with respect to critical temperatures for a mixed system $Li_2Mn_{1-x}Cr_xO_3$

Concentration (Cr)	Critical Temperature (K)
0.1	950
0.2	1000
0.3	1100
0.4	1400
0.5	1700
0.6	1500
0.7	1400
0.8	1200
0.9	1100

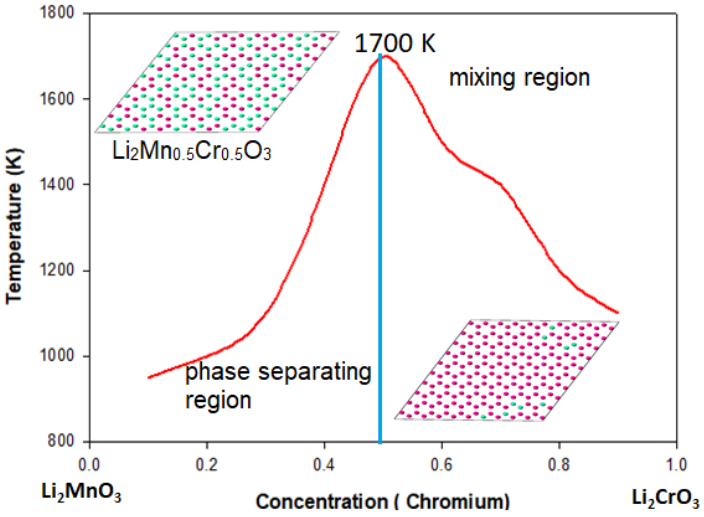

Figure 4.19: Constructed phase diagram of $Li_2Mn_{1-x}CrxO_3$ using critical temperature at different concentrations.

4.3.3.4. $Li_2Mn_{1-x}Ru_xO_3$

Figure 4.20 depicts a constructed phase diagram of Ru-doped Li_2MnO_3. The diagram shows that when the system is cooled the miscibility gap decreases and mixing occurs at 1300 K.

Table 4.8: Concentration of Manganese ruthenium with respect to critical temperatures for a mixed system $Li_2Mn_{1-x}RuxO_3$

Concentration (Ru)	Critical Temperature (K)
0.1	1650
0.2	1600
0.3	1500
0.4	1400
0.5	1300
0.6	1400
0.7	1450
0.8	1500
0.9	1550

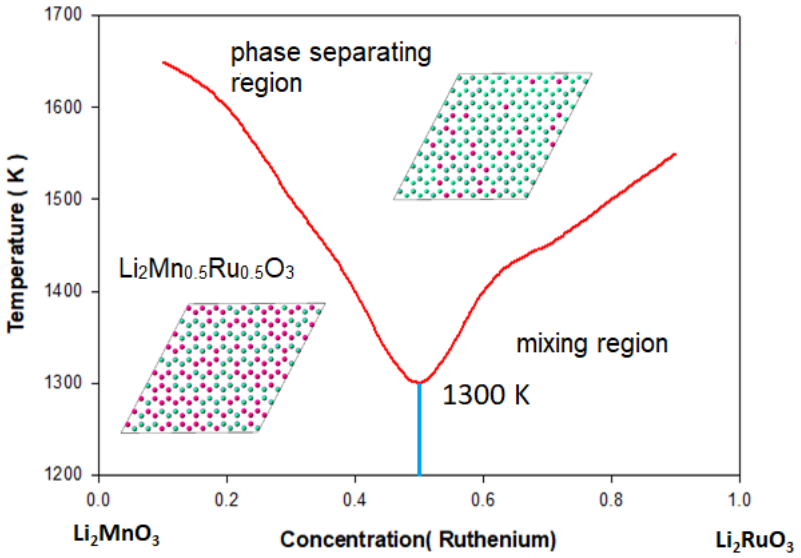

Figure 4.20: Constructed phase diagram of $Li_2Mn_{1-x}Ru_xO_3$ using critical temperature at different concentrations.

4.4. Discussion

Cluster expansion method was employed for $Li_2Mn_{1-x}Ni_xO_3$, $Li_2Mn_{1-x}Co_xO_3$, $Li_2Mn_{1-x}Cr_xO_3$ and $Li_2Mn_{1-x}Ru_xO_3$ to generate 73, 65, 90 and 83 new stable phases, respectively. The binary phase diagram predicted $Li_2Mn_{0.83}Ni_{0.17}O_3$, $Li_2Mn_{0.5}Co_{0.5}O_3$, $Li_2Mn_{0.5}Cr_{0.5}O_3$ and $Li_2Mn_{0.5}Ru_{0.5}O_3$ as the most stable phases of doped Li_2MnO_3. Monte Carlo simulations technique was utilized to investigate the thermodynamic properties of $Li_2Mn_{1-x}Ni_xO_3$, $Li_2Mn_{1-x}Co_xO_3$, $Li_2Mn_{1-x}Cr_xO_3$ and $Li_2Mn_{1-x}Ru_xO_3$ for the entire range of transition metal concentrations. Various phase diagrams were constructed from Monte Carlo simulations critical temperatures to show how $Li_2Mn_{1-x}Ni_xO_3$, $Li_2Mn_{1-x}Co_xO_3$, $Li_2Mn_{1-x}Cr_xO_3$ and $Li_2Mn_{1-x}Ru_xO_3$ systems change phases when the temperature was introduced. The $Li_2Mn_{1-x}Ni_xO_3$, $Li_2Mn_{1-x}Co_xO_3$, $Li_2Mn_{1-x}Cr_xO_3$ and $Li_2Mn_{1-x}Ru_xO_3$ systems were found to mix well at 850 K, 700 K, 1700 K and 1300 K respectively. Phase equilibrium of $Li_2Mn_{1-x}Ni_xO_3$, $Li_2Mn_{1-x}Co_xO_3$, $Li_2Mn_{1-x}Cr_xO_3$ and $Li_2Mn_{1-x}Ru_xO_3$ systems require that the free energy of all the constituent phases is known as a function of composition and temperature. The techniques have been successfully employed by Nguyen *et al.* [107] on binary (NiFe)(AlFe) 0, Chinnappan *et al*. [108] on the V–Ta alloy and Diale *et al.* [109] on Ti-Pd-Ru alloys, where the solid solution phase has a bcc structure. The results prove the advantage and the suitability of a combined

cluster expansion and Monte Carlo approach for studying phase transformations and thermodynamic properties occurring in $Li_2Mn_{1-x}Ni_xO_3$, $Li_2Mn_{1-x}Co_xO_3$, $Li_2Mn_{1-x}Cr_xO_3$ and $Li_2Mn_{1-x}Ru_xO_3$ systems.

Chapter 5 : Conclusions and Recommendations

5.1. Conclusions

First principle DFT+U calculations were employed to investigate the structural, thermodynamic, electronic, elastic and vibrational properties of the layered Li_2MnO_3 at 0 K to mimic their stability. The determination of the equilibrium cell parameters was achieved by subjecting the structure to full geometry optimization. The calculated lattice parameters correlated well with the reported experimental data from the literature to within 5% validating the approach employed. The thermodynamic stability of Li_2MnO_3 was investigated by calculating the heat of formations. The value was predicted to be low and negative, -874.417 KJ/mol, suggesting that the Li_2MnO_3 structure is thermodynamically stable.

The investigation of electronic properties was done by calculating the density of states (DOS). Li_2MnO_3 showed semiconductor behaviour characteristics with a band gap of 1.89 eV. The partial densities of states showed that the states around the Fermi level are predominantly from the p-orbital of lithium. The calculated elastic constants suggested mechanical stability for the Li_2MnO_3 structure since it satisfied the necessary Borne stability criterion for monoclinic crystals. The macroscopic Bulk and Young's moduli were found to be high and positive, indicating hardness and stiffness. Furthermore, the Pugh's ratio (B/G) for ductility and brittleness revealed that Li_2MnO_3 is brittle because it was less than 1.75. The phonon dispersion curves for Li_2MnO_3 structures revealed a lack of soft mode availability along the high symmetry zone, indicating vibrational stability.

Furthermore, the cluster expansion method was employed for $Li_2Mn_{1-x}Ni_xO_3$, $Li_2Mn_{1-x}Co_xO_3$, $Li_2Mn_{1-x}Cr_xO_3$ and $Li_2Mn_{1-x}Ru_xO_3$ to generate 73, 65, 90 and 83 new stable phases, respectively, from binary phase diagrams at 0 K. The new phases generated depict a miscible constituent whereby structures with energies close to the ground states have the lowest heat of formations at a given concentration. $Li_2Mn_{0.83}Ni_{0.17}O_3$, $Li_2Mn_{0.5}Co_{0.5}O_3$, $Li_2Mn_{0.5}Cr_{0.5}O_3$ and $Li_2Mn_{0.5}Ru_{0.5}O_3$ were found to be the most stable phases. Lastly, the Monte Carlo simulations technique was utilized to investigate thermodynamic properties and phase transitions of $Li_2Mn_{1-x}Ni_xO_3$, $Li_2Mn_{1-x}Co_xO_3$, $Li_2Mn_{1-x}Cr_xO_3$ and $Li_2Mn_{1-x}Ru_xO_3$ for the entire range of transition metal concentrations. Various phase diagrams were constructed from Monte Carlo simulations results to illustrate how $Li_2Mn_{1-x}Ni_xO_3$, $Li_2Mn_{1-x}Co_xO_3$, $Li_2Mn_{1-x}Cr_xO_3$ and Li_2Mn_{1-}

$_xRu_xO_3$ systems change phases when the temperature is introduced. Phase diagrams constructed using MC simulations results show that $Li_2Mn_{1-x}Ni_xO_3$, $Li_2Mn_{1-x}Co_xO_3$, $Li_2Mn_{1-x}Cr_xO_3$ and $Li_2Mn_{1-x}Ru_xO_3$ properly mix at 850 K, 700 K, 1700 K and 1300 K respectively.

The results prove the usefulness of a combined cluster expansion and Monte Carlo approach for studying phase transformations and thermodynamical properties occurring in $Li_2Mn_{1-x}TM_xO_3$ systems. Such validation will provide valuable insights which will guide experiments on where phase separation and mixed phases tend to occur in $Li_2Mn_{1-x}Ni_xO_3$, $Li_2Mn_{1-x}Co_xO_3$, $Li_2Mn_{1-x}Cr_xO_3$ and $Li_2Mn_{1-x}Ru_xO_3$.

5.2. Recommendations and future work

In light of the findings of this dissertation, three recommendations for future research are listed below:

- Use first principle calculations to study the key properties such as structural stability, electronic structure and mechanical stability of the newly generated phases of Li_2MnO_3.
- Use molecular dynamics to compare the results obtained using Monte Carlo simulation.
- Use MeDeA-UNCLE to generate co-doped phases of Li_2MnO_3.

Bibliography

[1] O. Schmidt, A. Hawkes, A. Gambhir and I. Stafell, “The future cost of electrical energy storage based on experience rates.,” *Nature Energy,* vol. 2, p. 1, 2017.

[2] A. Manthiram, “An outlook on lithium ion battery technology.,” *Central Science,* vol. 3, p. 1063, 2017.

[3] M. S. Guney and Y. Tepe, “Classification and assessmemt of energy storage sytems.,” *Renewable and Sustainable Energy Reviews,* vol. 75, p. 1187, 2017.

[4] A. R. Dehghani-Sanija, E. Tharumalingam, M. B. Dusseault and R. Fraser, “Study of energy storage systems and environmental challenges of batteries.,” *Renewable and Sustainable Energy Reviews,* vol. 104, p. 192, 2019.

[5] D. Larcher and J. M. Tarascon, “Towards Greener and More Sustainable Batteries for Electrical Energy Storage.,” *Nature Chemistry,* vol. 7, p. 19, 2015.

[6] H. Tian, P. Qin, K. Li and Z. Zhao, “A review of the state of health for lithium-ion batteries: Research status and suggestions,” *Journal of Cleaner Production,* vol. 261, p. 120813, 2020.

[7] G. E. Blomgren, “The Development and Future of Lithium Ion Batteries.,” *Journal of Electrochemical Society,* vol. 164, p. A5019, 2017.

[8] G. Liu, S. Dai, Q. Han and K. Liu, “Enhanced Electrochemical Properties of $LiMn_2O_4$ Cathode Materials by Coating with ZnO,” *International Journal of Electrochemical science,* vol. 17, p. 2, 2022.

[9] Z. Qu, S. Liu, P. Zhang, R. Wang, H. Wang, B. He, Y. Gong, J. Jin and S. Li, “Enhanced eletrochemical performances of $LiCoO_2$ at high cut-off voltage by introducing LiF additive,” *Solid State Ionics,* vol. 365, p. 115654, 2021.

[10] M. Sathiya, K. Ramesha, G. Rousse, D. Foix, D. Gonbeau, A. S. Prakash, M. L. Doublet, K. Hemalatha and J. M. Tarascon, “High perfomance $Li_2Ru_{1-y}Mn_yO_3$ ($0.2<y<0.8$) cathode materials for rechargeable lithium-ion batteries: Their understanding.,” *Chemistry Materials,* vol. 25, p. 1121, 2013.

[11] F. Li, X. Zhang, J. Lin, J. Ma, S. Zhang and G. Yang, “Unveiling the role of oxygen vacancy in Li_2MnO_3 upon delithiation.,” *Journal of Physical Chemistry C,* vol. 123, p. 23403, 2019.

[12] W. Zhao, L. Xiong , Y. Xu , X. Xiao and J. Wang, “Magnesium substitution to improve the electrochemical performance of layered Li_2MnO_3 positive-electrode material.,” *Journal of Power Sources,* vol. 330, p. 37, 2016.

[13] P. Kalyani, C. Chitra, T. Mohan and G. Gopukumar, “Lithium metal rechargeable cells using Li_2MnO_3 as positive electrode.,” *Journal of Power Sources,* vol. 80, p. 103, 1999.

[14] K. Shimoda, M. Oishi, T. Matsunaga, M. Murakami, K. Yamanaka, H. Arai, Y. Ukyo, Y. Uchimoto, T. Ohta, E. Matsubara and Z. Ogumi, “Direct observation of layered-to-spinel phase transformation in Li_2MnO_3 and the spinel structure stabilised after the activation process.,” *Journal of Materials Chemistry A,* vol. 5, p. 6695, 2017.

[15] A. R. Armstrong, M. Holzapfel, P. Novák, C. S. Johnson, S.H. Kang, M. M. Thackeray and P. G. Bruce, “Demonstrating oxygen loss and associated structural reorganization in the lithium battery cathode $Li[Ni_{0.2}Li_{0.2}Mn_{0.6}]O_2$.,” *Journal of American Chemical Society,* vol. 128, p. 8694, 2006.

[16] Z. Q. Wang, M. S. Wu, B. Xu and C. Y. Ouyang, “Improving the electrical conductivity and structural stability of the Li_2MnO_3 cathode via P doping.,” *Journal of Alloys and Compounds,* vol. 658, p. 818, 2016.

[17] H. Zhang, Y. Gong, J. Li, K. Du, Y. Cao and J. Li, “Selecting substituent elements for LiMnPO4 Cathode materials combined with density functional theory (DFT) calculations and experiments.,” *Journal of Alloys and Compounds,* vol. 793, p. 360, 2019.

[18] D. Mori, H. Sakaebe, M. Shikano, H. Kojitane, K. Tatsumi and Y. Inaguma, “Synthesis, phase relation and electrical and electrochemical properties of ruthenium-substituted Li_2MnO_3 as a novel cathode material.,” *Journal of Power Sources,* vol. 196, p. 6934, 2011.

[19] G. B. Liu, H. Liu, Y. Wang, Y. F. Shi and Y. Zhang, “The electrochemical properties of Fe- and Ni-cosubstituted Li_2MnO_3 via combustion method.,” *Journal of Solid State Electrochemistry,* vol. 17, p. 2434, 2013.

[20] P. H. Xia, Z. Q. Deng, A. Manthiram and G. Henkelman, “Calculations of oxygen stability in lithium-rich layered cathodes.,” *Journal of Physical Chemistry C,* vol. 116, p. 23201, 2012.

[21] S. Kim, J. K. Noh, S. Yu, W. Chang, K. Y. Chung and B. W. Cho, “Effects of transition metal doping and surface treatment to improve the electrochemical performance of Li_2MnO_3.,” *Journal of Electroceramics,* vol. 30, p. 159, 2013.

[22] Y. R. Gao, J. Ma, X. F. Wang, X. Lu, Y. Bai, Z. X. Wang and L. Q. Chen, “Improved electron/Li-ion transport and oxygen stability of Mo-doped Li_2MnO_3.,” *Journal of Materials Chemistry A,* vol. 2, p. 4811, 2014.

[23] Y. Gao, X. Wang, J. Ma, Z. Wang and L. Chen, “Selecting substituent elements for Li-Rich Mn-based cathode materials by density functional theory (DFT) calculations.,” *Chemistry of Materials,* vol. 27, p. 3456, 2015.

[24] D. Lindel and T. B. Reddy, Handbook Of Batteries, New York: McGraw-Hill, 2002.

[25] M. Hu, X. Pang and Z. Zhou, “Recent progress in high-voltage lithium ion batteries.,” *Journal of Power Sources,* vol. 237, p. 229, 2012.

[26] V. Aravindan, “TiO_2 Polymorphs in 'rocking-chair' Li-ion batteries.,” *Materials Today,* vol. 18, p. 345, 2015.

[27] N. Kitta, “Li-ion Battery Materials: Present and Future.,” *Materials Today,* vol. 18, p. 252, 2015.

[28] P. Strobel and B. Lambert-Andron, “Crystollagraphic and magnetic structure of Li_2MnO_3.,” *Journal of Solid State Chemistry,* vol. 75, p. 90, 1988.

[29] D. Y. W. Yu, K. Yanagida, Y. Kato and H. Nakamura, “Electrochemical activities in Li_2MnO_3.,” *Journal of Electrochemical Society,* vol. 156, p. A417, 2009.

[30] Y. Okamoto, “Ambivalent effect of oxygen vacancies on Li_2MnO_3: A first principle study.,” *Journal of Electrochemical Society,* vol. 159, p. A152, 2012.

[31] T. Teufl, B. Strehle, P. Müller, H. A. Gasteiger and M. A. Mendez, “Oxygen release and surface degradation of Li- and Mn-rich layered oxides in variation of Li_2MnO_3 content.,” *Journal of The Electrochemical Society,* vol. 165, p. A2718, 2018.

[32] Y. Lei, J. Nie, Z. Hu, Z. Wang, F. Gui, B. Li, P. Ming, C. Zhang, Y. Elias, D. Aurbach and Q. Xiao, “Surface Modification of Li-Rich Mn-Based Layered Oxide Cathodes: Challenges, Materials, Methods, and Characterization.,” *Advanced Energy Materials,* vol. 10, p. 2002506, 2020.

[33] T. Chen, C. Foo and S.C.E. Tsang, “Interstitial and substitutional light elements in transition metals for heterogenious catalysis.,” *Chemical Science,* vol. 12, p. 517, 2021.

[34] F. Kong, R. C. Longo, M.S. Park, J. Yoon, D.H. Yeon, J. H. Park, W. H. Wang, S. G. Doo and K. Cho, “First principles study on Li-site doping effect on the properties of Li_2MnO_2 and Li_2MnO_3 cathode materials.,” *ECS Transactions,* vol. 64, p. 21, 2015.

[35] A. Lanjan, B. G. Choobar and S. Amjad-Iranagh, “First principle study on the application of crystalline cathodes $Li_2Mn_{0.5}TM_{0.5}O_3$ for promoting the perfomance of lithium ion batteries.,” *Computational Materials Science,* vol. 173, p. 109417, 2020.

[36] F. Kong, R. C. Longo, M. S. Park, J. Yoon, D.H. Yeon, J. H. Park, W. H. Wang, S. G. Doo and K. Cho, “Ab initio study of doping effects on Li_2MnO_2 and Li_2MnO_3 cathode materials for Li-ion batteries.,” *Journal of Materials Chemistry A,* vol. 3, p. 8489, 2015.

[37] J. Lee, Y. Gong, L. Gu and B. Kang, “Long-term cycle stability enabled by the incorporation of Ni into Li_2MnO_3 phase in the Mn-based Li-rich layered materials.,” *ACS Energy Letters,* vol. 6, p. 789, 2021.

[38] Q. Li, Z. Yao, E. Lee, Y. Xu, M.M. Thackeray, C. Wolverton, V. P. Dravid and J. Wu, “Dynamic imaging of crystalline defects in lithium-manganese oxide electrodes during electrochemical activation to high voltage.,” *Nature Communications,* vol. 10, p. 1, 2019.

[39] B. Singh and P. Singh, “Ru doping effect on the structural, electronic, transport, optical and dye degradation properties of layered Li_2MnO_3.,” *Applied Sciences,* vol. 2, p. 1, 2020.

[40] T. Matsunaga, H. Komatsu, K. Shimoda, T. Minato, M. Yonemura, T. Kamiyama, S. Kobayashi, T. Kato, T. Hirayama, Y. Ikuhara, Y. and H. Arai, “Structural understanding of superior battery properties of partially Ni-doped Li_2MnO_3 as cathode material.,” *The Journal of Physical Chemistry Letters,* vol. 11, p. 2063, 2016.

[41] E. Wimmer, R. Najafabadi, G. A. Young, J. D. Ballard, T.M. Angeliu, J. Vollmer, J. J. Chambers, H. Niimi, J. B. Shaw, C. Freeman and M. Christensen, “Ab initio calculations for industrial materials engineering: successes and challenges,” *Journal of Physics: Condensed Matter,* vol. 38, p. 384215, 2010.

[42] S. Müller, “Bulk and Surface Ordering Phenomena in Binary Metal Alloys.,” *Journal of Physics: Condensed Matter,* vol. 34, p. R1429, 2003.

[43] G. Ceder, A. Van der Ven, C. Marianetti and D. Morgan, “First-iprinciples alloy theory in oxides.,” *Modelling and Simulation in Material Science and Engineering,* vol. 8, p. 322, 2000.

[44] Z. Yang, R. E. Ward, N. Tanibata, H. Takeda, M. Nakayama and T. Asaka, "Arrangement in $La_{1/3}NbO_3$ obtained by first principles density functional theory with cluster expansion and Monte Carlo simulation.," *Journal of Physical Chemistry C,* vol. 124, p. 9746, 2020.

[45] K. Wang, D. Cheng, C. Lu and B. Zhou, "First-principles investigation of the phase stability and early stages of precipitation in Mg-Sn alloys.," *Physical Review Materials,* vol. 4, p. 013606, 2020.

[46] P. Hohenberg and W. Kohn, "Inhomogeneous electron Gas," *Physical Review,* vol. 136, p. 864, 1964.

[47] L. H. Thomas, "The Calculation of Atomic Fields.," *Mathematical Proceedings of the Cambridge Philosophical Society,* vol. 23, p. 542, 1927.

[48] D. R. Hartree and V. A. Fock, "The wave mechanics of an atom with a non-coulomb central Field. Part I. Theory and methods.," *Mathematical Proceedings of the Cambridge Philosophical Society,* vol. 24, p. 89, 1928.

[49] J. C. Slater, "A Generalized Self-Consistent Field Method," *Physical Review,* vol. 81, p. 385, 1951.

[50] T. J. Zielinski, E. Harvey, R. Sweeney and D. M. Hanson, "Quantum states of atoms and molecules.," *Journal of Chemical Education,* vol. 82, p. 1880, 2005.

[51] P. W. Ayers, S. Golden and M. Levy, "Generalizations of the Hohenberg-Kohn Theorem: I. Legendre transform constructions of variational principles for density matrices and electron distrbution functions," *Journal of Chemical Physics,* vol. 124, p. 054101, 2006.

[52] W. Kohn and L. Sham, "Self-consistent equations including exchange and correlation Effects.," *Physical Review Journals Archive,* vol. 140, p. 1133, 1965.

[53] M. Chakraverty, H.M. Kittur and P.A. Kumar, “First Principle Simulations of Various Magnetic Tunnel Junctions for Applications in Magnetoresitive Random Access Memories,” *IEEE Transactions on Nanotechnology,* vol. 12, p. 971, 2013.

[54] B. J. Alder and D. M. Ceperley, “Ground State of the Electron Gas by a Stochastic Method.,” *Physical Review Letters,* vol. 45, p. 566, 1980.

[55] K. Horn and M. Scheffler, Handbook of surface science: electronic structure., vol. 2, North Holland, 2000.

[56] P. J Perdew, “Density-Functional Approximation for the Correlation Energy of the Inhomogeneous Electron Gas,” *Physical Review B,* vol. 34, p. 7406, 1986.

[57] A. D. Becke, “Density-Functional Exchange-Energy Approximation with Correct Asymptotic Behavior,” *Physical Review,* vol. 38, p. 3098, 1988.

[58] Y. Wang and J. P. Perdew, “Accurate and Simple Analytic Representation of the Electron-Gas Correlation Energy,” *Physical Review,* vol. 45, p. 13244, 1992.

[59] J. P. Perdew, K. Burke and M. Ernzerhof, “Generalized Gradient Approximation Made Simple.,” *Physical Review Letters,* vol. 77, p. 3865, 1996.

[60] E. Wimmer and J. Andzelm, “Density Functional Gaussian-type-Orbital Approach to Molecular Geometries, Vibrations and Reaction Energies.,” *The Journal of Chemical Physics,* vol. 96, p. 1280, 1992.

[61] M. Meyer and V. Pontikis, “Application of Computer Simulation in Material Science,” *Applied Mechanics and Materials,* vol. 112, p. 257, 1991.

[62] M. L. Cohen and M. T. Yin, “Theory of lattice-dynamical properties of solids: Application to Si and Ge.,” *Physical Review B,* vol. 26, p. 3259, 1982.

[63] M. Massimi, Pauli's exclusion principle: The origin and validation of a scientific principle., vol. 5, Cambridge University Press, 2005, p. 437.

[64] D. R. Hamann, M. Schlüter and C. Chiang, “Norm conserving pseudopotentials.,” *Physical Review Letters,* vol. 43, p. 1494, 1979.

[65] M. Suzuki and I. S. Suzuki, “Lecture note on solid state physics: mean-field theory,” *System,* vol. 6000, p. 1, 2006.

[66] D. J. Chadi and M. L. Cohen, “Special points in the Brillouin Zone,” *Physical Review B,* vol. 8, p. 5747, 1973.

[67] H. J. Monkhorst and J. D. Pack, “Special points for Brillouin-zone integrations.,” *Physical Review B,* vol. 13, p. 5188, 1976.

[68] G. Kresse, J. Furthmüller and J. Hafner, “Theory of the crystal structures of selenium and tellurium: The effect of generalized-gradient corrections to the local-density approximation,” *Phys. Rev. B,* vol. 50, p. 13181, 1994.

[69] G. Kresse, J. Furthmüller and J. Hafner, “Theory of the crystal structures of selenium and tellurium: The effect of generalized-gradient corrections to the local-density approximation.,” *Physical Review B,* vol. 50, p. 13181, 1994.

[70] P. E. Blöchl, “Projector augmented-wave method.,” *Physical Review B,* vol. 50, p. 17953, 1994.

[71] K. Parlinski, “Molecular dynamics simulation of incommensurate phases.,” *Computer Physics Reports,* vol. 8, p. 153, 1988.

[72] M. Zbiri, R. Mittal, S. Rols, Y. Su, Y. Xiao, H. Schober, S.L.Chaplot, M.R. Johnson, T. Chatterji, Y. Inoue, S. Matsuishi, H. Hosono and T.Brueckel, “Magnetic lattice dynamics of the oxygen-free FeAs: how sensitive are phonons to magnetic ordering,” *Journal of Physics: Condensed Matter,* vol. 22, p. 315701, 2010.

[73] J. M. Sanchez, F. Ducastelle and D. Gratias, “Generalized cluster description of multicomponent systems.,” *Physica A: Statistical Mechanics and its Applications,* vol. 128, p. 334, 1984.

[74] A. Mark, D. de Fontaine, M. van Schilfgaarde, M. Sluiter and M. Methfessel, “First-principles phase-stability study of fcc alloys in the Ti-Al system.,” *Physical Review B,* vol. 46, p. 5055, 1992.

[75] C. Colinet, A. Pasturel, D. Nguyen Manh, D. G. Pettifor, and P. Miodownik, “Phase stability study of the Al-Nb system.,” *Physical Review B,* vol. 56, p. 552, 1997.

[76] M. Asta, R. McCormack and D. de Fontaine, “Theoretical study of alloy phase stability in the Cd-Mg system.,” *Physical Review B,* vol. 48, p. 748, 1993.

[77] D. Lerch, O. Wiekhorst, G. L. W. Hart, R. W. Forcade, and S. Müller, “UNCLE: a code for constructing cluster expansions for arbitrary lattices with minimal user-input.,” *Modelling and Simulation in Material Science and Engineering,* vol. 17, p. 055003, 2009.

[78] G. L. W. Hart, V. Blum, M. J. Walorski and A. Zunger, “Evolutionary approach for determining first-principles hamiltonians.,” *Nature Materials,* vol. 4, p. 391, 2005.

[79] D. Reith, M. Stöhr, R. Podloucky, T. C. Kerscher and S. Müller, “First-principles modeling of temperature- and concentration-dependent solubility in the phase-separating alloy Fe_xCu_{1-x}.,” *Physical Review B,* vol. 86, p. 020201, 2012.

[80] Z. Zhou and B. Joós, “Stability criteria for homogeneously stressed materials and the calculation of elastic constants.,” *Physical Review B,* vol. 54, p. 3841, 1996.

[81] O. Beckstein, J.E. Klepeis, G. L. W. Hart and O. Pankratov, “First-principles elastic constants and electronic structure of α-Pt_2Si and PtSi.,” *Physical Review B,* vol. 63, p. 134112, 2001.

[82] M. Born and K. Huang, “Dynamical theory of crystal lattices.,” *Acta Crystallographica,* vol. 9, p. 837, 1956.

[83] R. Hill, Mechanics of solids, Pergamon, 1982.

[84] J. Wang, J. Li., S. Yip, S. Phillpot and D. Wolf, “Mechanical instabilities of homogeneous crystals.,” *Physical Review B,* vol. 52, p. 12627, 1995.

[85] T. H. K. Barron and M. L. Klein, “Second-order elastic constants of a solid under stress.,” *Proceedings of the Physical Society (1958-1967),* vol. 85, p. 523, 1965.

[86] A. St-Amant, W. D. Cornell , P. A. Kollman and T. A. Halgren, “A study of geometries, conformational energies, dipole moments and electrostatic potential fitted charges using density functional theory.,” *Journal of Computational Chemistry,* vol. 16, p. 1483, 1995.

[87] X. Q. Chen, H. Y. Niu, D. Z. Li and Y. Y. Li, “Modelling hardness of polycrystalline materials and bulk metallic glasses.,” *Intermetallics,* vol. 19, p. 1275, 2011.

[88] Z. Wu, X. J. Chen, V. V. Struzhkin and R. E. Cohen, “Trends in elasticity and electronic structure of transition metal nitrides and carbides from first principles.,” *Physical Review B,* vol. 71, p. 214103, 2005.

[89] C. Kittel and P. McEuen, Introduction to solid state physics., New York: Wiley, 1996.

[90] M. L. Cohen, “Calculation of bulk Moduli of diamond and zinc-blende solids.,” *Physical Review B,* vol. 32, p. 7988, 1985.

[91] S. F. Pugh, “Relationship between the elastic moduli and the plastic properties of a polycrystalline pure metals.,” *The London, Edinburgh, and Dublin Philosophical Magazine and Journal of Science,* vol. 45, p. 823, 1954.

[92] Y. L. Page and P. Saxe, “Ab-initio vs literature stiffness values for Ga: a caveat about crystal settings.,” *Physica B,* vol. 191, p. 57, 2001.

[93] G. Bao, D. Duan, D. Zhou, X. Jin, B. Liu and T. Cui, “Structural, electronic, and optical properties of crystalline iodoform under high pressure: A first-principles study.,” *Journal of Physical Chemistry B,* vol. 114, p. 3999, 2010.

[94] R. B. Kaner, J. J. Gilman and S. H. Tolbert, “Designing superhard materials.,” *Science,* vol. 308, p. 1268, 2005.

[95] R. Hill, “The elastic behavior of a crystalline aggregate.,” *Proceedings of the Physical Society,* vol. 65, p. 349, 1952.

[96] S. .J. Blundell and K. M. Blundell, Concepts in thermal physics, New York: Oxford University Press on Demand, 2010.

[97] Y. N. Gornostyrev, O. Y. Kontsevoi, A. F. Maksyutov, A. J. Freeman, M. I. Katsnelson, A. V. Trefilo and A. I. Lichtenstein, “Negative yield stress temperature anomaly and structural instability of Pt_3Al.,” *Physical Review B,* vol. 70, p. 014102, 2004.

[98] D. A. Pankhurst, D. Nguyen-Manh and D.G. Pettifor, “Electronic origin of structural trends across early transition-metal disilicides: Anomalous behaviour of $CrSi_2$.,” *Physical Review B,* vol. 69, p. 075113, 2004.

[99] D. Zhang, J. Wang, K. Dong and A. Hao, “First principle investigation on the elastic and electronic properties of Mn, Co, Nb, Mo doped $LiFePO_4$.,” *Computational Materials Science,* vol. 155, p. 410, 2018.

[100] F. Mouhart and F. X. Couder, “Necessary and sufficient elastic stability conditions in various crystal systems.,” *Physical Review B,* vol. 90, p. 224104, 2014.

[101] S. F. Pugh, “Relationship between the elastic moduli and the plastic properties of a polycrystalline pure metals.,” *The London, Edinburgh, and Dublin Philosophical Magazine and Journal of Science,* vol. 45, p. 823, 1954.

[102] C. James, Y. Wu, B. Sheldon and Y. Qi, “Computational Analysis of Coupled Anisotropic Chemical Expansion in $Li_{2-X}MnO_{3-\delta}$,” *Materials Research Society Advances,* vol. 1, p. 11037, 2016.

[103] A. Jain, S. P. Ong, G. Hautier, W. Chen, W. D. Richards, S. Dacek, S. Cholia, D. Gunter, D. Skinner, G. Ceder and K. A. Persson, “Commentary: The Materials Project:

A materials genome approach to accelerating materials innovation," *APL Materials,* vol. 1, p. 011002, 2013.

[104] R. J. Bosco and B. G. Jeyaprakash, "Lattice vibrations, phonons, specific heat capacity, thermal conductivity.," *School of Electrical & Electronics Engineering,* vol. 5, p. 20, 2007.

[105] S. Kazanc and S. Ozgen, "An investigation of temperature effect on phonon dispersion spectra of Ni by molecular dynamics simulation.," *Turkish Journal of Physics,* vol. 32, p. 315, 2008.

[106] D. Ye, C. Sun, Y. Chen, K. Ozawa, D. Hulicova, J. Zou and L. Wang, "Ni-induced stepwise capacity increase in Ni-poor Li-rich cathode materials for high performance lithium ion batteries.," *Nano Research,* vol. 8, p. 808, 2015.

[107] M. C. Nguyen, X. Zhao, C. Wang and K. Ho, "Cluster expansion modeling and Monte Carlo simulation of alnico 5–7 permanent magnets.," *Journal of Applied Physics,* vol. 117, p. 093905, 2015.

[108] R. Chinnappan, "Phase stability of V–Ta alloy using cluster expansion and Monte Carlo techniques.," *Calphad,* vol. 39, p. 33, 2012.

[109] R. G. Diale, R. Modiba, P. E. Ngoepe and H. R. Chauke, "Phase stability of $TiPd_{1-x}Ru_x$ and $Ti_{1-x}PdRu_x$ shape memory alloys.," *Materials Today Proceedings,* vol. 38, p. 1071, 2020.

Appendix A

Papers presented at conferences

1. South African Institute of Physics (SAIP) conference(Virtual) (2021) "**Computational modelling study on the stability of Li_2MnO_3 cathode material for lithium-ion batteries**".
2. Post-graduate research day held at Fusion Boutique Hotel (Polokwane) (2021) "**Computational modelling study of phase stability of Li_2MnO_3 cathode material for lithium-ion batteries**".
3. CHPC National Conference (2021) **"A search for stable structures of doped Li_2MnO_3 using cluster expansion and Monte Carlo simulations".**
4. South African Institute of Physics (SAIP) conference(Virtual) (2022) "**Phase stability of $Li_2Mn_{1-x}TM_xO_3$ (TM= Ni, Co, Cr and Ru) cathode material using cluster expansion and Monte Carlo simulations".**